# The Study of Ruthenium Polypyridyl Complexes for Dye Sensitized Solar Cell Applications

A DISSERTATION
SUBMITTED TO THE FACULTY OF
UNIVERSITY OF MINNESOTA
BY

Ryan Joseph Hue

IN PARTIAL FULFILLMENT OF THE REQUIREMENTS
FOR THE DEGREE OF
DOCTOR OF PHILOSOPHY

Wayne L. Gladfelter

June, 2013

**Acknowledgements**

Wayne Gladfelter
The Gladfelter Resarch Group
Rajan Vatassery
Andrew Bierbaum

David Blank
The Blank Research Group
Jon Hinke
Antonio Sanchez-Diaz

Kent Mann
The Mann Research Group
Raghu Chitta
Kyle Schwartz
Lindsay Hinkle

Stephen Campbell
Brijesh Kumar

Uwe Kortshagen
Ryan Gresback

**Abstract**

Nanocrystals are of great scientific interest as their properties form a bridge between bulk material properties and those of atomic or molecular structures. Researchers have been taking advantage of the unique properties of nanocrystals since the early 1990's to produce new device architectures for solar energy conversion and light-emitting diodes (LED).

In order to limit our dependence on fossil fuels and provide an energy solution for the future, renewable energy research is currently a major area of focus. One such device is a dye-sensitized solar cell (DSSC) that makes use of ruthenium polypyridyl dyes. Ruthenium polypyridyl complexes and their direct applications to dye-sensitized solar cells will be studied. Chapter 2 examines the synthesis, separation, and characterization of linkage isomers of the well-studied diisothiocyanato ruthenium dye N3. Chapter 3 examines the synthesis of amino substituted ruthenium bipyridine complexes and how the HOMO and LUMO energy levels affect charge injection into the metal oxide. Chapter 4 uses ultrafast transient absorption (TA) spectroscopy in collaboration with the Blank research group to study the charge injection of a diethylamino-substituted ruthenium dye into a ZnO nanocrystal.

A second device that will be studied is the light-emitting diode. Chapter 5 will focus on the synthesis and characterization of air-stable, monodisperse, highly photoluminescent indium phosphide (InP) nanocrystals, which emit from visible to infrared wavelengths. A wide range of particle sizes can be produced with narrow size distributions by changing the growth time or reaction concentrations. In addition, a successive ion layer adsorption and reaction (SILAR) technique is used to deposit a shell to stabilize the core against oxidation and increase the photoluminescence. The stability and emission are assessed using UV-Vis and fluorescence spectroscopy.

# Table of Contents

## List of Tables

## List of Figures

# 1 Introduction to Nanocrystal Based Devices

Nanocrystals are of great scientific interest as their properties form a bridge between bulk material properties and those of atomic or molecular structures. Typical nanocrystals are approximately spherical and have a diameter from 1 to 100 nm. While a bulk material has constant physical properties regardless of its dimensions, at the nano-scale this is often not the case. The first report of nanocrystals was in the 1850's by Faraday when he observed the surface plasmon resonance of gold nanocrystals in solution.[1] Ekimov, *et al.* first discovered these properties in semiconductor nanocrystals in the early 1980's, when they saw a size dependent shift in the HOMO-LUMO energy gap.[2] Researchers have been taking advantage of the unique properties of nanocrystals since the early 1990's to produce new device architectures for solar energy conversion and light-emitting diodes (LED).[3, 4]

## 1.1 Dye-Sensitized Solar Cells

In order to limit our dependence on fossil fuels and provide an energy solution for the future, renewable energy research is currently a major area of focus. There are several forms of renewable energy that are actively being explored, one of which being solar power. The sun provides an abundant and near limitless energy source that makes harvesting solar energy an appealing option over other sources. A majority of the solar cells currently in use are solid-state photovoltaic cells that make use of abundant materials like silicon. These types of cells are expensive to process due to the high-purity silicon needed to make an efficient solar cell.[3] Therefore solar cells that make use of

inexpensive, low-purity, easily processable materials, such as nanocrystalline metal oxides are becoming more prevalent. One such device that makes use of these metal oxides is a dye-sensitized solar cell (DSSC). The use of nanocrystalline metal oxides was a large development, since it was previously thought that rough surfaces would lead to recombination loss in the cells. However, Grätzel and O'Regan recognized that the dye molecules act as barriers between the electron produced in the semiconductor lattice and the positive charge carriers, preventing charge recombination.[5]

A schematic representation of a DSSC is presented in Figure 1.1.[5] The cell consists of two transparent conducting oxide electrodes that can be deposited on a number of substrates such as glass or flexible polymers. The use of flexible and transparent substrates helps promote the long term durability of the devices and the ability to integrate the devices into existing building structures. On one of the electrodes, a porous, nanocrystalline, wide band gap metal oxide film is deposited, such as titanium dioxide ($TiO_2$), zinc oxide (ZnO), or tin oxide ($SnO_2$). The metal oxide of choice is $TiO_2$ due to its low cost, non-toxicity, and wide availability. Attached to the surface of the nanocrystalline film is a monolayer of the sensitizer or dye. The dye-metal oxide layer is then placed in contact with a redox electrolyte.

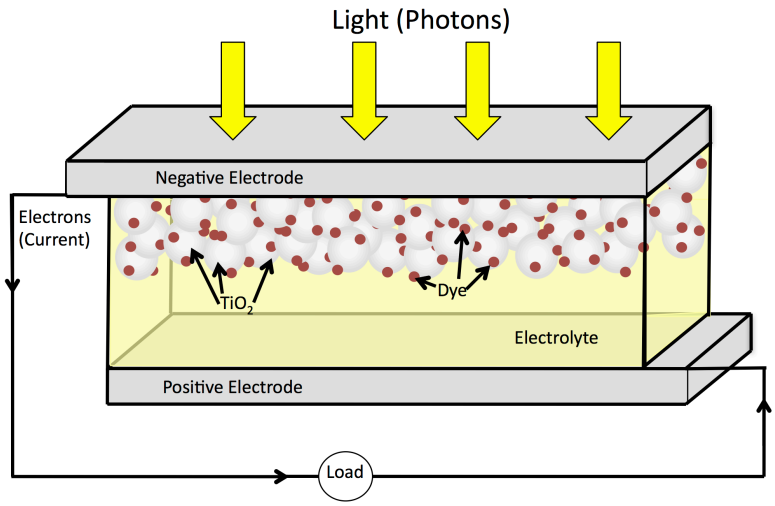


**Figure 1.1: Nanocrystal based dye-sensitized solar cell.**

The DSSC works by having light pass through the metal oxide film, where the dye absorbs the light not absorbed by the metal oxide. The photoexcited dye then injects an electron into the conduction band of the metal oxide. The injection process takes place as long as the excited state energy of the dye is higher in energy than the conduction band of the semiconductor. The cationic dye is then reduced by the electrolyte, which usually contains the iodide/triiodide redox couple. By having the electrolyte reduce the dye, the conduction band electron is allowed to escape through the external circuit. The iodide is then regenerated by the reduction of triiodide at the counter electrode. The device generates electric power from light without suffering any permanent chemical transformations. With this device architecture, DSSCs allow the light absorption process to be separated from the charge carrier transport process. This is advantageous for diffuse light adsorption, something that solid state solar cells cannot do effectively.[3, 5]

The nanocrystalline metal oxides are important to the DSSC architecture because of their high surface area to volume ratio. The absorption of light by a monolayer of dye is weak because the area occupied by one molecule is much larger than its optical cross section for light absorption. Therefore, an efficient dye-sensitized solar cell cannot be manufactured from a metal oxide with a flat surface, but instead a porous, nanocrystalline film with a large surface area. Depending on the thickness, constructing a film of 20 nm sized nanocrystals, results in a surface area of over 1000 times greater than a flat surface.[3] This allows more dyes to adsorb to the surface of the metal oxide and thus more light to be absorbed.

The first DSSC was produced in the laboratory of Michael Grätzel using a ruthenium polypyridyl dye adsorbed to a $TiO_2$ nanocrystalline film and obtained a light-to-electricity conversion efficiency of approximately 8%.[5] Since then, countless new dyes, particularly ruthenium complexes have been synthesized to study light absorption and charge transfer.[6-26] To date, N3 and its double deprotonated form N719 are the champion ruthenium complexes for overall device efficiency (12%),[10, 12] making them the standards for comparison.

Ruthenium is the metal of choice for dye complexes for multiple reasons. Ruthenium offers a wide range of oxidation states (from $2^-$ to $8^+$), which are accessible chemically, and electrochemically. The kinetic stability of these oxidation states and the reversible nature of its redox couples make ruthenium attractive for use in the DSSC system, where it will constantly be under going redox reactions. Another important aspect of ruthenium complexes is their sensitivity to synthetic substitution to induce changes in

both redox and spectral properties. The metal-to-ligand charge transfer (MLCT) often has intense absorption bands that extend into the visible and infrared region of the spectrum. The position of the MLCT absorption can be modified by altering the substituents on the bipyridine rings and by controlling the $d(\pi) - \pi^*$ back-bonding of the nonchromophore ligands.[27] The molar extinction coefficient of the MLCT absorption is often very intense, regularly around 15,000 $M^{-1}$ $cm^{-1}$, which is necessary to absorb a large portion of light. These complexes also have long lived triplet excited states, often in the microsecond regime. For comparison, electron transfer from the photoexcited complex is often complete in picoseconds and sometimes femtoseconds.[27] This ensures that photoluminescence of the excited complex does not compete with charge injection, ultimately leading to a greater charge transfer efficiency into the metal oxide film. Finally, these complexes are quite robust/photostable and are generally insensitive to their external environment. Therefore, intense light, adsorption to the metal oxide, and contact with the electrolyte do not have an affect on the properties of the ruthenium complexes.

For these reasons, ruthenium polypyridyl complexes and their direct applications to dye-sensitized solar cells will be studied. Chapter 2 examines the synthesis, separation, and characterization of linkage isomers of the well-studied diisothiocyanato ruthenium dye N3. Chapter 3 examines the synthesis of amino substituted ruthenium bipyridine complexes and how the HOMO and LUMO energy levels affect charge injection into the metal oxide. Chapter 4 uses ultrafast transient absorption (TA) spectroscopy in

collaboration with the Blank research group to study the charge injection of a diethylamino-substituted ruthenium dye into a ZnO nanocrystal.

## 1.2 Light-Emitting Diodes

A light-emitting diode is a semiconductor diode that produces monochromatic light. The electroluminescence produced is a function of the band gap of the material used. In this way, colored light is produced without the need for colored filaments. LEDs have advantages over conventional incandescent lighting due to greater efficiency and longer lifetime. Light emitting diodes do not have a filament to burn out, thus they last longer. Also, LEDs do not produce heat like conventional incandescent light bulbs, which wastes energy and decreases efficiency. A typical LED consists of a doped semiconducting material, which produces a p-n junction, where the P-type and N-type semiconductors meet. Electrons and holes flow from the electrodes to the p-n junction, where they recombine radiatively to produce light.

Semiconductor nanocrystals are important to LEDs because their physical properties are size dependent, which produces different properties than the bulk material. These properties emerge when a crystalline particle is smaller than the exciton Bohr radius of the bulk material. When a nanocrystal is smaller than the excitonic Bohr radius, quantum confinement effects dictate the energy of electrons and holes.[4] Because the electrons are confined in more than one dimension, the nanocrystal's electronic states become quantized. Seen in Figure 1.2, a nanocrystal's electronic structure is somewhere in between the continuous bands of the bulk and the single molecular orbitals of a molecule. This can be seen optically as a size dependent band gap peak, usually in the

ultraviolet/visible region, depending on the material.[28] Therefore, by changing the size of the nanocrystal, the band gap can be tuned to give a desired emission wavelength.[29]

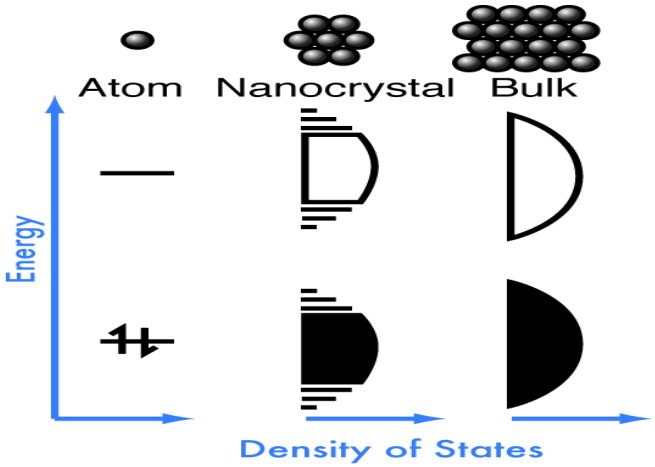


**Figure 1.2: Density of electronic states in an atom, a nanocrystal, and a bulk semiconductor.**

Established technologies, such as inorganic LEDs and lasers have been optimized in the infrared region for communications, spectroscopy, and chemical sensing. These devices offer high performance and lifetimes; however they are expensive, especially for larger devices. Therefore, new device models that make use of cheaper materials and fabrication techniques are needed to enable expanded use of infrared optoelectronics. Organic electronics are currently cheap and easily fabricated; however, they are unable to extend into the infrared. Current research involves integration of semiconductor nanocrystals into organic electron and hole transport layers to produce efficient LEDs for a variety of applications. This will combine the ease of organic processing with the ability to tune emissions into the IR.

A schematic representation of a nanocrystal based LED device is presented in Figure 1.3. LED devices can be constructed with conducting polymers using

monodisperse nanocrystals exhibiting a maximum photoluminescence and charge mobility. The process begins by taking an ITO coated glass slide, which is the anode, and depositing a hole-transporting layer (HTL) by either atomic layer deposition or spin coating. The nanocrystals are then deposited by spin coating on top of the HTL. As the solvent used to spin coat the nanocrystals dries, self-segregation of the HTL/NC occurs, forming an interface. A second interface is then created, by deposition of an electron-transporting layer (ETL) in a similar manner as the HTL. The HTL and ETL are organic or polymeric materials of sufficient energy gap to confine the charge carriers and prevent recombination in adjacent layers. In order to prevent exciton recombination outside of the nanocrystal, the HTL and ETL should not come in contact with each other. Finally, a transition metal cathode is deposited on top of the ETL by thermal evaporation. When the device in Figure 1.3 is exposed to forward bias, holes from the ITO are injected into the HOMO of the hole transporting layer and electrons from the cathode are injected into the LUMO of an electron-transporting layer.[30]

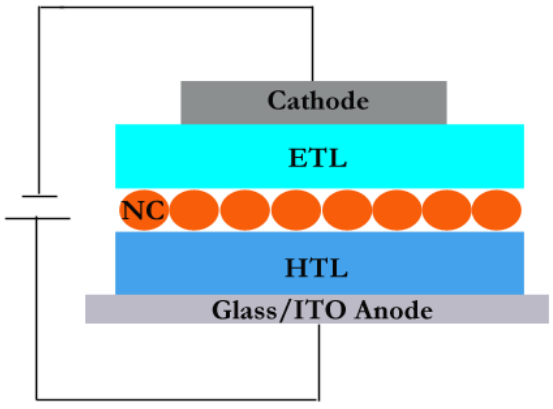


**Figure 1.3: Nanocrystal based LED device architecture using conducting polymers as transport layers.[31]**

The carriers are then able to travel toward the nanocrystal interface to form excitons that recombine radiatively in the nanocrystal to yield electroluminescence. The wavelength of electroluminescence is the energy of the band gap of the nanocrystal. The efficiency of charge transfer and photoluminescence determines the electroluminescence and overall device efficiency.[32] Therefore, all interfaces are important and tuning the transport and emissive layers can maximize device efficiency.[31]

Chapter 5 will focus on the synthesis and characterization of air-stable, monodisperse, highly photoluminescent indium phosphide (InP) nanocrystals, which emit from visible to infrared wavelengths. A wide range of particle sizes can be produced with narrow size distributions by changing the growth time or reaction concentrations. In addition, a successive ion layer adsorption and reaction (SILAR) technique is used to deposit a shell to stabilize the core against oxidation and increase the photoluminescence. The stability and emission are assessed using UV-Vis and fluorescence spectroscopy.

# 2 Linkage Isomerism in Ruthenium and Iridium Thiocyanate Complexes

We report the synthesis and spectroscopic characterization of ruthenium $Ru(iBuBpy)_2(NCS)_2$ and iridium $Ir(iBuPP)_2(NCS)_2$ thiocyanate complexes. By adjusting the reaction conditions in the ruthenium system, thiocyanate linkage isomers were isolated in pure form, producing a doubly N-bound complex **1** and the mixed N- and S-bound thiocyanate complex **2**. These complexes were characterized by NMR, mass spectrometry, and visible spectroscopy to prove the existence of the linkage isomers. The kinetic isomerization reaction of **2** to **1** was also studied. In the iridium system, linkage isomers were not observed, as all reactants went to the doubly N-bound product. The iridium complex was characterized and compared to the ruthenium complexes.

## 2.1 Introduction

During the past two decades, dye-sensitized solar cells (DSSC) utilizing titanium dioxide and ruthenium complexes have emerged as promising options for solar energy conversion due to low costs and increasing efficiencies.[3, 5] The diisothiocyanato ruthenium complexes known as N3 and N719 (Figure 2.1) have shown the largest conversion efficiencies to date (11.2%), making them the standard for comparison for all new ruthenium sensitizers.[12] Thiocyanate is an ambidentate ligand that can bind to the metal center through the nitrogen (isothiocyanate) or the sulfur (thiocyanate). In the synthesis of the doubly N bound diisothiocyanato complex N3 (abbreviated NN) there is also the possibility of producing the NS and SS linkage isomers. In isolating pure NN by HPLC, suspected NS is removed, which is observed as a small peak in the chromatogram with a similar retention time to the NN complex.[10, 33] While the SS isomer has not been reported, the NS isomer is believed to be present in small amounts (less than 4%), though it has not been isolated in pure form due to low yields.

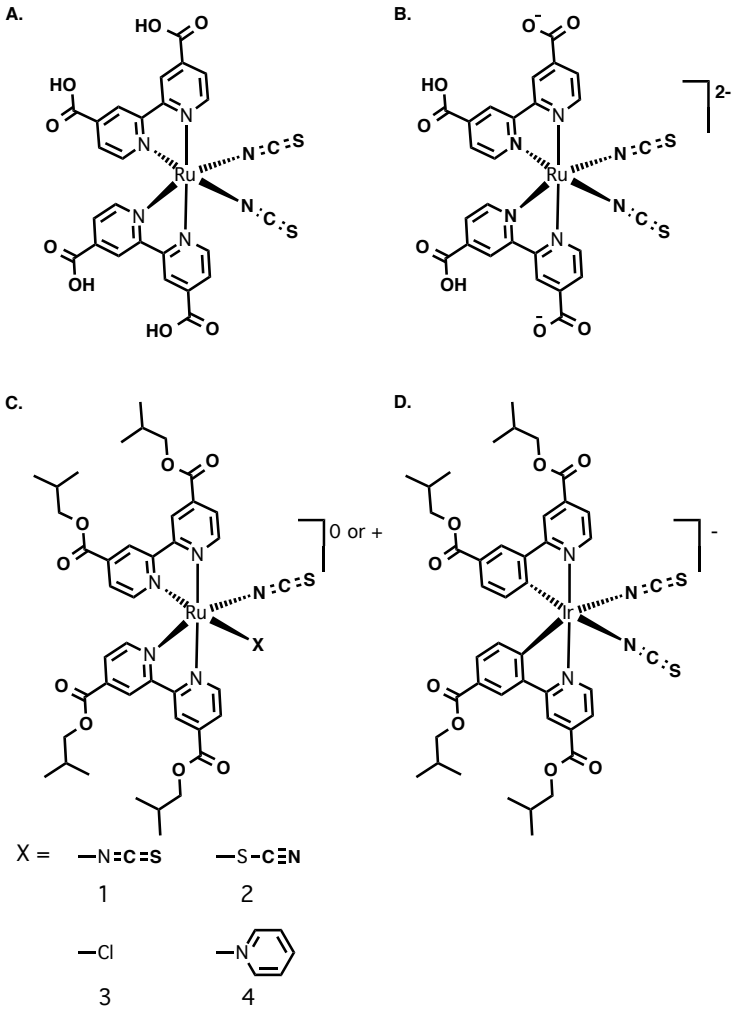


**Figure 2.1: Structure of metal complexes A.) N3, B.) N719, C.) Ruthenium linkage isomers, and D.) Iridium thiocyanate complex.**

It has been proposed that S-bound thiocyanate ligands are less efficient than the N bound isomer, due to thermal stability of the N-bound complexes.[34] Grätzel constructed a device with a mixture of linkage isomers in a mono-thiocyanate ruthenium complex and found a 10-20% decrease in the incident photon-to-current conversion efficiency (IPCE) values when compared to the purely N-bound complex.[9] It has been suggested computationally that when the thyocyanate is N-bound, the sulfur interacts with the

iodide electrolyte, which promotes regeneration of the oxidized dye.[35] This leads to an overall increase in the efficiency of the device.

The study of inorganic linkage isomerism dates back to the early 1900's,[36, 37] with the first thiocyanate linkage isomers reported in 1963 by John Burmeister.[38] Since the first report, Burmeister has studied how the additional ligands (steric and electronic effects),[38-41] solvents,[42, 43] and synthetic conditions[44, 45] have an impact on the binding mode of the thiocyanate group. In dithiocyanato complexes, steric and electronic factors of the other ligands tend to dictate the bonding mode of the thiocyanate ligand, often leading to either doubly N or S bonded products.[36, 39] However, by using bidentate ligands (such as bipyridine), mixed bonding of the thiocyanate ligand has also been observed in square planar Pd (II) complexes by changing the substituents and the position of the substituents on the bipyridine rings.[46, 47]

More recently, thiocyanate linkage isomerism has been observed in several ruthenium complexes to date. Grätzel has distinguished thiocyanate linkage isomers by NMR and IR of two anionic ruthenium benzimidazol complexes, $[Ru(bmipy)(dcbpy)SCN]^-$ and $[Ru(ph\text{-}bmipy)SCN]^-$, however neither isomer was isolated in pure form.[9] Freedman and coworkers were able to synthesize and isolate both linkage isomers of [(*para*-cymeme)Ru(bpy)SCN]$^+$ and characterize each by crystallography.[48] The most recent example of thiocyanate linkage isomerism was reported by Crabtree, in which both linkage isomers of $[Ru(terpy)(tbbpy)SCN]^+$ were isolated and characterized by NMR, IR and crystallography.[49] While ruthenium linkage isomerism has been well studied in mono-thiocyanate ruthenium complexes, a mixed isomer complex that exhibits

both an N-bound and S-bound thiocyanate has yet to be isolated in pure form.

We have adapted a known procedure from Rawling and coworkers that makes use of isobutyl ester groups at the 4 and 4' bipyridine positions to synthesize and isolate the doubly N bound, the N- and S-bound, and a mono-substituted NCS ester-analogue to N3.[50] The isobutyl esters make purification on a silica gel column straightforward. By modifying the synthesis conditions, particularly the choice of solvent and thiocyanate salt, it is possible to control the amount of each isomer formed. In addition to isolating the NS isomer, we have prepared an iridium analogue to the ester substituted ruthenium complexes. The iridium complex **5** is characterized and compared to the ruthenium complexes.

## 2.2 Experimental

### 2.2.1 Materials

Ruthenium (III) chloride trihydrate ($RuCl_3 \cdot 3H_2O$) and iridium (III) chloride hydrate ($IrCl_3 \cdot H_2O$) were purchased from Pressure Chemical Company and used as received. Spectroscopic grade methanol, 2,2'-bipyridine, 4,4'-dimethyl-2,2'-bipyridine, isobutanol, ammonium thiocyanate, silver thiocyanate, and tetrakis(triphenylphosphine)palladium were purchased from Sigma Aldrich and used as received. 2-Bromo-4-methylpyridine and 3-(methoxycarbonyl)phenylboronic acid were purchased from TCI America and used as received. All additional solvents were dried (unless water was used as a co-solvent) and deoxygenated before use, and all procedures were performed using standard Schlenk techniques. 4,4'-Dicarboxylic acid-bipyridine (**L1**) and bis(2-methylpropyl)-2,2′-bipyridine-4,4′-dicarboxylate (**L2**) were synthesized according to literature methods.[50, 51]

### 2.2.2 Methods

NMR spectra were taken on a Varian Inova 300 or 500 MHz spectrometer and chemical shifts were referenced to the residual solvent peak. Mass spectral data were taken on a Bruker BioTOF II operating in the ESI-TOF mode. Electronic absorption spectra were collected on an Ocean Optics DH-2000-BAL spectrometer. The steady-state emission spectra were recorded on a Spex Fluorolog 1680 0.22 m double spectrometer equipped with a xenon source. Fluorescence spectra were corrected over the entire wavelength region to compensate for changes in the instrument's sensitivity at longer wavelengths. UV-visible and fluorescence spectroscopic measurements were performed in quartz cuvettes with a 3 mm path length unless otherwise noted. The ATR IR spectra of ruthenium complexes were recorded on a Nicolet MAGNA-IR 560 spectrometer. Cyclic voltammograms were obtained on a BAS-100B electrochemical analyzer using methods previously described.[52] All solutions were prepared in acetonitrile or dimethylformamide with 0.1 M tetra-n-butylammonium hexafluorophosphate, $[N(C_4H_9)_4][PF_6]$, as the supporting electrolyte and degassed with argon. Potentials were referenced to a Ag/AgCl electrode and are reported versus NHE.

### 2.2.3 Synthesis of 2-bromo-4-carboxylic acid-pyridine (L3)

This procedure is based on the synthesis of 4,4'-dicarboxylic acid-2,2'-bipyridine.[51] To a stirred solution of 2-bromo-4-methylpyridine (2.5 g, 0.015 mol) and 60 mL concentrated sulfuric acid, potassium dichromate (8.6 g, 0.030 mol) was added in small portions. Upon addition of potassium dichromate, the reaction temperature rose to 80°C. Once the temperature fell below 40°C (approximately 2 hours), the reaction mixture was

poured onto 400 g of an ice and water mixture, and the precipitated solid was filtered and washed with water. **L3** was dried under vacuum to yield 2.53 g (85%) of as a white solid. $^1$H-NMR (300 MHz; DMSO-$d_6$): δ 14.03 (s, 1H), 8.57 (d, *J* = 5.0 Hz, 1H), 7.95 (t, *J* = 0.7 Hz, 1H), 7.83 (ddd, *J* = 5.0, 1.4, 0.4 Hz, 1H).

### 2.2.4 Synthesis of 2-bromo-4-methylcarboxylate-pyridine (L4)

**L3** (1.7 g, 0.0084 mol), sulfuric acid (1.6 mL, 0.021 mol), and methanol (60 mL, 0.88 mol) were refluxed until the reaction mixture turned clear (3.5 hours) and excess methanol was evaporated. The brown oil was taken up in water and made basic with saturated sodium carbonate. **L4** was extracted from the water layer with chloroform (3 x 100 mL) and evaporated to give 1.64 g (95%) of the desired compound as a light brown oil. $^1$H-NMR (300 MHz; CDCl3): δ 8.55 (dd, *J* = 5.1, 0.7 Hz, 1H), 7.89 (dd, *J* = 1.3, 0.7 Hz, 1H), 7.78 (dd, *J* = 5.1, 1.4 Hz, 1H), 3.98 (s, 3H).

### 2.2.5 Synthesis of 3,4'-dimethoxycarbonyl-phenylpyridine (L5)

**L4** (2.14 g, 0.01 mol) was dissolved in toluene (30 mL). Lithium chloride (1.26 g, 0.030 mol) and tetrakis(triphenylphosphine)palladium (0.23 g, 0.000198 mol, 2 mol %) were added and the reaction was cooled to 0°C. An aqueous solution of sodium carbonate (12.4 mL, 2.0 M) was added to the reaction, which was allowed to stir for 10 minutes. A solution of 3-(methoxycarbonyl)phenylboronic acid 3.58 g (3.58 g, 0.0198 mol) in ethanol (15.0 mL) was added dropwise to the reaction at 0°C and allowed to stir for 3 minutes. The reaction was warmed to room temperature, stirred for 30 minutes, and refluxed for 17.5 hours. The reaction was cooled to room temperature, and the aqueous phase was separated from the organic layer. The aqueous layer was further extracted with toluene (2 x 100 mL), and washed with 1 M sodium hydroxide solution. The organic

phase was dried over sodium sulfate and evaporated to give 1.72 g (64%) of the **L5** as a yellow oil. $^1$H-NMR (300 MHz; $CDCl_3$): δ 8.87 (dd, *J* = 5.0, 0.9 Hz, 1H), 8.72 (t, *J* = 1.5 Hz, 1H), 8.37 (dd, *J* = 1.4, 0.9 Hz, 1H), 8.31 (ddd, *J* = 7.8, 1.9, 1.2 Hz, 1H), 8.14 (dt, *J* = 7.8, 1.4 Hz, 1H), 7.84 (dd, *J* = 5.0, 1.5 Hz, 1H), 7.61 (td, *J* = 7.8, 0.5 Hz, 1H), 4.48 (q, *J* = 7.1 Hz, 3H), 3.99 (s, 3H).

### 2.2.6 Synthesis of bis(2-methylpropyl)-phenylpyridine-3,4′-dicarboxylate (L6)

**L5** (1.34 g, 0.0050 mol), concentrated sulfuric acid (0.80 mL, 0.014841 mol), and isobutanol (150 mL) were refluxed for 4 hours and the excess isobutanol was evaporated. The brown oil was taken up in water, basified with saturated sodium carbonate, and extracted with methylene chloride (3 x 100 mL). **L6** was purified on a silica gel column with methylene chloride:ethyl acetate (90:10) as the eluant to give 1.66 g (94%) of the desired ligand as a yellow oil. $^1$H-NMR (300 MHz; $CDCl_3$): δ 8.87 (dd, *J* = 5.0, 0.7 Hz, 1H), 8.70 (d, *J* = 1.7 Hz, 1H), 8.35 (d, *J* = 0.8 Hz, 1H), 8.29 (dt, *J* = 7.8, 1.5 Hz, 1H), 8.14 (dt, *J* = 7.8, 1.4 Hz, 1H), 7.83 (dd, *J* = 5.0, 1.4 Hz, 1H), 7.59 (t, *J* = 7.8 Hz, 1H), 4.47 (q, *J* = 7.1 Hz, 1H), 4.18 (dd, *J* = 8.4, 6.7 Hz, 3H), 2.14 (dq, *J* = 13.4, 6.7, 1.7 Hz, 2H), 1.05 (dd, *J* = 6.7, 0.9 Hz, 12H).

### 2.2.7 Synthesis of $[Ru((ibu)_2bpy)_2Cl_2]Cl_2$ (R1)

$RuCl_3$-$3H_2O$ (1.0 g, 4 mmol) was added under nitrogen to a solution of lithium chloride (0.920 g, 0.0217 mol) in ethylene glycol:water (20 mL, 4:1) at 110°C. After 15 minutes, **L2** (2.96 g, 0.0083 mol) was added under nitrogen. After an additional 15 minutes glucose (0.15 g, 8 mmol) was added and then after an additional 15 minutes ascorbic acid (0.373 g, 2 mol) was added and the reaction was maintained at 110°C for 30 minutes. The reaction was quenched with the addition of 10 mL of a saturated NaCl

solution and cooled to 0°C for 60 min. The reaction mixture was then filtered, washed with brine, and then toluene:ether:acetone (70:20:5). **R1** was isolated on a neutral alumina column with methylene chloride:ethyl acetate (50:50) as eluant to yield 3.5 g (82% yield) of a green solid. $^1$H-NMR (300 MHz; $CD_2Cl_2$): δ 10.34 (dd, *J* = 6.0, 0.5 Hz, 2H), 8.89 (d, *J* = 1.2 Hz, 2H), 8.72 (d, *J* = 1.3 Hz, 2H), 8.21 (dd, *J* = 5.9, 1.7 Hz, 2H), 7.75 (dd, *J* = 6.0, 0.5 Hz, 2H), 7.53 (dd, *J* = 6.0, 1.8 Hz, 2H), 4.29 (d, *J* = 6.6 Hz, 4H), 4.14 (d, *J* = 6.6 Hz, 4H), 2.29-2.15 (m, 2H), 2.13-2.02 (m, 2H), 1.11 (d, *J* = 6.7 Hz, 12H), 1.00 (d, *J* = 6.7 Hz, 2H).

### 2.2.8 Synthesis of Ru(ibubpy)$_2$(NCS)(X) (1-3)

**R1** (0.20 g, 0.23 mmol), either ammonium thiocyanate or silver thiocyanate (9.2 mmol), and 50 mL of either tetrahydrofuran or ethanol were refluxed under nitrogen for between 3-32 hours. Reaction times for tetrahydrofuran were 32 hours and for ethanol were 3-6 hours. Table 1 lists specific times for solvent and counterion combinations. The reaction was stopped at the disappearance of **R1** as monitored by TLC, and excess solvent was evaporated. Complexes **1** (NN), and **2** (NS), and **3** (NCl) were separated on a silica gel column using methylene chloride:ethyl acetate (95:5) as eluant. The order of elution was excess thiocyanate salt, then **1-NN**, followed by **2-NS**, and finally **3-NCl**. All ruthenium complexes were dark purple bands on the column and were isolated as dark purple solids. Table 1 lists the yields for the individual reactions.

**1** (NN):$^1$H-NMR (500 MHz; $CD_2Cl_2$): δ 9.71 (dd, *J* = 5.8, 0.6 Hz, 2H, 6), 8.91 (d, *J* = 1.1 Hz, 2H, 3), 8.75 (d, *J* = 1.1 Hz, 2H, 3'), 8.30 (dd, *J* = 5.8, 1.7 Hz, 2H, 5), 7.65-7.60 (m, 4H, 5' and 6'), 4.31 (d, *J* = 6.6 Hz, 4H), 4.16 (d, *J* = 6.6 Hz, 4H), 2.27-2.16 (m, 2H),

2.13-2.02 (m, 2H), 1.12 (d, $J$ = 6.7 Hz, 12H), 0.99 (d, $J$ = 6.7 Hz, 12H). HR-ESIMS m/z expected [M + $Na^+$] = 953.1916, m/z observed [M + $Na^+$] = 953.1921.

**2** (NS): $^1$H-NMR (500 MHz; $CD_2Cl_2$): δ 10.08 (dd, $J$ = 5.9, 0.6 Hz, 1H, $6_1$), 9.60 (dd, $J$ = 5.9, 0.6 Hz, 1H, $6_2$), 8.90 (dd, $J$ = 9.3, 1.2 Hz, 2H, 3), 8.76 (dd, $J$ = 6.0, 1.3 Hz, 2H, 3'), 8.26 (dd, $J$ = 5.9, 1.7 Hz, 2H, 5), 7.69-7.63 (m, 4H, 5' and 6'), 4.30 (dd, $J$ = 6.6, 2.5 Hz, 4H), 4.15 (dd, $J$ = 11.7, 6.7 Hz, 4H), 2.30-2.15 (m, 2H), 2.15-2.01 (m, 2H), 1.12 (d, $J$ = 6.7 Hz, 12H), 1.00 (dd, $J$ = 6.7, 2.9 Hz, 12H). HR-ESIMS m/z expected [M + $Na^+$] = 953.1916, m/z observed [M + $Na^+$] = 953.1921.

**3** (NCl): $^1$H-NMR (500 MHz; $CD_2Cl_2$): δ 10.29 (dd, $J$ = 5.9, 0.6 Hz, 1H, $6_1$), 9.73 (dd, $J$ = 5.9, 0.6 Hz, 1H, $6_2$), 8.88 (dd, $J$ = 4.5, 1.1 Hz, 2H, 3), 8.72 (dd, $J$ = 3.5, 1.3 Hz, 2H, 3'), 8.24 (ddd, $J$ = 11.2, 5.9, 1.7 Hz, 2H, 5), 7.74 (dd, $J$ = 6.0, 0.6 Hz, 1H, $6_1$'), 7.64 (dd, $J$ = 6.0, 0.6 Hz, 1H, $6_2$'), 7.55 (ddd, $J$ = 6.0, 3.2, 1.8 Hz, 2H, 5'), 4.30 (dd, $J$ = 6.6, 2.6 Hz, 4H), 4.15 (dd, $J$ = 6.6, 3.1 Hz, 4H), 2.29-2.16 (m, 2H), 2.15-2.01 (m, 2H), 1.11 (dd, $J$ = 6.7, 1.1 Hz, 12H), 0.99 (dd, $J$ = 6.7, 3.5 Hz, 12H). HR-ESIMS m/z expected [M + $Na^+$] = 930.1853, m/z observed [M + $Na^+$] = 930.1855.

**Table 2.1: Reaction conditions and yields for the ruthenium complexes**

| Solvent | Precursor | Reaction Time | Isolated NN | Isolated NS | Isolated NCl |
|---|---|---|---|---|---|
| THF | $NH_4NCS$ | 32 h | 0.076 g 30% | 0.012 g 4% | 0.086 g 32 % |
| THF | AgNCS | 32 h | 0.151 g 72% | - | - |
| EtOH | $NH_4NCS$ | 3 h | 0.156 g 73% | 0.033 g 15% | - |
| EtOH | AgNCS | 6 h | 0.160 g 77% | 0.007 g 3% | - |

### 2.2.9 Synthesis of Ru(ibubpy)$_2$(NCS)(Pyridine) (4)

A solution of **3** (0.060 g, 0.065 mmol) and silver trifluoromethanesulfonate (AgOTf, 0.051 g, 0.20 mmol) in acetonitrile (15 mL) was heated at 60 °C for 12 hours giving the mono-solvento species (confirmed through ESI MS). Pyridine (1.0 mL, 0.012 mol) was injected and the reaction refluxed for an additional 12 hours. The reaction was cooled to room temperature, excess solvent was evaporated, and **4** was purified on a silica gel column with methylene chloride:acetonitrile (90:10) as eluant to yield 0.060 g (80%) of a dark red solid. $^1$H-NMR (300 MHz; $CD_2Cl_2$): $\delta$ 9.70 (d, $J$ = 5.9 Hz, 1H), 9.01 (d, $J$ = 1.4 Hz, 1H), 8.87 (dd, $J$ = 5.6, 1.4 Hz, 2H), 8.79 (d, $J$ = 1.5 Hz, 1H), 8.59 (d, $J$ = 5.9 Hz, 1H), 8.33 (dd, $J$ = 5.8, 1.7 Hz, 2H), 8.21 (dd, $J$ = 5.9, 1.7 Hz, 2H), 8.05 (d, $J$ = 5.9 Hz, 1H), 7.90 (dd, $J$ = 5.9, 1.7 Hz, 1H), 7.83 (tt, $J$ = 7.6, 1.4 Hz, 1H), 7.73 (dd, $J$ = 5.9, 1.7 Hz, 1H), 7.66 (d, $J$ = 5.9 Hz, 1H), 7.39 (t, $J$ = 6.9 Hz, 2H), 4.29 (dd, $J$ = 6.6, 3.9 Hz, 4H), 4.18 (dd, $J$ = 6.7, 4.7 Hz, 4H), 2.15 (ddtd, $J$ = 29.9, 13.4, 6.7, 3.2 Hz, 4H), 1.09 (dd, $J$ = 6.7, 1.3 Hz, 12H), 1.00 (dd, $J$ = 6.7, 4.2 Hz, 12H).

### 2.2.10 Kinetic Isomerization of 2-NS

Complex **2** (0.0005 g, 5.4 x $10^{-7}$ mol) was dissolved in 500 $\mu$L of dimethylsulfoxide- $D_6$ and placed in a Varian Inova 300 MHz spectrometer preheated to 80 °C. The sample was allowed to equilibrate for 5 minutes, at which point an initial spectrum was acquired. From that point, a spectrum consisting of 32 scans was taken every 5 minutes for 900 minutes. Upon completion, the sample was cooled to room temperature, allowed to equilibrate for an hour, and a final spectrum was acquired.

### 2.2.11 Preparation of linkage isomers of N3

Complex **1** or **2** (0.015 g, 0.016 mmol) was dissolved in acetonitrile (15 mL) and 0.16 mL of a 1M tetra-n-butylammonium hydroxide (0.16 mmol) solution was added. The resulting solution was stirred at room temperature for 40 minutes and protected from light. The solvent was removed at room temperature and the resulting residue was dissolved in 5 mL of water, and the pH adjusted to 3.5 using 0.1 M nitric acid, at which point the mixture became cloudy. The suspension was stored in the freezer overnight and the resulting precipitate was filtered and washed with pH 3.5 water.

### 2.2.12 Synthesis of [Ir($^{i}$BuBAinic)$_2$Cl)]$_2$ (I1)

A solution of **L6** (0.50g, 1.4 mmol) in isobutanol ($^{i}$BuOH, 10 mL) was added to a flask containing isobutanol (5 mL) and $IrCl_3 \cdot 3H_2O$ (0.23g, 0.64 mmol) that had been pulverized with a mortar and pestle. The reaction mixture was allowed to reflux under nitrogen for 24 h. After cooling to room temperature the reaction mixture was concentrated by rotary evaporation to give a red oily residue. Sonication of the oil in the presence of MeOH induced precipitation of a sticky orange solid. The MeOH was decanted and a powder was obtained by repeated sonication / filtration cycles in hexanes followed by collection a fritted glass funnel. The solid was dried *in vacuo* giving compound **I1** as a dull yellow solid. Yield: 68%. $^1$H NMR (300 MHz, $CD_2Cl_2$): δ 9.28 (d, 4H, *J* = 6.3 Hz), 8.15 (s, 4H), 7.70 (d, 4H, *J* = 7.5 Hz), 7.59 (d, 4H, *J* = 3.9 Hz), 7.25 (d, 4H, *J* = 3.9 Hz), 7.14 (d, 4H, *J* = 3.6 Hz), 7.02 (dd, 4H, *J* = 6.3, 1.8 Hz), 6.94 (s, 8H), 6.89 (t, 4H, *J* = 7.5 Hz), 6.73 (d, 4H, *J* = 3.6 Hz) 6.68 (t, 4H, *J* = 7.5 Hz), 6.12 (d, 4H, *J* = 7.8 Hz), 2.71 (q, 16H, *J* = 7.2 Hz), 2.32 (s, 12H), 2.16 (s, 24H), 1.46 (m, 32H), 0.989 (t, 12H, *J* = 6.6 Hz), 0.910 (t, 12H, *J* = 7.2 Hz).

### 2.2.13 Synthesis of $[N(C_4H_9)_4][Ir(^tBuBAinic)_2(NCS)]$ (5)

$[Ir(^tBuBAinic)_2Cl]_2$ (0.13 g, 0.068 mmol) **I1** was dissolved in acetonitrile (25 mL) to give a yellow-orange solution. Once fully dissolved the dimer **I1** treated with an acetonitrile solution (5 mL) of AgOTf (0.039 g, 0.15 mmol). The resulting reaction mixture was protected from light and allowed to stir at room temperature for 7 h. The reaction mixture was filtered through a Celite pad removing a dull gray precipitate (AgCl). The filter cake was washed with additional acetonitrile (40 mL) to provide a clear yellow solution of the bis-solvento complex $[Ir(^tBuBAinic)_2(NCCH_3)_2]OTf$ (**I2**). The solution of **I2** was concentrated to ~10 mL by rotary evaporation and the solution degassed with argon. Treatment of **I2** with tetrabutylammonium thiocyante($N(C_4H_9)_4$)NCS, 0.21 g, 0.68 mmol) resulted in an immediate color change from yellow to orange. The reaction mixture was again protected from light and stirred under an inert gas atmosphere for 24 h then concentrated under reduced pressure to give an oily red-orange residue. The oil was dissolved in $CH_2Cl_2$ (25 mL) and the solution washed with $H_2O$ (3 x 15 mL) to remove excess ($N(C_4H_9)_4$)NCS. The organic layer was concentrated under reduced pressure giving a red-orange oil. Sonication of the oil in the presence of diethyl ether induced precipitation of an orange solid. The solid was filtered and washed with copious amounts of diethyl ether then dried *in vacuo* giving compound **5** as a yellow solid. Yield: 37%. $^1$H NMR (300 MHz, $CD_2Cl_2$): δ 9.40 (d, 2H, *J* = 6.0 Hz), 8.55 (d, 2H, *J* = 1.5 Hz), 8.32 (d, 2H, *J* = 1.5 Hz), 7.86 (dd, 2H, *J* = 6.0, 1.8 Hz), 7.35 (dd, 2H, *J* = 8.1, 1.8 Hz), 6.23 (d, 2H, *J* = 7.8 Hz), 4.25 (d, 4H, *J* = 6.6 Hz), 4.00 (d, 4H, *J* = 6.6 Hz), 3.19 (t, 8H, *J* = 8.4 Hz) 2.19 (sp, 2H, *J* = 6.6 Hz), 2.01 (sp, 2H, *J* = 6.6 Hz), 1.65 (m, 8H), 1.40 (sex, 8H, *J* = 7.2 Hz), 1.09 (d, 12H, *J* = 6.9 Hz), 0.98 (t, 12H, *J* =

7.2 Hz), 0.96 (d, 12H, $J$ = 6.9 Hz). HRESIMS m/z expected [$M^+$] = 1017.2543, m/z observed [$M^+$] = 1017.2600.

## 2.3 Results and Discussion

N3-like ruthenium complexes with isobutyl ester groups in place of the acid functionality were synthesized from a two-step reaction. Rawling and coworkers used isobutyl esters to synthesize and isolate the pure NN ester analogue to N3, which they were able to hydrolyze to N3.[50] We took advantage of the isobutyl protecting groups to synthesize and isolate the NS ester-analogue to N3. The ester substituents allow for the large-scale purification of the complexes through straightforward silica gel column chromatography. To synthesize the intermediate ruthenium complex *cis*-Ru($^i$buBpy)$_2$Cl$_2$ (**R1**) the glucose reaction[53] was used as opposed the widely used DMF method.[54, 55] In this reaction, glucose and ascorbic acid are used as the reducing agents instead of DMF. Therefore, the reaction can be done in a range of aqueous organic solvents opening up the possibility to use wider range of substituted bipyridines. By modifying the synthesis conditions for the second reaction, particularly the choice of solvent and thiocyanate salt, it is possible to optimize the amount of each isomer formed.

In the second substitution reaction to produce the thiocyanato complexes, the NCS precursor and solvent was modified to determine the best reaction conditions, which can be seen in Table 2.1. Depending on reaction conditions, one to three unique ruthenium complexes were isolated and characterized. On the basis of the evidence discussed below, the three complexes are described as linkage isomers of the two NCS ligands (doubly N-bound **1**, and N- and S-bound **2**) and a monosubstituted thiocyanate

complex **3** (Figure 2.1). The isomeric ratio was found to depend on the reaction conditions, particularly solvent polarity and thiocyanate salt counterion identity. When a polar solvent like ethanol is used, the reaction times are significantly decreased compared to the less polar tetrahydrofuran (THF), due to a stabilization of the dissociation products, while still allowing for the isolation of **2**. With ethanol and ammonium thiocyanate, appreciable amounts of the linkage isomer **2** can be isolated. However, using the more polar ethanol, the monosubstituted complex **3** is not observed in appreciable quantities to isolate. When AgNCS is used as the thiocyanate source, particularly when THF is used as the solvent, the yield of the NN fraction increases at the expense of the other fractions when compared to $NH_4NCS$. Also, the monosubstituted complex **3** is not observed when AgNCS is used under these reaction conditions. Overall, this supports that **2** is the kinetic product and can be isolated due to the lower temperatures of the THF reaction and the shorter reaction times of the ethanol reaction.[9]

In the process of isolating the linkage isomers, we were also able to isolate the monosubstitued thiocyanate complex **3**. This complex proves to be a valuable intermediate in the preparation of more structurally diverse ruthenium complexes. To gauge its potential use as a reactive intermediate, **3** was treated with AgOTf in acetonitrile, which produced the mono-solvento species. The solvento species was then substituted by the addition of pyridine, giving complex **4**. This reaction and the use of this intermediate can be extended to introduce further complexity into mono-substituted thiocyanato ruthenium complexes.

There are currently few examples in the literature of iridium dyes for DSSCs despite their potential benefits compared to ruthenium.[56] In a similar fashion to the ruthenium complexes described above, an iridium analogue to N3 was synthesized. The ligand bis(2-methylpropyl)-phenylpyridine-3,4′-dicarboxylate (**L6**) was prepared in high yield by a Suzuki cross-coupling reaction of 3-(methoxycarbonyl) phenylboronic acid and 2-bromo-4-methylcarboxylate-pyridine, before being transesterified to the isobutyl ester. The cyclometalated iridium dimer **I1** was prepared in isobutanol to protect the ester groups on the phenylpyridine in 68% yield. By using isobutanol as the solvent, the possibility of ester cleavage or transesterification reactions are minimized. This is an important aspect because the iridium complex is refluxed for 24 hours and produces stoichiometric amounts of acid capable of cleaving the ester protecting groups. This is not an issue in the ruthenium synthesis because the reaction is complete in under an hour and acid is not produced. The iridium dimer was then cleaved by the addition of AgOTf in acetonitrile to produce the bis-solvento species, which was then treated with tetrabutylammonium thiocyanate to produce the desired final complex **5**. In the iridium system, only one isomer was observed, unlike the ruthenium system. The reaction conditions, including, the use of silver triflate, solvent, thiocyanate salt, reaction time, and temperature, were further modified to try to produce linkage isomers. However all attempts produced either **5** or some combination of uncleaved iridium dimers and/or cleaved esters on the phenylpyridines, which made purification attempts difficult.

Figure 2.2 shows the $^{1}$H NMR spectrum of complexes **1** and **2** in the aromatic and alkyl regions in addition to **R1** and **3** for comparison. The spectrum of **2** appears more

complex than the spectrum of **1** from a loss of symmetry due to one NCS being N-bound and the other being S-bound. Also the doublet of a doublet at 9.75 ppm in the spectrum of **1**, which corresponds to the 6 hydrogens on the trans pyridine rings, is split into two doublets of doublets at 10.08 and 9.60 ppm when one of the ligands is S-bound as in the spectrum of **2.** These two protons each show strong coupling (5.9 Hz) to the ortho hydrogen 5 and weak coupling (0.6 Hz) to the para hydrogen 3. In this case, one of the hydrogens is above an N-bound thiocyanate and one is above an S-bound thiocyanate, giving two separate peaks. The proton peak for the S-bound isomer is expected to be shifted downfield from the N-bound isomer.[9] The splitting of the peak furthest downfield is also observed in the spectrum of **3** indicating a change in the coordination environment around the metal center. On the basis of $^{1}$HMNR, the iridium complex **5** shows the resonances of only one linkage isomer, which is believed to be the doubly N-bound complex.

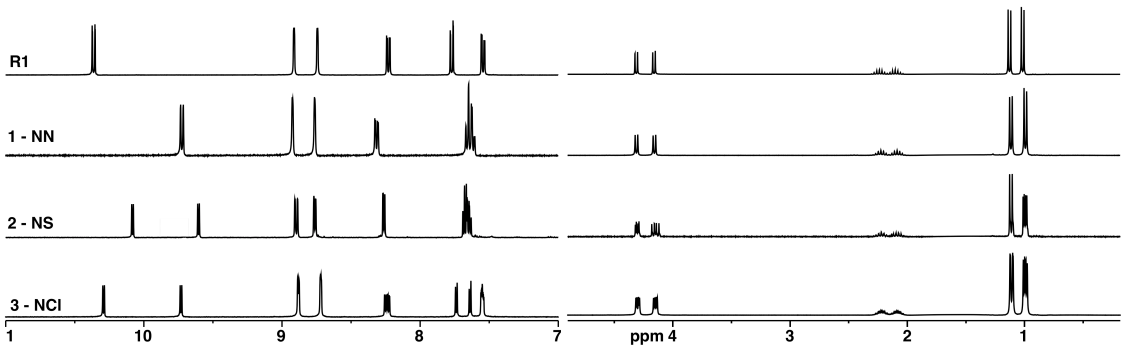


**Figure 2.2: $^{1}$H NMR of R1, and 1-3 in $CD_2Cl_2$. Note: The intensity of the aromatic region is scaled by a factor of 7 compared to the intensity of the alkyl region to better show the peaks.**

Figure 2.3 shows the $^{13}C$ NMR spectra of complexes **1** and **2** in the region of the spectrum where a carbon in an S-bound NCS ligand would appear (120-125 ppm).[10] When the NCS ligand is bound to a metal through the sulfur, it shields the carbon more than when it is nitrogen bound, therefore this peak appears upfield compared to the N-bound NCS carbon (135-140 ppm). The $^{13}C$ NMR spectrum of **2** shows a peak at 120.6 ppm, which we assign to the carbon of an S-bound thiocyanate. The $^{13}C$ NMR spectrum of **1** does not show the peak around 120 ppm, but it does show a peak at 136.5 ppm, which we assign to the carbon of an N-bound thiocyanate. The carbon peak of an N-bound thiocyanate is obscured in the spectrum of **2** by additional bipyridine peaks that are not present in the spectrum of **1**. However, on the basis of the carbon peak at 120.6 ppm, we can assign **1** as being doubly N-bound and **2** as being a mixture of N- and S-bound thiocyanates. In addition, the mono-substituted complexes **3** and **4** are N-bound on the basis of the $^{13}C$ NMR not having the peak at 120.6 ppm.

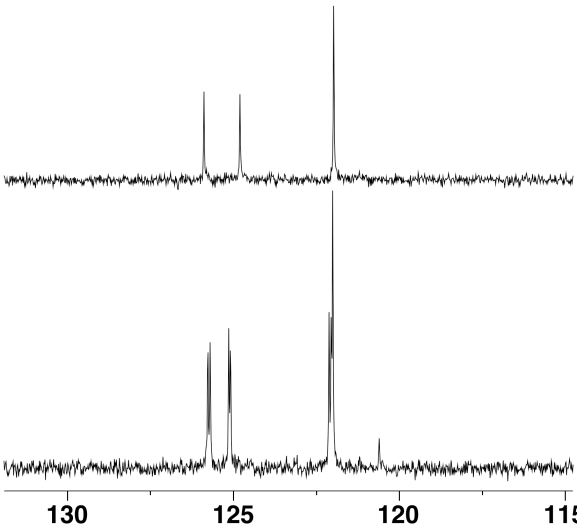


**Figure 2.3: $^{13}C$ NMR of 1-NN (top) and 2-NS (bottom) in $CD_2Cl_2$. The peak at 120.6 ppm in the bottom spectrum corresponds to the carbon in an S-bound NCS.**

The $^{1}H$ and $^{13}C$ NMR show the presence of two unique complexes. To further prove **2** is the NS linkage isomer, high-resolution ESI mass spectrometry was used. Figure 2.4 shows the mass spectrum for complexes **1** and **2**. Since the complexes are linkage isomers, the same mass is expected for both complexes (m/z [M + $Na^+$ ]= 953.1916 for both complexes). Indeed, the two complexes show the exact same m/z of 953.1921, indicating that in combination with the NMR data, the complexes are in fact linkage isomers of NCS.

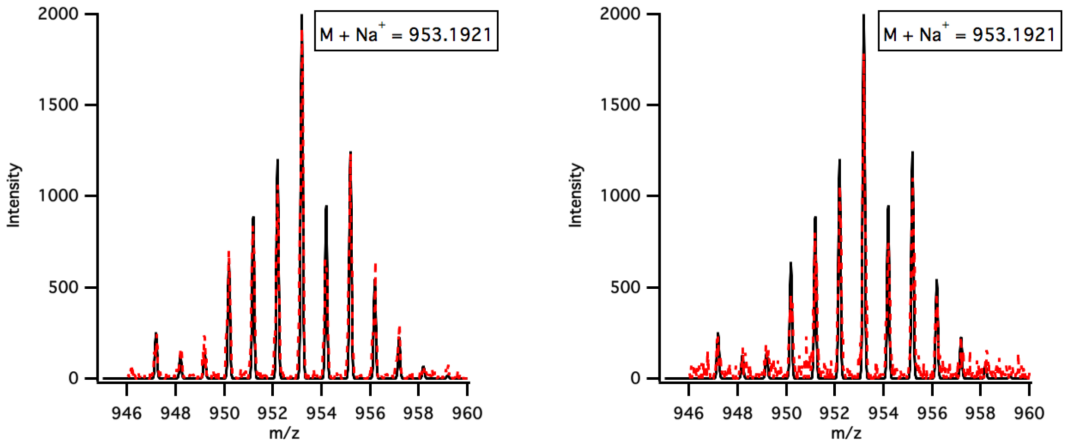


**Figure 2.4: High-resolution ESI mass spectrum of 1-NN (right) and 2-NS (left) ruthenium complexes. The expected m/z [M + Na+] = 953.1916 for both complexes.**

Figure 2.5 shows ATR-IR spectroscopy, which was used to study the C-N stretching region. The doubly N-bound complex **1** has a sharp CN stretch at 2112 $cm^{-1}$ while the mixed isomer **2** has a broad CN stretch centered at 2102 $cm^{-1}$. The C-N stretching band is expected to appear at slightly higher frequency (2108 $cm^{-1}$) for an S-bound NCS compared to the N-bound NCS (2102 $cm^{-1}$).[48, 49, 57, 58] However, this is not

always the case as Grätzel and Schreiner argue that an N-bound thiocyanate appears at higher frequency than an S-bound species.[9, 59] The consensus is that it can be difficult to determine the bonding mode of the thiocyanate ligand using infrared spectroscopy as the two frequencies tend to overlap. Since **2** has both an N- and S- bound NCS, it is not possible to resolve the individual peaks.[49] In addition, the peak corresponding to the S-bound NCS is easily obscured by the stronger absorption of the N-bound NCS. The IR spectrum of **2**, where both binding modes are present, shows a broader absorption compared to the doubly N-bound spectrum of **1**. The shoulder present in **1** can be assigned to free thiocyanate. The iridium complex **5** shows a sharp CN stretch at 2099 $cm^{-1}$, which would indicate only one thiocyanate bonding mode present.

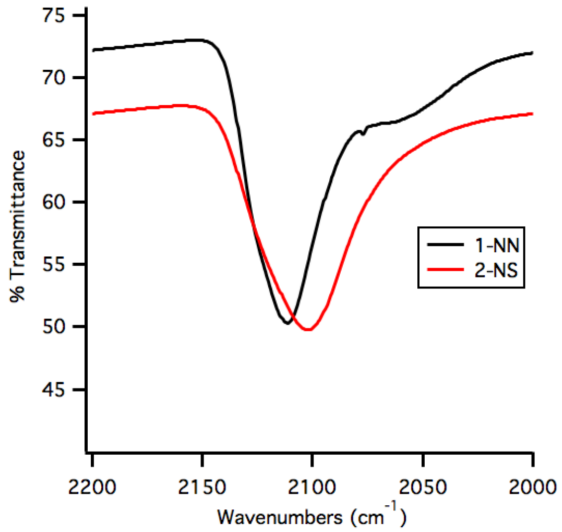


**Figure 2.5: Attenuated total reflectance (ATR) infrared spectrum of 1-NN (black) and 1-NS (red) ruthenium complexes in the C-N stretching region.**

The two isomers give distinct UV/Vis spectra when dissolved in methylene chloride. Figure 2.6 shows the molar absorptivity of complexes **1-4** in the UV/visible

region and Table 2.2 lists complex specific data. The complexes have a sharp, intense absorptions around 315 nm corresponding to the bipyridine π -π* transition. In the visible region, all complexes have two broad absorptions from 400-600 nm, with the peaks around 400 nm and 560 nm attributed to the metal to ligand (π*-bpy) transition (MLCT). The MLCT has a molar extinction coefficient of 14,400 $M^{-1}$ $cm^{-1}$ at 565 nm for the doubly N-bound complex **1** and 10,200 $M^{-1}$ $cm^{-1}$ at 560 nm for complex **2**. For comparison, N719 has two broad absorptions at 535 and 395 nm with molar absorptivities of 14,700 and 14,300 $M^{-1}$ $cm^{-1}$ respectively. In the case of N3, the doubly N-bound thiocyanate is the desired isomer and it has been proposed that the N- and S- bound isomer is less efficient for light harvesting. Our absorption data shows that when the thiocyanate is doubly N-bound, it absorbs 30% more light at the lowest energy MLCT than when the thiocyanate is bound through the S. In addition, the MLCT is red-shifted by 5 nm in the doubly N-bound complex. Complex **4** has a similar absorption spectrum, although it is shifted to higher energy by about 40 nm as a result of its cationic nature.

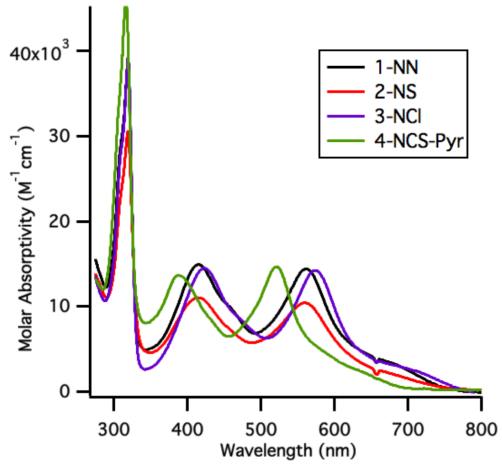


**Figure 2.6: Molar absorptivity of complexes 1-4 in $CD_2Cl_2$.**

For comparison purposes, the absorption spectrum of **5** is also presented in Table 2.2 with the ruthenium isomers. In typical iridium complexes, the absorption tails off at 450 nm, however **5** shows charge transfer absorptions red shifted to 500 nm. This complex though absorbs only 10% of the light compared to the corresponding ruthenium complexes at the lowest energy transition.

**Table 2.2: Spectroscopic and electrochemical data for the metal complexes 1-5.**

| Sample | $\lambda_{abs}$ (nm)[a] | | | $E_{1/2}Ru^{III}/Ru^{II}$ | $E_{Red}RuL_3^{2+}/RuL_3^{1+}$ | $E_{Red}RuL_3^{1+}/RuL_3^{0}$ |
|---|---|---|---|---|---|---|
| | $\varepsilon$ ($10^3$ $M^{-1}cm^{-1}$) | | | (V/NHE)[c] | (V/NHE)[d] | (V/NHE)[d] |
| **1 -** NN | 318 | 415 | 565 | 0.90 | -1.05 | -1.28 |
| | 38.7 | 15.0 | 14.4 | | | |
| **2 -** NS | 315 | 413 | 560 | 0.86 | -1.05 | -1.26 |
| | 30.6 | 11.0 | 10.2 | | | |
| **3 -** NCl | 318 | 422 | 574 | 0.77 | -1.11 | -1.39 |
| | 39.3 | 14.5 | 14.2 | | | |
| **4 -** NCS-Pyr | 316 | 388 | 520 | 0.85 | -1.06 | -1.41 |
| | 46.1 | 13.7 | 14.7 | | | |
| **5 -** Ir-NCS | 319-sh | 370-sh | 490 | 0.54 | -0.82 | -0.97 |
| | 20.0 | 7.32 | 1.50 | | | |

Cyclic voltammetry data, shown in Table 2.2, was used to analyze the redox processes in the complexes. In their as-synthesized forms, **1-4** show reversible $Ru^{II}/Ru^{III}$ oxidations between 0.77 – 0.90 V/NHE and two reversible bipyridine reductions. The first reduction is between -1.05 and -1.11 V and the second reduction between -1.26 and -1.41 V. As seen in Figure 2.7, **1** and **2** have very similar electrochemical properties, with **1** being harder to oxidize by 0.04 V and having the same reduction properties. The iridium complex **5** has two reversible oxidations, an $Ir^{III}/Ir^{IV}$ at 0.54 V and $Ir^{IV}/Ir^{V}$ at 0.91

V. Similar to the ruthenium system, **5** has two quasi-reversible ligand reductions at -0.82 V and -0.97 V.

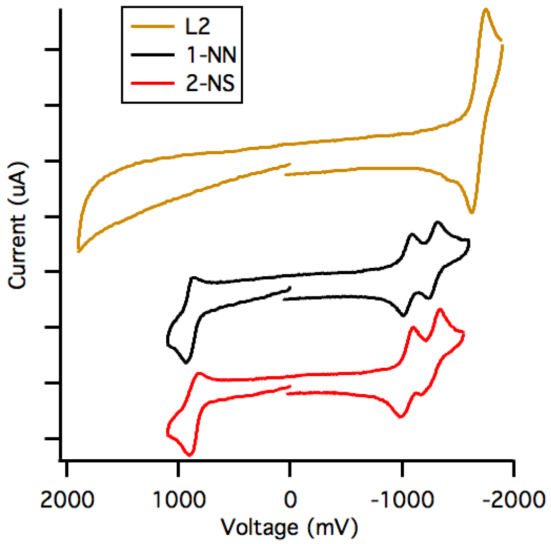


**Figure 2.7: Cyclic voltammogram of L2 (brown), 1-NN (black), and 2-NS (red) in acetonitrile with tetrabutylammonium hexafluorophosphate as the supporting electrolyte with a scan rate of 300 mV/s positive to negative scan.**

The experimental isomerism of **2** was studied by first dissolving the complex in deuterated methanol and monitoring the $^{1}$HNMR of over the course of a week. The NMR tube was left at room temperature and in the light, at which point a precipitate formed over time. After 300 hours, the solution was decanted and an NMR of the precipitate in deuterated methylene chloride revealed complex **2** and not an isomerization product as expected. Complex **2** is slightly solutble in methanol and slowly precipitated over time. A similar experiment was attempted with methylene chloride instead of methanol,

however **2** failed to isomerize on the time scale monitored. Complex **2** was then dissolved in deuterated DMSO and the NMR spectrum was monitored every 5 minutes for 900 total minutes at 80 °C. Figure 2.8 shows the spectral changes of the downfield peaks as the mixed isomer **2**, isomerizes into the doubly N-bound species **1**. The intensity of the peaks at 9.85 and 9.45 ppm, which correspond to proton $6_1$ and $6_2$ in the mono S-bound species decrease, while the peak at 9.51 ppm, which corresponds to the 6 hydrogens in a doubly N-bound system, increases. The process is complete in 200 minutes and the spectrum remains constant for the remainder of the experiment. Figure 2.9 shows the initial and final spectra (Note: the initial spectrum is at 80 °C and the final spectrum is at room temperature) of **2** as well as **1** in DMSO for comparison. From Figure 2.9 it is evident that **2** isomerizes to **1**, which is stable at elevated temperatures for an extended period of time.

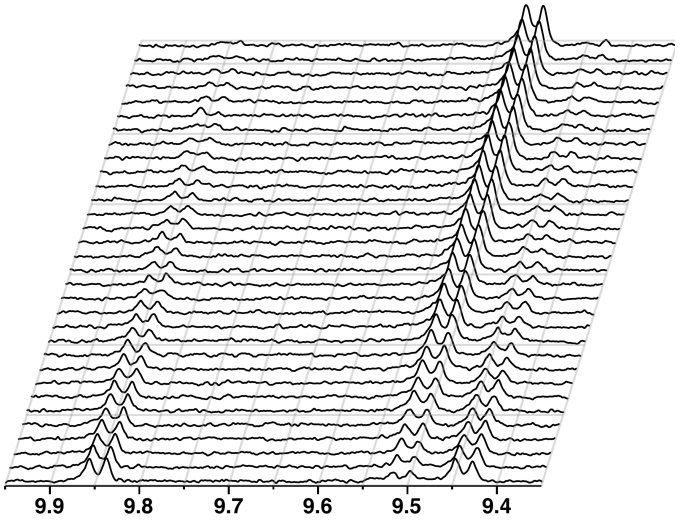


**Figure 2.8: $^1$H NMR spectrum in DMSO- $D_6$ of the downfield peaks during the kinetic isomerization of 2-NS at 80 °C over the first 200 minutes. The initial spectrum is on the bottom and spectrum 31 on the top.**

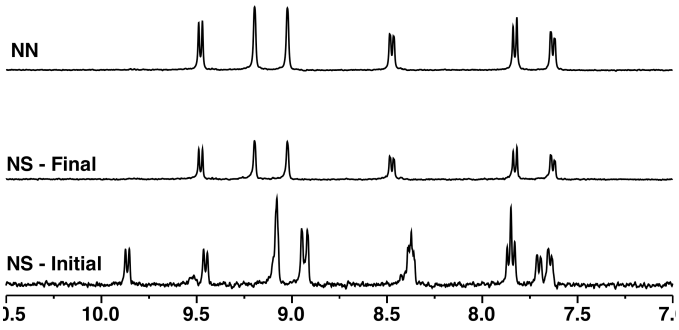


**Figure 2.9: $^1$H NMR in DMSO-$D_6$ of the aromatic region of 2-NS before and after the isomerization at 80 °C and a spectrum of 1-NN in DMSO for comparison.**

The reaction was followed by $^1$HNMR in a sealed tube; therefore a first-order kinetic plot can be generated from the integration of subsequent spectra. The peak at 9.85 ppm was monitored because it is known to be characteristic of **2** and does not overlap with any other peaks associated with **1**. Figure 2.10 shows a plot of ln [**2**] versus time over 3.5 half-lives, which was fit to a linear line with a slope of -0.00842. From the slope, the rate constant was found to be 0.00842 $min^{-1}$, which corresponds to a $t_{1/2}$ = 82 minutes at 80 °C. The first-order nature of the isomerization from NS to NN suggests either a dissociation or solvent assisted ligand exchange.[36] With no evidence of a solvento species intermediate in the NMR data, a fully dissociative mechanism is most probable and is assisted by the polar DMSO solvent.

The linearity of the plot indicates a simple first-order isomerization, however a reversible reaction should also be considered. The [**2**]/[**2**]$_o$ versus time was also plotted. In this type of plot, if the data levels off at zero, then the reaction is said to proceed to completion; however if the data levels off at any value greater than zero, then the reaction is said to reach an equilibrium mixture. In our plot of [**2**]/[**2**]$_o$ versus time, the data does in

fact level off at zero, indicating the isomerization went to completion. The initial slope of this plot is -0.00861 $min^{-1}$, which is the sum of $k_1 + k_{-1}$. Therefore, within experimental error, the reverse reaction and $k_{-1}$ (0.00019) do not contribute to the overall rate and isomerization of **2**. With a limited amount of material only one kinetic experiment was completed and it is difficult to discount an equilibrium process in which a small amount of **2**, undetectable by NMR, is still present.

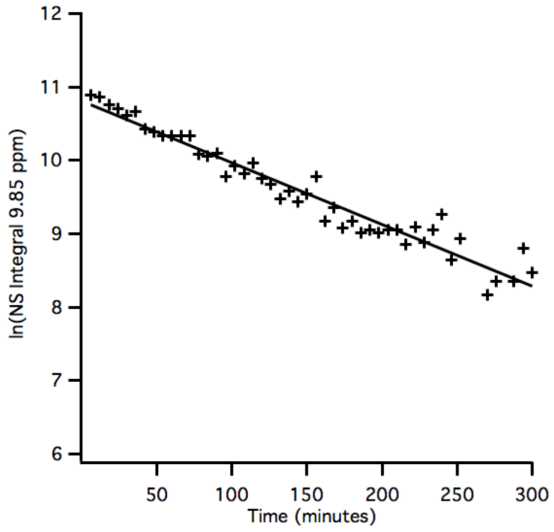


**Figure 2.10: First order kinetic plot of ln[2-NS] versus time over 3.5 half-lives, where [2-NS] is determined by the integration of the peak at 9.85 ppm. The rate constant was found to be 0.00842 $min^{-1}$.**

The ability to cleave the isobutyl esters is an important aspect of the synthesis, as noted by McDonagh.[50] The linkage isomers of N3 were prepared by hydrolyzing the ester groups at room temperature with tetra-n-butylammonium hydroxide, followed by acidification. In the case of the doubly N-bound complex **1**, the ester groups were hydrolyzed giving N3. However, in the case of the linkage isomer **2,** the hydrolysis led to a mixture of the two isomers. Figure 2.11 shows the $^1$HNMR of hydrolyzed forms of **1**

and **2**. Analysis of the spectrum of **1** including peak assignments and integrations indicate that it is the only isomer present. However, when looking at the spectrum of **2**, an additional peak is present at 9.65 ppm, which overlaps with the peak furthest downfield in the hydrolyzed form of **1**. This is in contrast to Figure 2.2 in which the NS isomer **2** has two peaks downfield of 9.5 ppm. All of the other peaks associated with **2** overlap with peaks present in **1**. Analysis of the integration values indicate that 40% of the hydrolyzed product of **2** has isomerized to the doubly N-bound product **1**. In addition to the high-temperature isomerization of **2**, isomerization is also possible through chemical reaction.

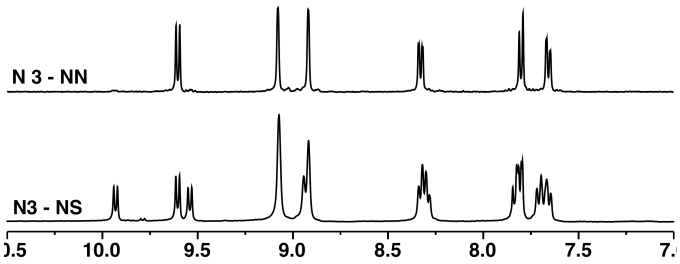


**Figure 2.11: $^1$H NMR in $CD_3OD$ of the hydrolyzed complexes 1-NN and 2-NS.**

## 2.4 Conclusions

We have synthesized and isolated ruthenium complexes **1** and **2** that display linkage isomerism in the thiocyanato ligands by changing the reaction conditions. Through column chromatography, complexes **1** and **2** were isolated in their pure forms and characterized spectroscopically. Through these techniques, **1** was assigned as the doubly N-bound thiocyanate complex, while **2** was assigned as the linkage isomer with one N-bound and one S-bound thiocyanate. The kinetic isomerization of **2** was followed

by NMR spectroscopy and found to be a first order process with a rate constant of 0.00842 $min^{-1}$ at 80 °C. In addition, a mono-substituted complex **3** was isolated and characterized. The substitution properties of **3** were explored as complex **4** was synthesized. An iridium analogue **5** of the ruthenium complexes was also synthesized. In the iridium system, through repeated attempts, linkage isomers were unable to be synthesized or isolated.

# 3 Electron-Rich Ruthenium-Bipyridine Complexes for Dye-Sensitized Solar Cell Applications

The effects on electron donating amino-substituted bipyridine ligands on the properties of $[Ru(amino_2bpy)_2(dcb)](PF_6)_2$ (deabpy = 4,4'-bis(diamino)-2,2'-bipyridine, dcb = 4,4'-dicarboxy-2,2'-bipyridine) complexes has been investigated. A series of amino substituted bipyridines, including diethylamino, pyrrolidino, piperidino, morpholino, and 1-methylpiperazino, and the corresponding ruthenium complexes have been synthesized and characterized. These complexes were used to study dye attachment and charge injection behavior into ZnO nanocrystal dispersions as the excited state oxidation potential of the dye was modified. In addition, Incident photon-to-current conversion efficiencies were measured on $TiO_2$ electrodes and compared to the dispersion results.

## 3.1 Introduction

Dye-sensitized solar cells (DSSC) utilizing sensitized metal oxide films have emerged as promising options for solar energy conversion due to low costs and increasing efficiencies.[3, 5] Interfacial electron transfer from the photoexcited state of the sensitizer dye to the conduction band of the metal oxide semiconductor is an important event leading to charge separation in dye-sensitized solar cells.[3, 27, 60] The dynamics of this process have been examined with a variety of time-resolved and steady-state spectroscopic methods on metal oxide nanocrystal films.[22, 60-62] However, the heterogeneous nanocrystal surface environment complicates electron transfer dynamics, where multiple injection time scales for a given sensitizer have been observed (<100 fs to >100 ps).[61, 63-69]

In this regard, a homogenous sample of dye:nanocrystal dispersions can be used to simplify the system, which should allow for a detailed investigation of interfacial charge transfer and a more consistent comparisons between systems. This has recently been done using $TiO_2$ dispersions, where injection times were too fast to be measured accurately.[19, 22] Zinc oxide (ZnO) offers similar properties to $TiO_2$, but has the added advantage that many synthetic routes lead to monodispersed nanocrystals which are stable as a dispersion in common solvents and are optically clear. Hence, a homogeneous sample of dye-coated ZnO NC dispersions can be used to model the dye-sensitized solar cell.

Sensitizer molecules derived from ruthenium-polypyridyl complexes have been an attractive choice due to the intense absorption bands in the visible region of the spectrum, long-lived excited states, photostability, and sensitivity to synthetic substitution

to induce changes in redox and spectral properties. Recent work by our group has shown that the excited state (-1.6 V/NHE) of a terthiophene acid dye is quenched on 3 nm ZnO nanocrystal dispersions, while the excited state (-0.78 V) of $Ru(bpy)_2(dcbpy)$ is not.[70, 71] This research consists of studying ruthenium complexes of the form $[Ru((R_2N)_2bpy)_2(dcbpy)]^{2+}$ (where $(R_2N)_2bpy$ = 4,4'-diamino-2,2'-bipyridine, dcbpy = 4,4'-dicarboxy-2,2'-bipyridine), which will be anchored to ZnO NCs dispersions and $TiO_2$ nanocrystalline films. These complexes, shown in Figure 3.1, were designed to have two 4,4'-diamino-2,2'-bipyridine ligands to raise the excited state reduction potential of the complex, which will allow for efficient electron injection into ZnO NC dispersions. The third ligand is 4,4'-dicarboxylic acid-2,2' bipyridine which will act as the anchoring group to the surface of the metal oxide. Using these complexes, well-defined dye-coated ZnO NC dyads were studied using NMR, UV-visible spectroscopy, and steady state fluorescence to analyze dye binding, photoluminescence quenching of the excited dye, and the subsequent electron injection at different concentrations of ZnO NCs. In addition, the incident photon-to-current conversion efficiency (IPCE) of sensitized $TiO_2$ films was studied and compared to N3, which has shown the largest conversion efficiencies to date (~11.2%) of ruthenium dyes, making it the standard for comparison for all new ruthenium sensitizers.[12]

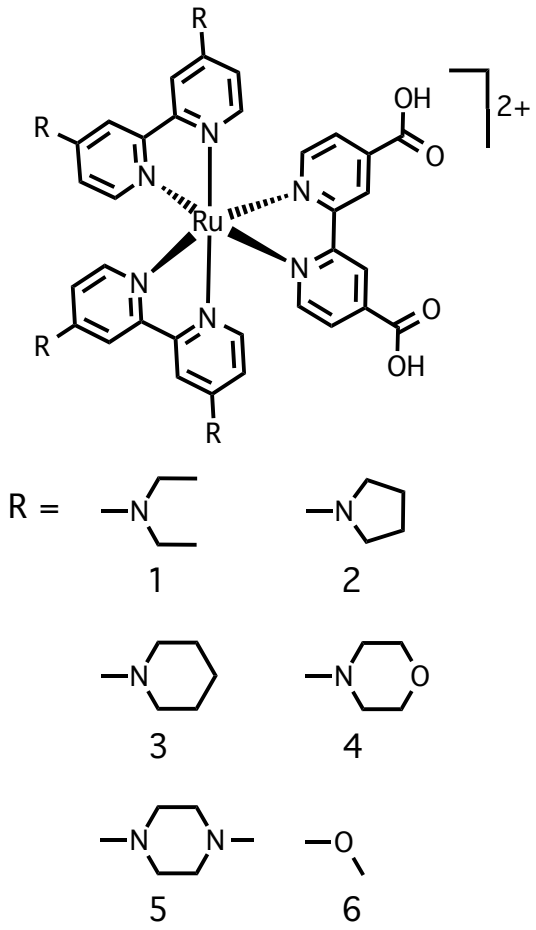


**Figure 3.1: Molecular structure of the subsituted tris-bipyridine ruthenium cpmplexes 1-6. 1-Cl replaces the diacid functionality with the dichloro functionality.**

## 3.2 Experimental

### 3.2.1 Materials

Ruthenium (III) chloride trihydrate ($RuCl_3 \cdot 3H_2O$) was purchased from Pressure Chemical Company and used as received. Spectroscopic grade methanol, 2,2'-bipyridine, 4,4'-dimethyl-2,2'-bipyridine, diethylamine, pyrrolidine, piperidine, morpholine, thiomorpholine, 1-methylpiperazine, tetramethylammonium hydroxide ($NMe_4OH \cdot 5H_2O$), and zinc acetate ($Zn\text{-}(CH_3COO)_2 \cdot 2H_2O$), were purchased from

Sigma Aldrich and used as received. P25 $TiO_2$ nancrystal powder was purchased from DeGussa and used as received. All additional solvents were dried (unless water was used as a co-solvent) and deoxygenated before use, and all procedures were performed using standard Schlenk techniques. 4,4'-Dicarboxylic acid-bipyridine, 4,4'-dichloro-2,2'-bipyridine-N,N'-dioxide, and 4,4'-dichloro-2,2'-bipyridine were prepared according to literature procedures.[51, 72, 73] N3 was synthesized according to literature methods.[50]

### 3.2.2 Methods

All NMR spectra of the complexes and ligands were taken on a Varian Inova 300 MHz spectrometer and chemical shifts were referenced to the residual solvent peak. All NMR spectra of dye:ZnO dyads were taken on a Varian Inova 500 MHz spectrometer and chemical shifts were referenced to the residual solvent peak. All mass spectral data taken on a Bruker BioTOF II in ESI-TOF mode. Electronic absorption spectra were collected on an Ocean Optics DH-2000-BAL spectrometer. The steady-state emission spectra were recorded on a Spex Fluorolog 1680 0.22 m double spectrometer equipped with a xenon source. Fluorescence spectra were corrected to compensate for changes in the instrument's sensitivity at longer wavelengths. UV-visible and fluorescence spectroscopic measurements were performed in quartz cuvettes with a 3 mm path length unless otherwise noted. The IR spectra of ruthenium complexes (KBr pellet) were recorded on a Nicolet MAGNA-IR 560 spectrometer. Cyclic voltammograms were obtained on a BAS-100B electrochemical analyzer using methods previously described.[52] All solutions were prepared in acetonitrile or dimethylformamide with 0.1 M tetrabutylammonium hexafluorophosphate ($TBA^+$ $PF_6^-$) as the supporting electrolyte and degassed with argon. Reported E° potentials were referenced to a Ag/AgCl electrode and

are reported versus NHE. UV-vis spectroelectrochemical measurements were performed in a specular reflectance thin layer (0.2 mm) cell using a BAS-100B bulk electrolysis system. Solutions were prepared identically to those in the electrochemistry experiments, and spectra in the UV-vis region were recorded using an Ocean Optics USB4000 spectrometer.

### 3.2.3 ZnO Nanocrystal (NC) Synthesis[74]

To a 0.1 M solution of $Zn(CH_3COO)_2 \cdot 2H_2O$ (25 mL, 2.51 mmol) in DMSO, a 0.55 M solution of $NMe_4OH \cdot 5H_2O$ (7.73 mL, 4.25 mmol) in ethanol was added dropwise over the course of 30-180 s and allowed to stir at room temperature (ca. 24 °C) for up to 30 minutes. The longer reaction times led to larger particles. The diameters were determined using electronic absorption spectra.[75] To induce precipitation, an aliquot of the solution was removed and added to three times the volume of ethyl acetate. The turbid mixture was centrifuged using a LW Scientific Ultra-8V centrifuge. After the liquid was decanted, the white pellet was dispersed in a minimum of ethanol and precipitated a second time. The purified ZnO NCs were dispersed in methanol to yield an optically clear dispersion. To obtain a mass of ZnO, a known volume of the dispersion was evaporated and then heated to 500 °C for an hour to burn off all organics. A typical yield for the reaction is 78-80%.

### 3.2.4 Sample Preparation: Steady State Absorption, Emission and NMR

In all samples the amount of dye was held constant throughout the experiment and the amount of ZnO was varied in subsequent samples. In a typical experiment, aliquots of $3.0 \times 10^{-4}$ M ZnO nanocrystals (3.0 nm in diameter) dispersed in methanol was added to $1.0 \times 10^{-3}$ M dye in methanol. The samples were then diluted to a total volume of 1.2 mL

with methanol. Samples were allowed to equilibrate for 2h before any measurements were taken. Methanol-$d_4$ was used for the NMR experiments.

### 3.2.5 Device Construction and Characterization

Devices were prepared using a slight modifications literature reports.[7, 11, 76] Fluorine-doped tin oxide glass (10 ohm/square, F-$SnO_2$) was soaked in a 40 mM titanium tetrachloride ($TiCl_4$) solution at 70 °C for 30 minutes at which point a slurry of P25 $TiO_2$ was doctor-bladed onto a 1 $cm^2$ area. The films were dried at 120 °C for 10 minutes and then annealed at 500 °C for 20 minutes. The films were then treated with the $TiCl_4$ solution and again annealed at 500 °C for 30 minutes. Once cooled, the films were immersed in a 0.5 mM dye solution in ethanol for 24 hours. A platinum electrode was prepared by placing a drop of a 5 mM platinum tetrachloride solution in ethanol on the F-$SnO_2$ glass, allowed to dry, and annealed at 400 °C for 30 minutes. The electrolyte was prepared with: 0.60 M HMII ionic liquid, 0.03 M $I_2$, 0.10 M guanidinium thiocyanate, 0.50 M 4-tert-butylpyridine in 3 mL of acetonitrile:valeronitrile (85:15). Devices were characterized as previously reported.[77]

### 3.2.6 Synthesis of 4,4'-bis(diethylamino)-2,2'-bipyridine (L1)[51, 72]

4,4'-Dichloro-2,2'-bipyridine-N,N'-dioxide (0.60 g, 0.0023 mol) was added to 27 mL of 2:1 diethylamine/water and heated in a sealed autoclave with stirring for 22 hours at 135°C. The reaction was then cooled to room temperature and the solvent was evaporated. The crude brown oil was dissolved in dry, deoxygenated chloroform (~30 mL) to which 5 mL (0.047 mol, 20 eq) of phosphorus trichloride ($PCl_3$) was added at 0°C. The reaction was then refluxed for 3 h, cooled to room temperature, and poured onto ice (~200 g). The organic layer was separated from the aqueous layer and further

extracted with water (3 x 20 mL). The aqueous layers were combined and the volume was reduced to ~100 mL under vacuum. The reaction mixture was then basified with concentrated NaOH(aq) causing the desired compound to precipitate. The precipitate was filtered and washed thoroughly with water and dried under vacuum. **L1** was isolated as a grey solid by filtration to yield 0.57 g (82%). $^1$H-NMR (300 MHz; $CD_2Cl_2$): δ 8.21 (d, *J* = 5.9 Hz, 2H), 7.67 (d, *J* = 2.7 Hz, 2H), 6.49 (dd, *J* = 5.9, 2.8 Hz, 2H), 3.46 (q, *J* = 7.1 Hz, 8H), 1.22 (t, *J* = 7.1 Hz, 12H).

### 3.2.7 Synthesis of 4,4'-dipyrrolidino-2,2'-bipyridine (L2)

4,4'-Dichloro-2,2'-bipyridine-N,N'-dioxide (0.50 g, 0.0022 mol) was added to 40 mL pyrrolidine and the reaction was refluxed neat for 23 h. Using the same procedure as above, **L2** was isolated after treatment with $PCl_3$ as a light brown solid by filtration to yield 0.27 g (47%). $^1$H-NMR (300 MHz; $CDCl_3$): δ 8.29 (d, *J* = 5.7 Hz, 2H), 7.55 (d, *J* = 2.3 Hz, 2H), 6.40 (dd, *J* = 5.7, 2.4 Hz, 2H), 3.44 (t, *J* = 6.5 Hz, 8H), 2.05 (q, *J* = 6.5 Hz, 8H).

### 3.2.8 Synthesis of 4,4'-dipiperidino-2,2'-bipyridine (L3)

4,4'-Dichloro-2,2'-bipyridine-N,N'-dioxide (0.50 g, 0.0022 mol) was added to 50 mL piperidine and the reaction was refluxed neat for 23 h. After treatment with $PCl_3$, **L3** was isolated as a light brown solid by filtration to yield 0.50 g (80%). $^1$H-NMR (300 MHz; $CDCl_3$): δ 8.31 (d, *J* = 5.9 Hz, 2H), 7.85 (d, *J* = 2.7 Hz, 2H), 6.66 (dd, *J* = 5.9, 2.7 Hz, 2H), 3.44 (d, *J* = 4.9 Hz, 8H), 1.67-1.63 (m, 12H).

### 3.2.9 Synthesis of 4,4'-dimorpholino-2,2'-bipyridine (L4)

4,4'-Dichloro-2,2'-bipyridine-N,N'-dioxide (0.50 g, 0.0022 mol) was added to 50 mL morpholine, and the reaction was refluxed for 24 h. After treatment with $PCl_3$, **L4** was

isolated as a light brown solid by filtration to yield 0.47 g (74%). $^1$H-NMR (300 MHz; $CDCl_3$): δ 8.36 (d, *J* = 5.9 Hz, 2H), 7.88 (d, *J* = 2.6 Hz, 2H), 6.69 (dd, *J* = 5.9, 2.7 Hz, 2H), 3.86 (t, *J* = 4.9 Hz, 8H), 3.42 (t, *J* = 5.0 Hz, 8H).

### 3.2.10 Synthesis of 4,4'-di(N-methylpiperazino)-2,2'-bipyridine (L5)

4,4'-Dichloro-2,2'-bipyridine-1,1'-dioxide (0.50 g, 0.0022 mol) was added to 50 mL N-methylpiperazine and the reaction was refluxed for 22 h. After treatment with $PCl_3$, **L5** was isolated as a light brown solid by filtration to yield 0.61 g (90%). $^1$H-NMR (300 MHz; $CDCl_3$): δ 8.33 (d, *J* = 5.9 Hz, 2H), 7.87 (d, *J* = 2.5 Hz, 2H), 6.68 (dd, *J* = 5.9, 2.7 Hz, 2H), 3.47 (t, *J* = 5.1 Hz, 8H), 2.54 (t, *J* = 5.0 Hz, 8H), 2.35 (s, 6H).

### 3.2.11 Synthesis of 4,4'-dimethoxy-2,2'-bipyridine (L6)[72]

Solid 4,4'-dichloro-2,2'-bipyridine-N,N'-dioxide (1.50 g, 0.0058 mol) was added to freshly prepared sodium methoxide (0.025 mol) in dry methanol (75 mL). The yellow suspension was stirred at 60 ˚C for 5 h, resulting in a yellow solution. The reaction was cooled to 0°C and neutralized with concentrated sulfuric acid. The excess solvent was evaporated and the crude solid was dried under vacuum. The crude solid 4,4'-dimethoxy-2,2'-bipyridine-N,N'-dioxide was treated with $PCl_3$ as above to yield 1.0 g (80%) of **L6** as an off-white solid. $^1$H-NMR (300 MHz; $CD_2Cl_2$): δ 8.46 (d, *J* = 5.6 Hz, 2H), 8.01 (d, *J* = 2.6 Hz, 2H), 6.86 (dd, *J* = 5.6, 2.6 Hz, 2H), 3.94 (s, 6H).

### 3.2.12 Synthesis of [Ru((Et$_2$N)$_2$bpy)$_2$Cl$_2$]Cl (R1)

$RuCl_3$-3$H_2O$ (0.25 g, 1 mmol) was added to a solution of LiCl (1.7 g, 39 mmol) in ethylene glycol/water (25 mL, 4:1) at 110 ˚C. The LiCl was used to maintain a total $Cl^-$ ion concentration of 1.7 M. After 15 min, **L1** (0.60 g, 2.0 mmol) was added. After 12 min glucose (0.36 g, 2.0 mmol) was added and allowed to react for 10 min, at which point

ascorbic acid (0.089 g, 0.5 mmol) was added. The reaction solution was maintained at 110 ˚C for 30 min. The reaction was quenched with the addition of 10 mL of a saturated NaCl solution and cooled to 0°C for 60 min. The dark purple precipitate was filtered, washed with the NaCl solution, and purified on a neutral alumina column using methylene chloride/methanol (99:1) as the eluent to yield 0.30 g (37%) of **R1.** Paramagnetic **R1** did not display a useful NMR spectrum. Its composition was confirmed using mass spec. HR ESI-MS m/z (observed) 768.2724 ($M^+$), m/z (calculated) 768.2736.

### 3.2.13 Synthesis of [Ru((pyrrolidino)$_2$bpy)$_2$Cl$_2$]Cl (R2)

The same procedure was repeated with $RuCl_3$-$3H_2O$ (0.21 g, 0.8 mmol) and **L2** (0.50 g, 1.6 mmol). The dark dark purple precipitate was filtered and purified on a neutral alumina column using methylene chloride/methanol (99:1) as the eluent to yield 0.17 g (25%) of **R2.** HR ESI-MS m/z (observed) 760.2119 ($M^+$), m/z (calculated) 760.2110.

### 3.2.14 Synthesis of [Ru((piperidino)$_2$bpy)$_2$Cl$_2$]Cl (R3)

The same procedure was repeated with $RuCl_3$-$3H_2O$ (0.17 g, 0.7 mmol) and **L3** (0.45 g, 1.4 mmol). The dark purple precipitate was filtered and purified on a neutral alumina column using methylene chloride/methanol (99:1) as the eluent to yield 0.14 g (25%) of **R3.** HR ESI-MS m/z (observed) 816.2713 ($M^+$), m/z (calculated) 816.2736.

### 3.2.15 Synthesis of [Ru((morpholino)$_2$bpy)$_2$Cl$_2$]Cl (R4)

The same procedure was repeated with $RuCl_3$-$3H_2O$ (0.17 g, 0.7 mmol) and **L4** (0.45 g, 1.4 mmol). The reaction was quenched, and dark purple precipitate was filtered. Due to its limited solubility crude **R4** was used in the subsequent reaction. HR ESI-MS showed the presence of m/z 824.1890 ($M^+$), m/z (calculated) 824.1906.

### 3.2.16 Synthesis of $[Ru((piperazino)_2bpy)_2Cl_2]Cl$ (R5) and $[Ru((piperazino)_2bpy)_2((COOH)_2bpy)](PF_6)_2$:(5)

The glucose reaction was unsuccessful at producing **R5** as all products went directly to the tris-bipyridine ruthenium complex when **L5** was added. This was confirmed through NMR and ESI-MS as only the $[Ru((piperazino)_2bpy)_3]^{2+}$ complex was observed. The following alternative route started with $[[(n^6\text{-cymene})RuCl]_2(\mu\text{-}Cl)_2]$, which was prepared according to literature procedures.[13, 17] A mixture of $[[(\eta^6\text{-cymene})RuCl]_2(\mu\text{-}Cl)_2]$ (0.23g, 0.00038 mol, 1 eq), 4,4'dicarboxylic acid bipyridine (0.19 g, 0.00076 mol, 2 eq) in 80 mL DMF was heated to 65 ˚C for 4 h. Then excess **L5** (0.60 g, 0.0017 mol, 4.5 eq) was added and the reaction was refluxed for 4 additional hours, cooled to room temperature, and the solvent evaporated. The crude reaction mixture was dissolved in water, washed with methylene chloride (3 x 50 mL), and then metathesized to the hexafluorophosphate salt by adding $NaPF_6$ (0.015 mol, 20 eq) dissolved in a minimum volume of water. The precipitate was isolated by filtration and was washed with water and then acetone to yield 0.35 g (70%) of **5**. $^1$H-NMR (300 MHz; $D_2O$): δ 8.59 (s, 2H), 7.84 (d, *J* = 5.5 Hz, 2H), 7.65 (d, *J* = 18.9 Hz, 4H), 7.45 (d, *J* = 5.8 Hz, 2H), 7.21 (d, *J* = 6.6 Hz, 2H), 6.99 (d, *J* = 6.6 Hz, 2H), 6.68 (dd, *J* = 6.5, 1.1 Hz, 2H), 6.49 (dd, *J* = 5.3, 0.9 Hz, 2H), 4.24-3.96 (m, 8H), 3.58-3.37 (m, 8H), 3.38-3.14 (m, 8H), 3.13-2.93 (m, 8H), 2.79 (d, *J* = 4.6 Hz, 12H). HR ESI-MS m/z (observed) 525.2150 ($M^{2+}$), m/z (calculated) 525.2139.

### 3.2.17 Synthesis of $[Ru((methoxy)_2bpy)_2Cl_2]$ 2Cl (R6)

The same procedure was repeated with $RuCl_3$-$3H_2O$ (0.30 g, 1.3 mmol) and **L7** (0.54 g, 2.5 mmol). The purple/brown precipitate was filtered, dissolved in a warm 1:1 mixture of methanol:methylene chloride, and filtered a second time. The red/orange filtrate was

evaporated to yield 0.47 g (60%) of **R6.** $^1$H-NMR (500 MHz; $CD_3OD$): δ 9.57 (d, *J* = 6.3 Hz, 1H), 9.17 (d, *J* = 6.2 Hz, 1H), 8.22 (d, *J* = 1.2 Hz, 2H), 8.07 (d, *J* = 1.8 Hz, 2H), 7.44 (ddd, *J* = 28.0, 23.1, 5.5 Hz, 4H), 6.84 (d, *J* = 6.0 Hz, 2H), 4.14 (d, *J* = 12.8 Hz, 6H), 3.94 (d, *J* = 6.7 Hz, 6H). HR ESI-MS m/z (observed) 302.0120 ($M^{2+}$), m/z (calculated) 302.0109.

### 3.2.18 Synthesis of $[Ru((Et_2N)_2bpy)_2((COOH)_2bpy)](PF_6)_2$:(1)[78]

A mixture of **R1** (0.30 g, 0.38 mmol, 1 eq), 4,4'-dicarboxy-2,2'-bipyridine (0.27 g, 1.1 mmol, 3 eq), and triethylamine (0.90 mL, 6.4 mmol, 17 eq) was added to 25 mL of ethanol/water (4:1) and heated at reflux for 3 h. The solvent was evaporated and the resulting complex was purified on a Sephadex LH-20 column using acetonitrile/isopropanol (90:10) as eluent. The red solid was dissolved in a minimum of water and the desired complex was precipitated with the addition of excess $NaPF_6$ and isolated by filtration to give 0.37 g (80%) of **1.** $^1$H-NMR (300 MHz; $CD_3CN$): δ 9.48 (s, 2H), 8.07 (d, *J* = 5.9 Hz, 2H), 7.82 (dd, *J* = 5.9, 1.3 Hz, 2H), 7.38 (dd, *J* = 13.0, 2.7 Hz, 4H), 7.19 (d, *J* = 6.8 Hz, 2H), 6.90 (d, *J* = 6.8 Hz, 2H), 6.61 (dd, *J* = 6.8, 2.7 Hz, 2H), 6.40 (dd, *J* = 6.9, 2.7 Hz, 2H), 3.52 (m, *J* = 21.0, 7.0 Hz, 16H), 1.16 (dt, *J* = 18.6, 7.0 Hz, 24H). HR ESI-MS m/z (observed) 471.1930 ($M^{2+}$), m/z (calculated): 471.1921.

### 3.2.19 Synthesis of $[Ru((pyrrolidino)_2bpy)_2((COOH)_2bpy)](PF_6)_2$:(2)

Using the same procedure as above, **R2** (0.15 g, 0.18 mmol) was reacted with 4,4'-dicarboxy-2,2'-bipyridine (0.14 g, 0.56 mmol, 3 eq), and triethylamine (0.50 mL, 3.2 mmol, 17 eq). **2** was purified on a Sephadex LH-20 column using acetonitrile/methanol (90:10) as eluent to yield 0.17 g (75% yield). $^1$H-NMR (300 MHz; $CD_3OD$): δ 8.95 (s, 2H), 8.00 (d, *J* = 5.8 Hz, 2H), 7.73 (dd, *J* = 5.8, 1.5 Hz, 2H), 7.53 (dd, *J* = 11.5, 2.5 Hz,

4H), 7.27 (d, *J* = 6.6 Hz, 2H), 7.01 (d, *J* = 6.6 Hz, 2H), 6.53 (dd, *J* = 6.7, 2.5 Hz, 2H), 6.42 (dd, *J* = 6.7, 2.5 Hz, 2H), 3.56-3.37 (m, 16H), 2.16-2.00 (m, 16H). HR ESI-MS m/z (observed) 467.1614 ($M^{2+}$), m/z (calculated) 467.1608.

### 3.2.20 Synthesis of $[Ru((piperidino)_2bpy)_2((COOH)_2bpy)](PF_6)_2$:(3)

Using the same procedure as above, **R3** (0.13 g, 0.15 mmol) was reacted with 4,4'-dicarboxy-2,2'-bipyridine (0.11 g, 0.46 mmol, 3 eq), and triethylamine (0.37 mL, 2.6 mmol, 17 eq). **3** was purified on a Sephadex LH-20 column using acetonitrile/isopropanol (90:10) as eluent to yield 0.13 g (68% yield). $^1$H-NMR (300 MHz; $CD_3CN$): δ 9.10 (s, 2H), 8.14 (d, *J* = 5.9 Hz, 2H), 7.82 (d, *J* = 5.9 Hz, 2H), 7.65 (dd, *J* = 12.9, 2.4 Hz, 4H), 7.21 (d, *J* = 6.8 Hz, 2H), 6.93 (d, *J* = 6.8 Hz, 2H), 6.76 (dd, *J* = 6.8, 2.6 Hz, 2H), 6.56 (dd, *J* = 6.7, 2.3 Hz, 2H), 3.69-3.42 (m, 16H), 1.80-1.51 (m, 24H). HR ESI-MS m/z (observed) 495.1940 ($M^{2+}$), m/z (calculated) 495.1921.

### 3.2.21 Synthesis of $[Ru((morpholino)_2bpy)_2((COOH)_2bpy)](PF_6)_2$:(4)

Using the crude mixture of **R4** and an excess of 4,4'-dicarboxy-2,2'-bipyridine, the reaction was completed as above and **4** was purified on a Sephadex LH-20 column using acetonitrile/methanol (90:10) as eluent to yield 0.18 g (20% yield based on $RuCl_3$ from **R4** reaction). $^1$H-NMR (300 MHz; $CD_3CN$): δ 9.64 (s, 2H), 7.99 (d, *J* = 5.8 Hz, 2H), 7.80 (d, *J* = 6.0 Hz, 2H), 7.66 (dd, *J* = 10.7, 2.3 Hz, 4H), 7.28 (d, *J* = 6.7 Hz, 2H), 7.06 (d, *J* = 6.7 Hz, 2H), 6.75 (dd, *J* = 6.7, 2.3 Hz, 2H), 6.58 (dd, *J* = 6.7, 2.6 Hz, 2H), 3.76 (dt, *J* = 14.2, 4.7 Hz, 16H), 3.46 (dt, *J* = 19.2, 4.6 Hz, 16H). HR ESI-MS m/z (observed) 499.1517 ($M^{2+}$), m/z (calculated) 499.1506.

### 3.2.22 Synthesis of $[Ru((methoxy)_2bpy)_2((COOH)_2bpy)](PF_6)_2$:(6)

Using the same procedure as above, **R6** (0.47 g, 0.74 mmol) was reacted with 4,4'-dicarboxy-2,2'-bipyridine (0.55 g, 2.2 mmol, 3 eq), and triethylamine (1.50 mL, 11.1 mmol, 15 eq). Due to solubility, **7** was first converted to the $PF_6^-$ salt with $NaPF_6$ and purified on a Sephadex LH-20 column using acetonitrile/methanol (90:10) as eluent to yield 0.62 g (80% yield). $^1$H-NMR (300 MHz; $CD_3CN$): δ 9.02 (d, $J$ = 1.2 Hz, 2H), 8.03-8.00 (m, 6H), 7.80 (dd, $J$ = 5.9, 1.7 Hz, 2H), 7.50 (d, $J$ = 6.5 Hz, 2H), 7.36 (d, $J$ = 6.5 Hz, 2H), 7.00 (dd, $J$ = 6.5, 2.7 Hz, 2H), 6.89 (dd, $J$ = 6.6, 2.7 Hz, 2H), 3.99 (d, $J$ = 10.4 Hz, 12H). HR ESI-MS m/z (observed) 389.0683 ($M^{2+}$), m/z (calculated) 389.0662.

### 3.2.23 Synthesis of $[Ru((Et_2N)_2bpy)_2((Cl)_2bpy)](PF_6)_2$:(1-Cl)

Using the same procedure as above, **R1** (0.21 g, 0.26 mmol) was reacted with 4,4'-dichloro-2,2'-bipyridine (0.18 g, 0.78 mmol, 3 eq), and triethylamine (0.73 mL, 5.2 mmol, 17 eq). **6** was purified on a Sephadex LH-20 column using acetonitrile/isopropanol (90:10) as eluent to yield 0.16 g (52% yield). $^1$H-NMR (300 MHz; $CD_2Cl_2$): δ 8.24 (d, $J$ = 2.1 Hz, 2H), 7.88 (d, $J$ = 6.1 Hz, 2H), 7.41 (dd, $J$ = 6.2, 2.2 Hz, 2H), 7.23-7.19 (m, 6H), 6.96 (d, $J$ = 6.8 Hz, 2H), 6.56 (dd, $J$ = 6.8, 2.9 Hz, 2H), 6.44 (dd, $J$ = 6.8, 2.8 Hz, 2H), 3.48 (dq, $J$ = 15.1, 7.4 Hz, 16H), 1.23 (dt, $J$ = 12.1, 7.1 Hz, 24H). HR ESI-MS m/z (observed) 461.1641 ($M^{2+}$), m/z (calculated) 461.1633.

## 3.3 Results and Discussion

### 3.3.1 Characterization of the Ruthenium Complexes

Ruthenium complexes **1-6** seen in Figure 3.1 were synthesized in a two-step procedure to study dye adsorption to the surface of a ZnO nanocrystal, the subsequent

light absorption, and electron injection into the conduction band of the ZnO nanocrystal dispersions. These complexes with amino substituted bipyridines are of interest because the electron donating nature of the amino substituent serves multiple purposes. It destabilizes the metal based HOMO more than the ligand based LUMO, leading to a red-shift of the MLCT absorption band and a lower oxidation potential of the complex.[23, 24, 79, 80] This combination helps raise the excited state potential of the complex, which should allow for efficient electron injection into 3 nm ZnO NC dispersion. Complexes **1-5** were designed to have two amino-substituted bipyridines to raise the excited state of the complex, as well as one diacid bipyridine to anchor the complex on the surface of ZnO NCs. The control complex (**1-Cl**) was designed to have one bipyridine, particularly dichloro-bipyridine, that should not be able to coordinate to the surface of ZnO. Complex **6** makes use of the electron donating methoxy group.

The ligands **L1-L6** were prepared in good yields (50-90%) using a two step reaction starting from 4,4'-dichoro-2,2'-bipyridine-N,N'-dioxide. Using electrophilic aromatic substitution, the first reaction employed refluxing the starting bipyridine for approximately 24 hours in the neat amine. After evaporating the excess amine, the crude ligand mixture was deoxygenated using $PCl_3$ in chloroform. The desired bipyridines are then precipitated from aqueous solution with the addition of concentrated base. These reactions lead to pure 4,4'-diamino-2,2'-bipyridines without the need for expensive catalysts, complicated cross-coupling, and ring-construction reactions reported elsewhere.[79] With the exception of **L2**, all bipyridines were isolated in 75+% yields based on 4,4'-dichoro-2,2'-bipyridine-N,N'-dioxide.

The synthesis of **R1-R6** makes use of glucose and ascorbic acid as the reducing agents.[53] In general, reactions involving the synthesis of the precursor Ru-bpy$_2$-Cl$_2$ have been carried out with the commonly used procedure proposed by Sullivan and coworkers in which a solution of DMF, 2,2'-bipyridine, lithium chloride and ruthenium trichloride is refluxed for several hours.[54] This reaction relies on DMF acting as both the solvent and the reducing agent, which can result in long reaction times, which is not desirable with the reactive, electron-rich bipyridines, as it would be difficult to keep the reaction from forming the trisbipyridine complexes. Through literature it was then discovered that a method involving the use of saccharides as reducing agents could reduce reaction times while still yielding the desired product.[53] This reaction was employed to synthesize the Ru-bpy$_2$-Cl$_2$ intermediates **R1-R6**. Due to the electron donating power of the amino groups, the ruthenium complexes ended up as paramagnetic ruthenium (III), which was confirmed through ESI-MS. However, the third bipyridine can easily be attached by refluxing in an aqueous ethanol solution for 2-3 hours with triethylamine to help speed the reaction and reduce the ruthenium to the desired oxidation state. The complexes **1-6** were then isolated in pure form using column chromatography. **R5** reacting with the methylpiperazine-bipyridine could not be isolated as the dichloride as all products went straight to the tris-bipyridine complex after several attempts with different reactant ratios. In order to make the desired complex it had to be synthesized in reverse. Using the ruthenium para-cymene dimer, the diacid bipyridine was first coordinated, followed by coordination of the two **L5** ligands.[17] **5** was then isolated in pure form using column chromatography.

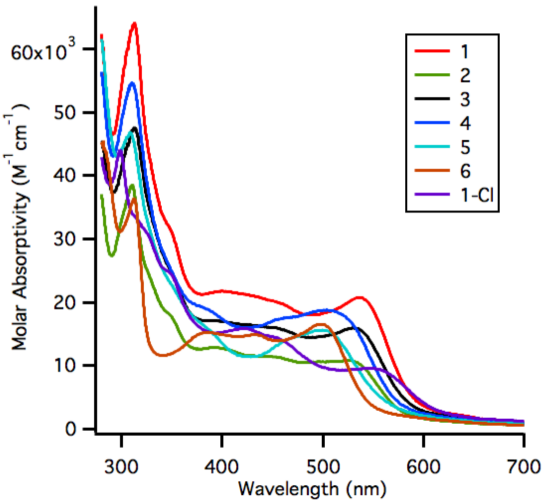


**Figure 3.2: Molar absorptivity of complexes 1-6 in methanol.**

Figure 3.2 shows the molar absorptivity of complexes **1-6** in the UV/visible region. The complexes have sharp, intense absorptions around 315 nm corresponding to the bipyridine π -π* transition. In the visible region, all complexes have a broad absorption from 400-600 nm, with the peak at 500-540 nm attributed to the metal to ligand (π*-dcbpy) transition (MLCT). The MLCT has a molar extinction coefficient of 12,000-20,000 $M^{-1}$ $cm^{-1}$, with the diethylamino substituted complex **1** having the highest molar absorptivity. The molar absorptivities of the complexes are comparable to the known dyes N3 and N719, which are 15,000 $M^{-1}$ $cm^{-1}$ at 535 nm.[10]

Figure 3.3 shows the effects of protonation state on both the visible absorption and emission trends of the complexes by examining **1**. When **1** is doubly deprotonated, the MLCT is blue-shifted by 25 nm to 515 nm in accordance with the transition requiring more energy, since the dcbpy ligand is now in its anionic form. The emission spectrum of 1 shows a very weak emission at 780 nm. When even one equivalent of $H^+$ is added,

the emission is indistinguishable from the baseline. However, the luminescence is turned on and blue-shifted to 750 when the complex is deprotonated. These complexes are only weakly emissive in their protonated states, however they become emissive upon deprotonation. The weak emission from the as-synthesized, protonated complexes of **1-6** is believed to be from an equilibrium between protonated and deprotonated forms in the methanol solution.[81] Complex specific absorption and emission data is listed in Table 3.1.

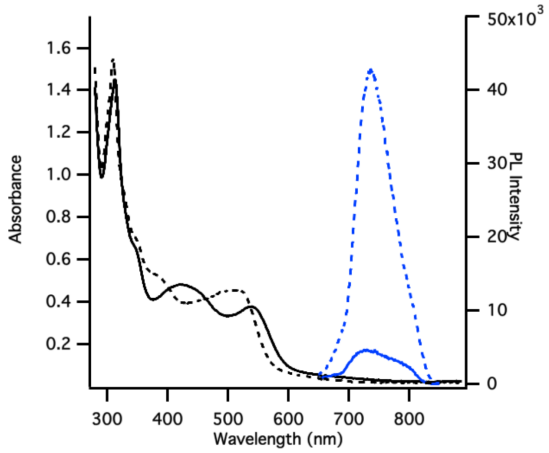


**Figure 3.3: Absorption and emission of 1 protonated (solid lines) and doubly deprotonated (dashed lines) with tetramethylammonium hydroxide in methanol. When one equivalent of additional $H^+$ is added, the emission of 1 protonated goes to zero.**

Cyclic voltammetry, shown in Figure 3.4 and listed in Table 3.1, was used to analyze the redox processes in the complexes. In their protonated forms, **1-6** show reversible $Ru^{II}/Ru^{III}$ oxidations between 0.80 - 1.37 V/NHE. It was however difficult to assign any of the reduction processes due to their irreversible nature. When deprotonated, **1-6** become easier to oxidize as the $Ru^{II}/Ru^{III}$ is shifted to lower potentials (0.78 - 1.22 V/NHE). For example, upon deprotonaton **1** becomes 0.12 V easier to oxidize than when

it is in its protonated form. Also, upon deprotonation, three reversible reductions are now evident for the three bipyridine ligands.

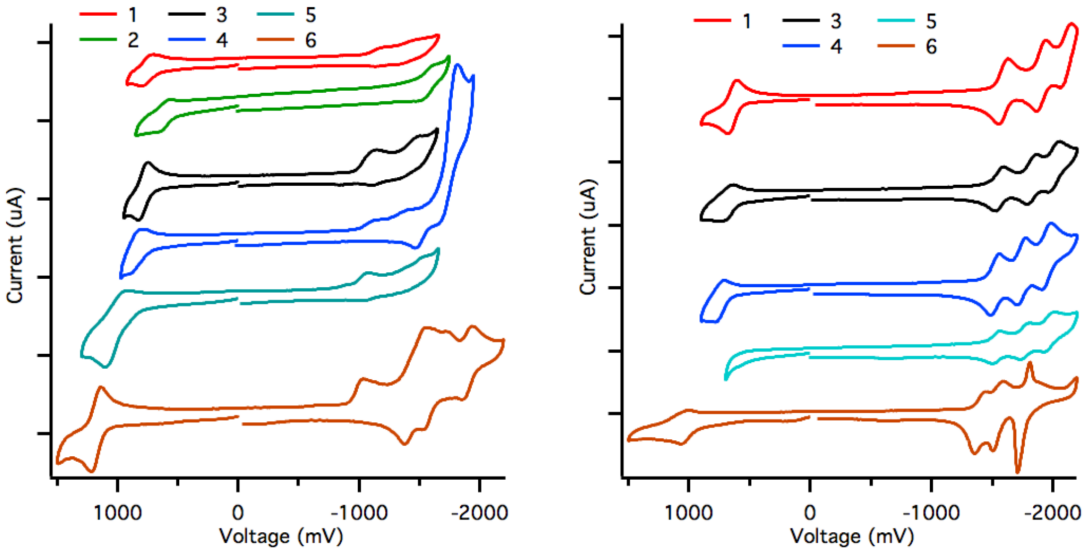


**Figure 3.4: Cyclic voltammograms of 1-6 Right Panel.) Protonated and Left Panel.) Deprotonated in dimethylformamide with 0.1 M tetrabutylammonium hexafluorophosphate as the supporting electrolyte, degassed with argon, and referenced to a Ag/AgCl electrode. Due to solubility, a CV of 2-deprotonated was not obtained. The large current at -1.7 V for 4-protonated is due to reduction of the oxygen in the morpholine ring.**

In addition to showing strong absorptions, these complexes, particularly the deprotonated forms of **1-5** are easily oxidized compared to ruthenium complexes without electron donating amines.[82] However they are still harder to oxidize compared to the corresponding homoleptic complex (reported for tris-(diethylaminobipyridine) ruthenium).[82] This is a consequence of the electron donating effects of the amino substituted ligands in combination with the electron withdrawing nature of the dicarboxylic acid bipyridine. While these complexes oxidize easily, they are stable in air

and light and do not show signs of degradation or oxidation over time in their powder form. By using the MLCT energy from visible spectroscopy and the oxidation potential from electrochemistry, the excited state oxidation potentials of the complexes, listed in Table 3.1, were calculated to be -0.82 to -1.25 V (versus NHE). The conduction band of nanocrystalline ZnO is -0.5 to -0.7 V (versus NHE) depending on the size of the nanocrystal, therefore these complexes should be sufficiently reducing to be able to inject an electron into ZnO nanocrystals when excited.

The irreversible nature of the reductions of the complexes in their protonated forms can be attributed to hydrogen gas formation from the carboxylic acid protons, which subsequently makes the reduction of the second and third bipyridine also irreversible.[33, 83] When the complexes are deprotonated first, three reversible reductions appear. In ruthenium polypyridyl complexes, the excited state is localized on the first ligand reduced electrochemically. Based on the cyclic voltammetry, the first ligand reduced is the dicarboxylic acid bipyridine based on the reversible nature of the reductions after deprotonation. Therefore, the relaxed MLCT excited state is attributed to $[RuIII(aminobpy)_2(dcb^-)]^{2+*}$, where the equilibrated excited state is localized upon the ligand that binds to ZnO.

**Table 3.1: Spectroscopic and electrochemical of complexes 1-6 and their deprotonated analogues.**

| Dyes | $\lambda_{abs}$ (nm)[a] | $\lambda_{em}$ (nm)[a,b] | $E_{1/2}$ $Ru^{III}/Ru^{II}$ (V/NHE)[c] | $E_{Red}$ $RuL_3^{2+}/RuL_3^{1+}$ (V/NHE)[d] | $E_{Red}$ $RuL_3^{1+}/RuL_3^{0}$ (V/NHE)[d] | $E_{Red}$ $RuL_3^{0}/RuL_3^{1-}$ (V/NHE)[d] | E* $Ru^{III}/Ru^{II}$ (V/NHE)[e] |
|---|---|---|---|---|---|---|---|
| **1** | 540 | 778 | 0.953 | -0.993 (ir) | -1.29 (ir) | - | -0.99 |
| **1-COO$^-$** | 515 | 748 | 0.832 | -1.40 | -1.71 | -1.92 | -1.20 |
| **2** | 535 | 760 | 0.801 | -1.43 (ir) | - | - | -1.17 |
| **2-COO$^-$** | 520 | 752 | 0.779 | - | - | - | -1.23 |
| **3** | 542 | 786 | 0.980 | -0.940 (ir) | -1.30 (ir) | - | -0.95 |
| **3-COO$^-$** | 502 | 742 | 0.865 | -1.37 | -1.64 | -1.82 | -1.21 |
| **4** | 527 | 777 | 1.04 | -0.948 (ir) | -1.21 (ir) | -1.62 (ir) | -0.94 |
| **4-COO$^-$** | 499 | 723 | 0.942 | -1.33 | -1.55 | -1.76 | -1.15 |
| **5** | 505 | 775 | 1.21 | -0.880 (ir) | -1.35 (ir) | - | -0.82 |
| **5-COO$^-$** | 498 | 725 | 0.940 | -1.34 | -1.58 | -1.78 | -1.16 |
| **6** | 500 | 740 | 1.37 | -0.840 (ir) | -1.35 (ir) | -1.75 (ir) | -0.70 |
| **6-COO$^-$** | 475 | 680 | 1.22 | -1.20 | -1.36 | -1.57 | -0.99 |
| **1-Cl** | 545 | - | 0.927 | -0.946 (ir) | -1.57 (ir) | -1.70 (ir) | |

[a] Measured in $CH_3OH$ at 25 °C. [b] $\lambda_{Excit} = \lambda_{abs}$. [c] First oxidation potential converted to NHE, recorded at 100 mV/s using tetrabutylammonium hexafluorophosphate as the supporting electrolyte in dimethylformamide. [d] Reduction potentials of the ligands. If the process is reversible the value reported is, $E_{1/2}$ ($L/L^-$). If it is irreversible, it is labeled as such (ir) and the value reported is $E_{pc}$ ($L/L^-$). Values not reported, were not observed. [e] Excited state reduction potential versus NHE.

Figure 3.5 shows the DFT (B3LYP) results obtained for **1**, which verifies the LUMO resides primarily on the dicarboxylic acid bipyridine. When the complexes are excited, the electron will reside on the dicarboxylic acid ligand bound to the surface of the ZnO, which will facilitate electron injection to the semiconductor. The calculations show that the HOMO resides on the ruthenium metal center and extends onto the amino substituted bipyridine rings and the amino nitrogen. The results for the remaining

complexes, including **1-Cl** are indistinguishable from the results obtained for **1** presented in Figure 3.5.

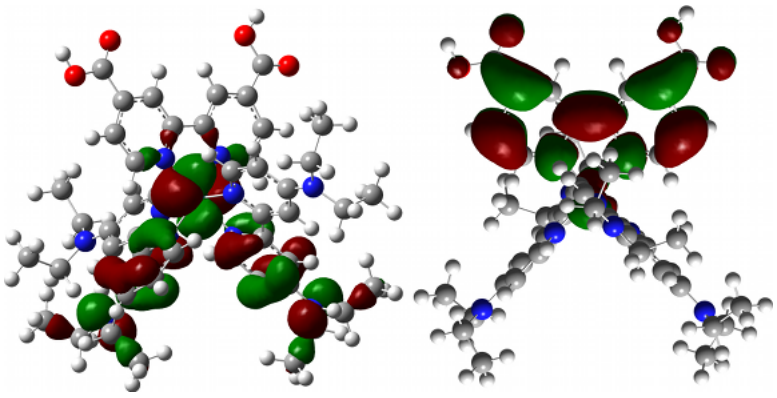

**Figure 3.5: HOMO (left) and LUMO (right) of 1 obtained from DFT B3LYP.**

### 3.3.2 Dye Binding

It is difficult to determine the binding nature of the dye to the ZnO NC. Using FTIR would be an ideal technique to monitor the binding of the dye to the surface of the ZnO NC. One would expect that as the dye binds, the C=O stretch should disappear, therefore being able to distinguish free dye from bound dye. However, the surface of ZnO is basic, plus it is possible that tetramethylammonium hydroxide is still present from the nanocrystal synthesis. Therefore it is difficult to establish qualitatively whether the dye is bound or simply has been deprotonated from the basic solution conditions. Looking at the UV/Vis of the dye alone and in the presence of ZnO, again there is a problem detecting the difference between deprotonated and surface bound. There is not much change in the spectrum with the exception of the absorbance of the ZnO around 340 nm. Results for titanium dioxide show that when the dye is bound to the surface of the nanocrystal, the UV/Vis spectrum broadens and red-shifts due to the electronic

coupling.[22] Unlike these results reported for $TiO_2$, the spectrum doesn't broaden and redshift when the dye is bound to the surface again making it difficult to determine if the dye is bound to the surface of the ZnO (and how much of it is bound) or simply deprotonated from the solution conditions.

In order to probe the question of dye bound to the surface of the ZnO, we turn to NMR, since IR and UV/Vis can't distinguish between deprotonation and dye binding. When a molecule is attached to the surface of a nanocrystal, its characteristic signals will broaden and disappear into the baseline. The broadening can be attributed to the hindered motion of the molecule on the surface[84] and the heterogenous nature of binding sites on the surface of the nanocrystal, while the disappearance of the peaks can be attributed to the slow rotation of the dye:NC complex.[85-87]

NMR experiments were used to quantify the extent of dye attachment to the surface of the nanocrystal. Figure 3.6a shows the aromatic region of the $^1$HNMR of **1** in its protonated and deprotonated forms, as well as with increasing amounts of ZnO NCs. The concentration of **1** is held constant as the concentration of ZnO is increased in successive samples. The characteristic peaks of the protonated form of **1** decrease in intensity and shift upfield to peaks characteristic of the deprotonated form of **1** with increasing ZnO concentration. The three peaks furthest downfield represent the diacid-bipyridine, with the peak at 9 ppm representing the 3 and 3' hydrogens, which are the hydrogens ortho to the acid group. These hydrogens are the most sensitive to the protonation state of the complex. As **1** is deprotonated either by the ZnO or base, these peaks shift downfield, while all other peaks associated with the diethylamino-bypyridine

are not affected significantly. At ratios of 20:1 and 10:1 free dye is still present in solution, as it is still detectable by the NMR. At 2:1, it appears all dyes in solution are attached to the surface of the ZnO as all the peaks are indistinguishable from the baseline. By keeping the concentration of dye constant while increasing the concentration of ZnO in successive samples, it is clear that the dye attaches to the nanocrystal and that the maximum surface coverage is 6 dyes per nanocrystal (~3 nm).

Using similar concentrations of dye and ZnO, as well as similar sized NCs in deuterated methanol this same experiment was done using **6** to see if there is a difference in binding between the amino derivatives and the methoxy derivative. Looking at the NMRs of **6**, free dye is still present, even in the 4:1 sample, while it is indistinguishable from the baseline at 2:1. When compared to the NMRs of **1**, the signal is almost indistinguishable from the baseline at 10:1, which indicates that the amino substituted dyes, particularly **1** are better at binding to the surface of a ZnO NC.

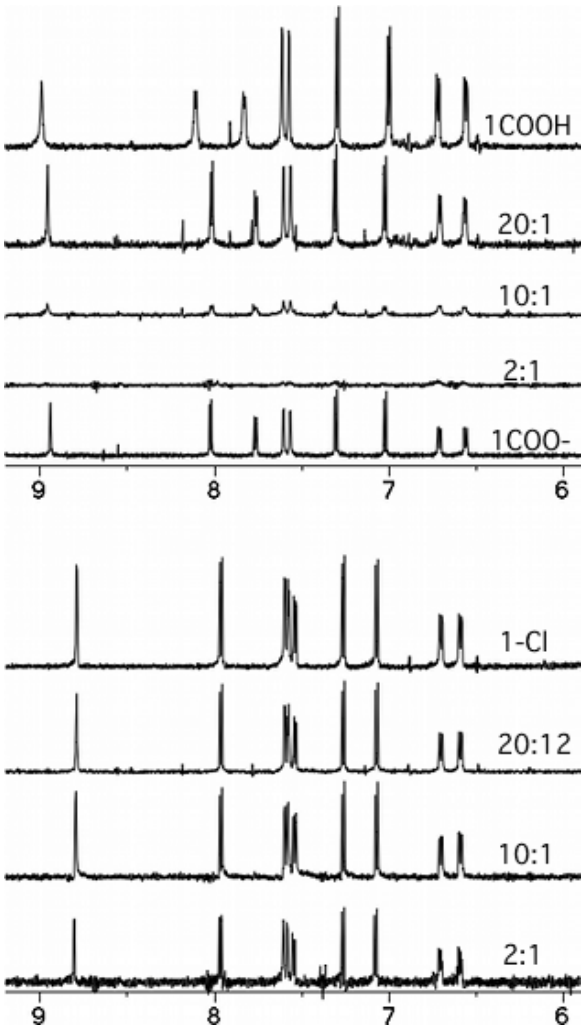


**Figure 3.6: 1HNMR spectrum of the aromatic region of 1:ZnO (top) and 1-Cl:ZnO (bottom) dyads in $CD_3OD$ at the given ratios.**

To show the difference in binding between **1** and **6**, this data is plotted in Figure 3.7, where the integrated intensity of the aromatic region of the dye alone is divided by that of the nanocrystal samples ($I^0_{NMR}/I_{NMR}$) and plotted versus the concentration of ZnO. In the case of **1** we get a linear relationship in the diminution of the aromatic peaks as a function of increasing ZnO concentration with a slope of $2.0 \times 10^4\ M^{-1}$. With **6** a linear relationship is also observed, however the slope is $4.0 \times 10^3\ M^{-1}$, indicating **1** is five times

more likely to bind to the surface than the methoxy derivative **6**. The amino substituted complexes (such as **1**) are more strongly electron donating (and thus more reactive) than the methoxy derivative **6**. This difference is one possibility that can account for the difference in binding.

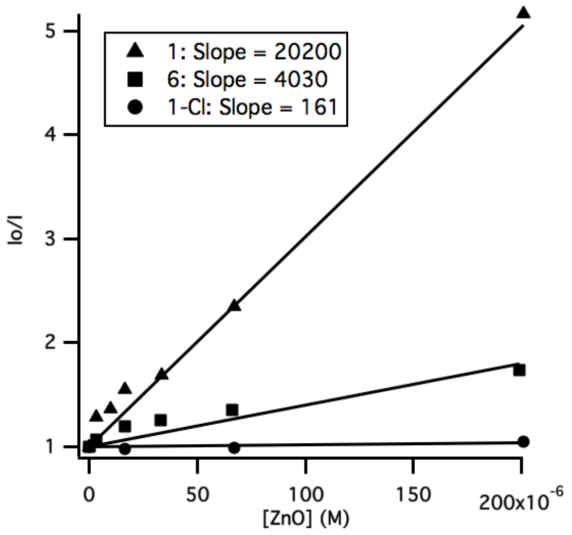


**Figure 3.7: Plot of the integrated area of the aromatic region of the dye alone divided by that of the dye:ZnO dispersions versus the concentration of ZnO NCs to show differences in dye binding to the surface of the NCs.**

To prove that the disappearance of the aromatic signals of **1** (and **6**) was a result of the dye adsorbing to the surface of the nanocrystals, the control experiment was completed using the chloro substituted complex **1-Cl**, which replaces the acid functionality with a chlorine**.** As with **1**, the concentration **1-Cl** was held constant while the concentration of the ZnO was increased with each successive sample. Looking at the spectra in Figure 3.6b of 20:1 through 2:1, there is no change in the intensity or width of the peaks. Again, when this is plotted as $I^0_{NMR}/I_{NMR}$ versus the concentration of ZnO nanocrystals in Figure 3.7, the slope is 1.6 x $10^2$ $M^{-1}$, which is over two orders of

magnitude less than **1**. This indicates that the acid functionality is necessary for binding to the surface of the nanocrystals and that NMR is a valid probe for dye binding. This proves a static quenching mechanism in that dyes must be bound to the surface of the nanocrystal to be able to inject.

### 3.3.3 Stern-Volmer Photoluminescence Quenching

Steady state Stern-Volmer quenching analysis was performed on the dyads described above using a constant concentration of dye and an increasing amount of ZnO nanocrystals and comparing the photoluminescence to that of the deprotonated dye. Figure 3.8 shows the emission of **1** at various ZnO ratios from 120:1 to 2:1. As the amount of ZnO increases, the photoluminescence intensity decreases to 50% of the dye alone due to ZnO quenching the emission of **1**. When plotted in a Stern-Volmer plot of $I_o/I$ versus concentration of ZnO in Figure 3.9, the quenching relationship is linear and the Stern-Volmer association constant ($K_{sv}$) was found to be $3.1 \times 10^4$ $M^{-1}$, which is consistent with the association constant obtained from the NMR experiment. As in the NMR experiment, the control study using **1-Cl** was done, however **1-Cl** is not emissive under any conditions and the addition of ZnO had no influence on its emission properties.

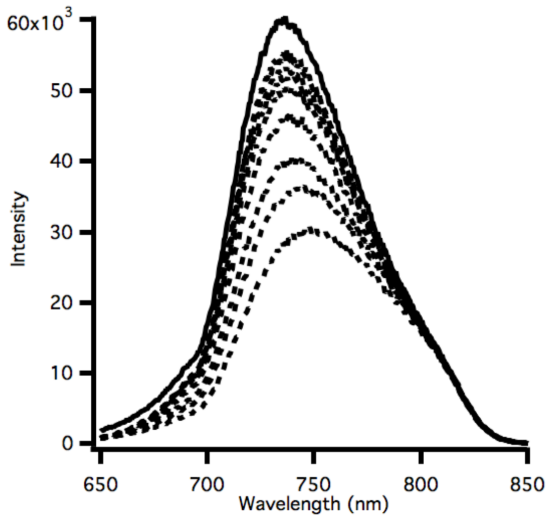


**Figure 3.8: Emission from methanol solutions of pure 1-$CO_2^-$ (solid line), (1-$CO_2^-$ )$_n$ZnO dispersions with subsequent additions of ZnO NCs at constant dye concentration. As the concentration of ZnO increases the emission intensity decreases to the final sample of 2:1. At ratios less than 2:1, the dyads precipitated. ($\lambda_{ex}$ = 415 nm).**

In the remaining complexes **2-6**, the amount of quenching is directly related to the excited state potential of the complex. While the complexes exhibit different amounts of quenching, the relationship of quenching versus concentration is linear in all cases. Table 3.2 lists the Stern-Volmer association constants for the six complexes and Figure 3.9 shows the Stern-Volmer plot for complexes **1** and **2**. As the value of $K_{sv}$ decreases, the amount of quenching decreases. Complexes **2** and **3** which have excited states similar to **1** (approximately -1.2 V), display quenching of 45-50% as in the case with **1**. However, complexes **4** and **5** have excited state potentials approximately 50 mV lower in energy than the other complexes, which leads to a maximum quenching efficiency of only 25-30%. Complex **6** has the lowest excited state value, at -1.0 V, and does not show any quenching. In fact, the Stern-Volmer constant is negative, indicating the emission

increases in the presence of ZnO. Since we know **6** is capable of attaching to the surface of the ZnO NCs, the excited state must not be of sufficient energy for electron transfer to be energetically favorable.

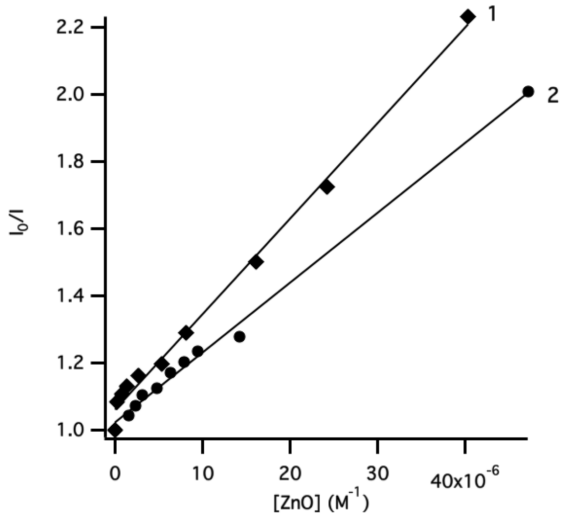


**Figure 3.9: Stern-Volmer plot of the integrated area of the emission of the dye alone divided by that of the dye:ZnO dispersions versus the concentration of ZnO NCs for 1 (diamonds) and 2 (circles).**

These results show for complexes **1-6** when attached to ZnO, that as the excited state of the dye approaches the conduction band edge of the ZnO, the injection process becomes less favorable and a lower injection yield results, until injection does not occur, in the case of **6**. This is due to the density of states of ZnO decreasing as the conduction band edge is approached, meaning that there are fewer states available for the excited electron to inject. With fewer states available, the injection yield decreases as the excited state decreases.

**Table 3.2: Stern-Volmer association constants for the corresponding dye on 3.2 nm ZnO nanocrystals in methanol.**

| Dye | **1** | **2** | **3** | **4** | **5** | **6** |
|---|---|---|---|---|---|---|
| $K_{SV}$ ($M^{-1}$) | 3.1 x $10^4$ | 2.6 x $10^4$ | 2.2 x $10^4$ | 1.7 x $10^4$ | 1.5 x $10^4$ | -3.8 x $10^3$ |

While these Stern-Volmer experiments prove that ZnO is capable of quenching the emission of the excited dye, it does not prove the mechanism. On the basis of the results discussed below, IPCE and the $TiO_2$ solar cells support electron injection as the primary mechanism, however other possible quenching mechanisms including nonradiative dissipation do exist and need to be disproved.

### 3.3.4 $TiO_2$ Solar Cells

$TiO_2$ electrodes were sensitized with dyes **1**, **3**, and **4**, as well as N3 for comparison purposes. Dyes **2**, **5**, and **6** were not reported due to solubility limitations that produced low quality films. Figure 3.10 shows the incident monochromatic photon-to-current conversion efficiency (IPCE) results over the visible spectrum. All of the dyes show high IPCE values at their respective MLCT absorptions between 450 - 550 nm, with **4** having the highest of the amino dyes synthesized. Overall, the dyes tested show comparable IPCE spectra and overall efficiencies to N3, however N3 does exhibit the highest values of any the dyes tested. The amino dyes **1** and **2** have the highest calculated excited state potentials (-1.20 V) while the excited state of **4** is 50 mV lower in energy. In addition, the absorption spectra of **1** and **2** are red-shifted by 20 nm compared to **4**, however **4** shows the highest IPCE values. Therefore, **1**and **2** are the strongest reductants and absorb the most light, but exhibit the worst efficiencies. As discussed above, the electron-donating amino groups destabilize the metal based HOMO more than the ligand

based LUMO, leading to a red-shift in the absorption spectrum. However, shifting the ruthenium HOMO too much can lead to problems with regeneration of the complex by the electrolyte after electron injection due to an insufficient driving force for the redox reaction.[5, 12] This shows the importance of the energy levels in a $TiO_2$ solar cell. Due to their strong absorptions into the red and large molar absorptivities, **1** and **2** could be promising DSSC dyes, but a more efficient and better energy match electrolyte is needed.

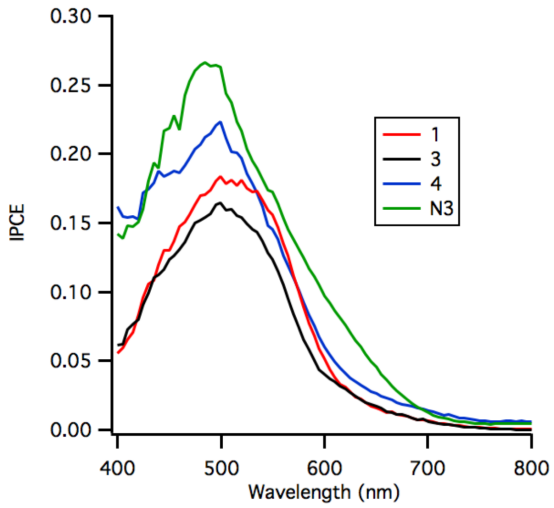


**Figure 3.10: IPCE of complexes 1, 3, 4, and N3 on $TiO_2$ electrodes.**

## 3.4 Conclusion

A series of Ru(aminobpy)$_2$(dcb) complexes (where amino = diethylamino, pyrrolidino, piperidino, morpholino, and N-methylpiperaziono) have been synthesized and characterized by NMR, MS, UV/Vis, and electrochemical techniques. Optical absorption studies show that the series absorbs into the red due to the electron donating nature of the amino substituent. The dicarboxylic acid bipyridine ligand serves as the anchoring group to bind to the surface of ZnO nanocrystals to form well-defined dyads. Steady state

photoluminescence quenching studies show that ZnO is capable of quenching the emission of the dyes. Quenching was found to be directly related to the excited state energy of the complex; **1** has the highest excited state and displays the largest quenching. However, the largest quenching efficiency does not correlate to largest incident photon-to-current conversion efficiency. The IPCE shows the importance of energy level placement of the dye in the overall DSSC device structure, as **4** showed the largest IPCE values of the amino dyes tested.

# 4 Observation of an Interface-Bound Charge-Separated Pair in Ruthenium Sensitized ZnO Nanocrystal Dispersions

Ultrafast transient absorption spectroscopy on dye:nanocrystal dyads has shown electron injection of $[Ru(deabpy)_2(dcb)](PF_6)_2$ (**1**) (deabpy = 4,4'-bis(diethylamino)-2,2'-bipyridine, dcb = 4,4'-dicarboxy-2,2'-bipyridine) into 3 nm zinc oxide (ZnO) nanocrystals dispersed in methanol. The injection was shown to proceed through an intermediate interface-bound charge-separated pair (IBCSP), before giving rise to the fully oxidized dye.

## 4.1 Introduction

In dye-sensitized solar cells (DSSC), ruthenium complexes are among the best organometallic complexes in terms of device efficiency when they are absorbed on a $TiO_2$ or ZnO mesoporous film.[3, 5] Sensitizer molecules derived from ruthenium-polypyridyl complexes have been an attractive choice due to the intense absorption bands in the visible region of the spectrum, long-lived excited states, photostability, and sensitivity to synthetic substitution to induce changes in redox and spectral properties. The ruthenium complex known as N3 has shown the largest conversion efficiencies to date (~11.2%) of ruthenium dyes, making it the standard for comparison for all new ruthenium sensitizers.[12]

Understanding the process by which photons are converted into separated charges in photovoltaic systems is important for further improvement of such technologies. In the case of DSSCs, interfacial electron transfer from the photoexcited state of the sensitizer dye to the conduction band of the metal oxide semiconductor is an important event leading to charge separation.[3, 27, 60] Charge separation between a dye linked to a semiconductor nanoparticle begins with photoexcitation of the dye. The electronic coupling between the excited molecule and states in the conduction band (CB) of the semiconductor facilitates electron transfer from the dye to CB. The dynamics of this process have been examined with a variety of time-resolved and steady-state spectroscopic methods on metal oxide nanocrystal films.[22, 60-62] Electron transfer dynamics have been investigated in such systems, with reported time constants that range from <100 femtoseconds to hundreds of picoseconds. One possible reason for the broad range

of time scales lies with the heterogeneity inherent to the films. This leads to a wide variety of different environments for both dye molecules and NCs.

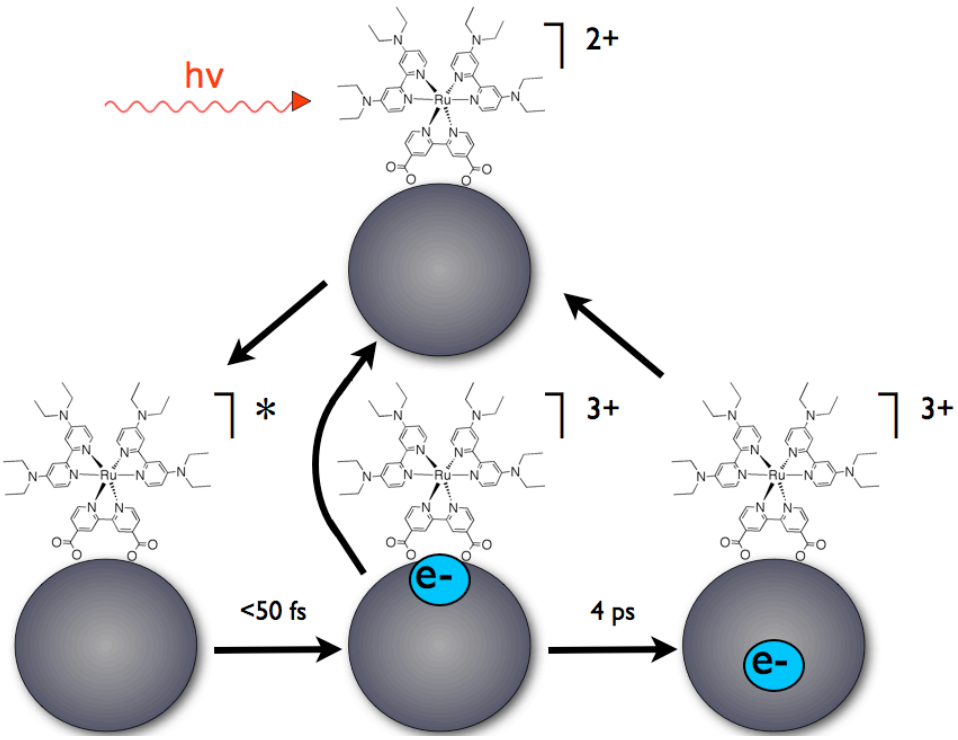


**Figure 4.1: Schematic for the interfacial charge separation and recombination proceeding through an interface-bound charge-separated pair.**

Lian and coworkers have recently done a comparison between metal oxide films of $TiO_2$, $SnO_2$, and ZnO and showed that in the case of ZnO, injection proceeds through an intermediate state, described as an interface-bound charge-separated pair (IBCSP).[62] Figure 4.1 shows a schematic of this process. Several other groups have also noticed this phenomenon in ZnO films.[66, 88-90] It is possible that when the oxide is $TiO_2$, injection proceeds through an IBCSP, but the lifetime of the species is shorter than the time resolution of the experiment. However, with ZnO the IBCSP lifetime was significantly extended with the conduction band electron lagging the initial cation formation by 12 ps.

Depending on the nature of the localized state and the coupling to the CB, the IBCSP will either separate or recombine. Noted above, the heterogeneous nanocrystal surface environment complicates electron transfer dynamics.[61, 63-69] Direct verification of the IBCSP is difficult in most systems because it either delocalizes to the CB within the time resolution of the experiment (tens of fs) or its characteristic absorption cannot be resolved from the fully oxidized dye. Complexity of the interfacial charge separation process presents significant challenges when investigating the mechanism in such heterogeneous samples.

In this regard, a homogenous sample of dye:nanocrystal dispersions can be used to simplify the system, which should allow a detailed investigation of interfacial charge transfer and more consistent comparisons between systems. This has recently been done using $TiO_2$ dispersions, but the injection did not proceed through an intermediate state.[19, 22] Zinc oxide (ZnO) offers similar properties to $TiO_2$, but has the added advantage that many synthetic routes lead to monodispersed nanocrystals which are stable as a dispersion in common solvents and are optically clear. A homogeneous sample of dye-coated ZnO NC dispersions can be used to gain a better understanding of the dynamics, which may lead to specific strategies to improve the ratio of charge separation to recombination. In this investigation we report direct evidence for IBCSP formation following photoexcitation of a ruthenium compound, (Figure 4.2), attached to ZnO nanocrystals. The IBCSP absorption is well resolved from the dye cation radical facilitating access to mechanistic and dynamic details of the interfacial charge separation.

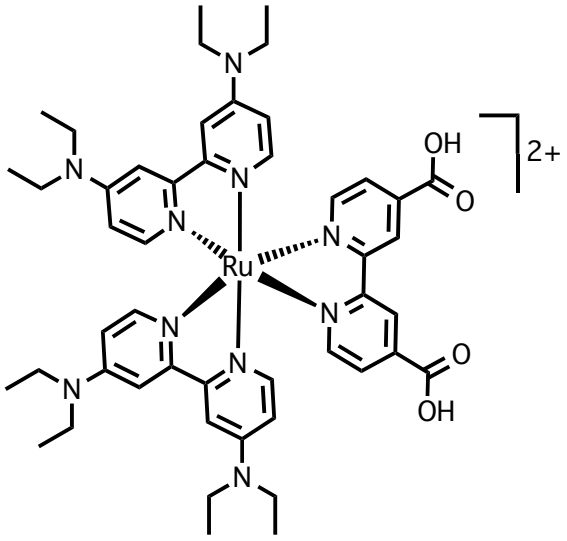


**Figure 4.2: Molecular structure of the diethylamino substituted tris-bipyridine ruthenium complex 1.**

## 4.2 Experimental

### 4.2.1 Materials

The ruthenium compound (**1**) $[Ru(deabpy)_2(dcb)](PF_6)_2$ (deabpy = 4,4'-bis(diethylamino)-2,2'-bipyridine, dcb = 4,4'-dicarboxy-2,2'-bipyridine),[51, 72, 73] was prepared as described in Chapter 3 Spectroscopic grade methanol, tetramethylammonium hydroxide ($NMe_4OH \cdot 5H_2O$), zinc acetate ($Zn\text{-}(CH_3COO)_2 \cdot 2H_2O$), dimethyl sulfoxide (DMSO), and ethyl acetate were purchased from Sigma Aldrich and used as received.

### 4.2.2 Methods

Electronic absorption spectra were collected on an Ocean Optics DH-2000-BAL spectrometer. The steady-state emission spectra were recorded on a Spex Fluorolog 1680 0.22 m double spectrometer equipped with a xenon source. Fluorescence spectra were corrected to compensate for changes in the instrument's sensitivity at longer wavelengths. UV-visible and fluorescence spectroscopic measurements were performed in quartz

cuvettes with a 3 mm path length unless otherwise noted. spectrometer. Cyclic voltammograms were obtained on a BAS-100B electrochemical analyzer using methods previously described.[52] All solutions were prepared in acetonitrile or dimethylformamide with 0.1 M tetrabutylammonium hexafluorophosphate ($TBA^+$ $PF_6^-$ ) as the supporting electrolyte and degassed with argon. Reported E° potentials were referenced to a Ag/AgCl electrode and are reported versus NHE. UV-vis spectroelectrochemical measurements were performed in a specular reflectance thin layer (0.2 mm) cell using a BAS-100B bulk electrolysis system. Solutions were prepared identically to those in the electrochemistry experiments, and spectra in the UV-vis region were recorded using an Ocean Optics USB4000 spectrometer.

### 4.2.3 Frequency Resolved Pump-Probe Measurements

Pump-probe experiments were performed using a home-built, amplified, 1 kHz Ti:sapphire laser system that produces 1 mJ, 800 nm, 80 fs (Gaussian, FWHM) pulses as described previously. The light is split and a portion was frequency doubled in a 1 mm BBO crystal for excitation at 400 nm. The resulting light was reflected off 3 dichroic mirrors to remove any residual 800 nm light, and 100 nJ/pulse was focused to a spot size of 120 μm at the sample by a 10 cm parabolic mirror. Focusing another portion of the 800 nm light into a 2 mm sapphire plate produced a probe continuum (400-900 eV). This was re-collimated, and then focused and crossed with the excitation light in the simple using the same 10 cm parabolic mirror. Polarization of the 400 eV pulse was set to the magic angle of 54.7° relative to the continuum probe to discriminate against anisotropic dynamics.

After the sample, the probe was collimated, filtered through a 1 mm cuvette consisting of 1,1'- diethyl-4,4'-dicarbocyanine iodide to remove excess 800 nm light, and focused into a Princeton Instruments 2150 monochromator that dispersed the light onto a Hamamatsu 256 pixel silicon diode array resulting in an effective resolution of 2 nm. The array was collected at the 1 kHz laser repetition rate, and the probe was modulated to 500 Hz using a mechanical chopper. The change in optical density (**Δ**O.D.) was then calculated for every sequential pair of excitation pulses a subsequently averaged over 50,000 shot pairs at each time delay between excitation and probe. All data were time corrected for temporal chirp in the probe as described previously. All samples were continuously flowed through the 1 mm optical path length quartz cuvette at a rate of 35 ml/minute. A gear pump was employed to generate the continuous flow on a closed system that was not initially degassed. Zero time delay and the instrument response function were obtained monitoring the appearance of the ground state bleach that occurs within the time response of our instrument setup.

### 4.2.4 ZnO Nanocrystal (NC) Synthesis[74]

To a 0.1 M solution of $Zn(CH_3COO)_2 \cdot 2H_2O$ (25 mL, 2.51 mmol) in DMSO, a 0.55 M solution of $NMe_4OH{\cdot}5H_2O$ (7.73 mL, 4.25 mmol) in ethanol was added dropwise over the course of 30-180 s and allowed to stir at room temperature (ca. 24 °C) for up to 30 minutes. The longer reaction times led to larger particles. The diameters were determined using electronic absorption spectra.[75] To induce precipitation, an aliquot of the solution was removed and added to three times the volume of ethyl acetate. The turbid mixture was centrifuged using a LW Scientific Ultra-8V centrifuge. After the liquid was decanted, the white pellet was dispersed in a minimum of ethanol and precipitated a

second time. The purified ZnO NCs were dispersed in methanol to yield an optically clear dispersion. To obtain a mass of ZnO, a known volume of the dispersion was evaporated and then heated to 500 °C for an hour to burn off all organics. A typical yield for the reaction is 78-80%.

### 4.2.5 Sample Preparation: Steady State Absorption, Emission and NMR

In all samples the amount of dye was held constant throughout the experiment and the amount of ZnO was varied in subsequent samples. In a typical experiment, aliquots of 3.0 x $10^{-4}$ M ZnO nanocrystals (3.0 nm in diameter) dispersed in methanol was added to 1.0 x $10^{-3}$ M dye in methanol. The samples were then diluted to a total volume of 1.2 mL with methanol. Samples were allowed to equilibrate for 2h before any measurements were taken. Methanol-$d_4$ was used for the NMR experiments.

### 4.2.6 Sample Preparation: Frequency Resolved Pump-Probe Measurements

In a typical experiment, two samples are run: protonated dye alone (40 mL of 4.0 x 10-5 M in methanol) and dye:nanocrystal (ratio is 2 dyes per 1 nanocrystal). For the dye:nanocrystal sample, 20 mL of 8.0 x 10-5 M Rudea (protonated) in methanol was added to 20 mL of 4.0 x 10-5 M ZnO nanocrystals (3.0 nm+-0.3 nm in diameter) dispersed in methanol. The sample is allowed to equilibrate for 2 hours before any measurements were taken.

## 4.3 Results and Discussion

From previous work with complexes of the form $[Ru(amino_2bpy)_2(dcb)](PF_6)_2$, where the amino substituent on the bipyridine ligands is changed, complex **1** with the diethylamino substituents was determined to be the best candidate for DSSCs. Absorption spectra for the protonated and deprotonated form of **1** in methanol samples at 6.0 x $10^{-5}$ M

are shown in Figure 4.3. The protonated complex was deprotonated by the addition of a 6.0 x $10^{-4}$ M tetramethylammonium hydroxide solution in methanol, while keeping the overall concentration of the Rudea complex constant. The protonated complex has a sharp, intense absorption at 315 nm corresponding to the bipyridine $\pi$ -$\pi^*$ transition and in the visible region, a broad absorption from 400-600 nm, with the peak at 540 nm attributed to the metal to ligand ($\pi^*$-dcbpy) transition (MLCT). The MLCT of **1** was red-shifted the most of all the complexes studied and had the highest molar extinction coefficient of 20,000 $M^{-1}$ $cm^{-1}$. Upon deprotonation, the absorption band at 540 nm on the protonated dye is blue-shifted by 25 nm. The reason for that can be explained by the lower electron affinity of the negatively charged ligand compared to the neutral counterpart, as this band corresponds to the metal-to-ligand charge transfer (MLCT) process. The molar absorptivities of **1** are comparable to those of the known dyes N3 and N719 .[10] In addition to showing strong absorptions, particularly the deprotonated form of **1** is easily oxidized compared to ruthenium complexes without electron donating amines.[82] In conjunction with absorption data, cyclic voltammetry was used to calculate the excited state potential of **1** to be -1.25 V versus NHE, which was the most reducing of the series of complexes. The conduction band of nanocrystalline ZnO is -0.5 to -0.7 V (versus NHE) depending on the size of the nanocrystal, meaning **1** should be sufficiently reducing to be able to inject an electron into ZnO nanocrystals when excited. While **1** oxidizes easily, it is stable in air and light and does not show signs of degradation or oxidation over time as a solid. For these reasons, it is not surprising that **1** exhibited the

greatest steady-state quenching ability when attached to ZnO dispersion-phase nanocrystals.

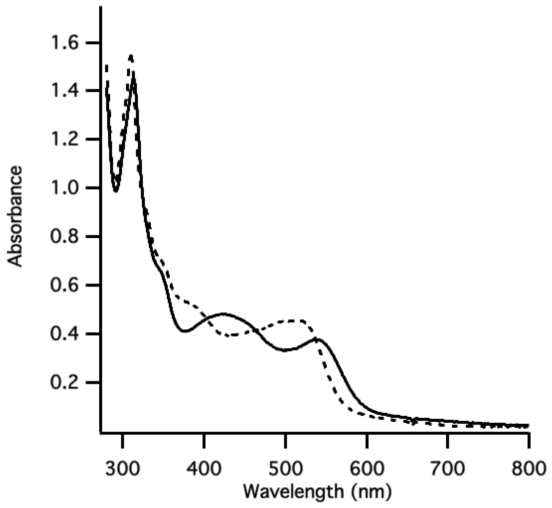


**Figure 4.3: Absorption of 1 protonated (solid lines) and doubly deprotonated (dashed lines) with tetramethylammonium hydroxide in methanol.**

While Stern-Volmer experiments prove that ZnO is capable of quenching the emission of the excited dye, it does not prove the mechanism. Possible quenching mechanisms include electron injection from the dye to the conduction band of the ZnO nanocrystal, which is the most likely mechanism, however other mechanisms do exist, including nonradiative pathways, and need to be disproved. Therefore, **1** was chosen to further study the interfacial electron transfer dynamics with ultrafast transient absorption spectroscopy.

Spectroelectrochemistry was used to obtain a spectrum of the oxidized dye **1** (cation radical) to compare to ultrafast transient absorption experiments. Figure 4.4 presents the changes observed in the UV-vis spectrum of **1** upon bulk electrolysis of the

sample at 0.7 V (a potential ~0.1 V more positive than $E_{ox}^{o}$). The bleach of the ground state absorption of the dye at 540 nm is correlated with a growth of the cation, which shows a peak at 650 nm and a broad positive absorption into the infrared. An isosbestic point is formed at 600 nm indicating clean conversion to the oxidized species. Holding the potential at -0.1 V regenerates the original spectrum, indicating the reversibility of the process. The difference between the first data set (neutral dye) and the last data set (fully oxidized dye), occur through a clean isosbestic point at 600 nm. The inset in Figure 4.4 shows that a decay from the band at 540 nm is accompanied by a rise of a band with a peak at 650 nm.

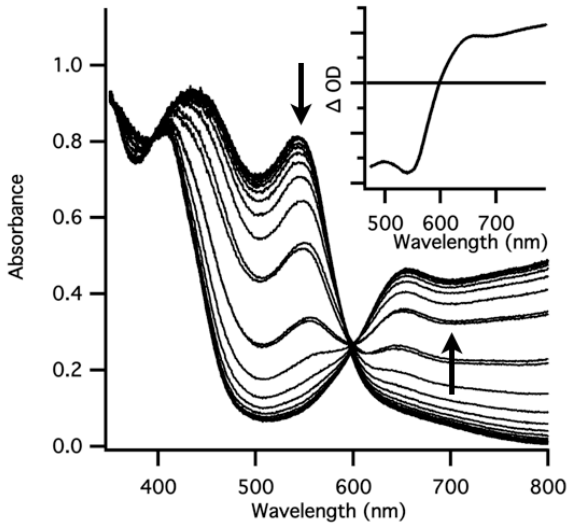


**Figure 4.4: Absorption spectrum of the cation radical of 1 obtained through bulk electrolysis of the reversible oxidation process. Inset: Difference spectrum.**

Ultrafast transient absorption spectroscopy was used to study samples of **1**:nanocrystal dyads in methanol, which were photoexcited at 400 nm. In order to

understand the interfacial electron transfer of the dyads, it is necessary to understand the excited state dynamics of **1** in methanol without the presence of ZnO.

Figure 4.5a shows the dye alone sample **1** in its protonated form. Looking at the dye alone spectrum, there is a bleach of the ground state at 525 nm and a broad positive absorption from 600 to 800 nm attributed to the excited state absorbance of the dye. The appearance of the excited state absorption is instrument limited (appears in first 80 fs) and persists for the length of the experiment (500 ps). It has been reported in recent literature that the intersystem crossing from the singlet to triplet state in ruthenium-polypyridyl complexes occurs on the time scale of 50 fs.[91, 92] Therefore, the excited state absorbance can be attributed to the excited triplet state absorbance, while the singlet to triplet conversion takes place within the pulse width of the instrument. The long lived excited state can be fit to a monoexponetial decay with a lifetime of 5 nanoseconds at 688 nm. The bleach recovery at 525 nm can also be fit with a monoexponential rise with a lifetime of 5 ns. Table 4.1 lists all the lifetimes at the wavelengths of interest. With data taken only to a long time point of 500 ps, it is difficult to get an accurate fit for this lifetime. However, it is known that the excited state lifetime is on the order of 10-100 ns in these complexes, therefore it should not affect the charge transfer event.[93] The transient absorption spectrum of the doubly deprotonated form of **1** (not shown) is the same as that of the protonated form, with the one exception being the bleach occurs at 515 nm, a blue-shift of 25 nm. This agrees with the UV/Vis differences in MLCT absorption between protonated and deprotonated **1**.

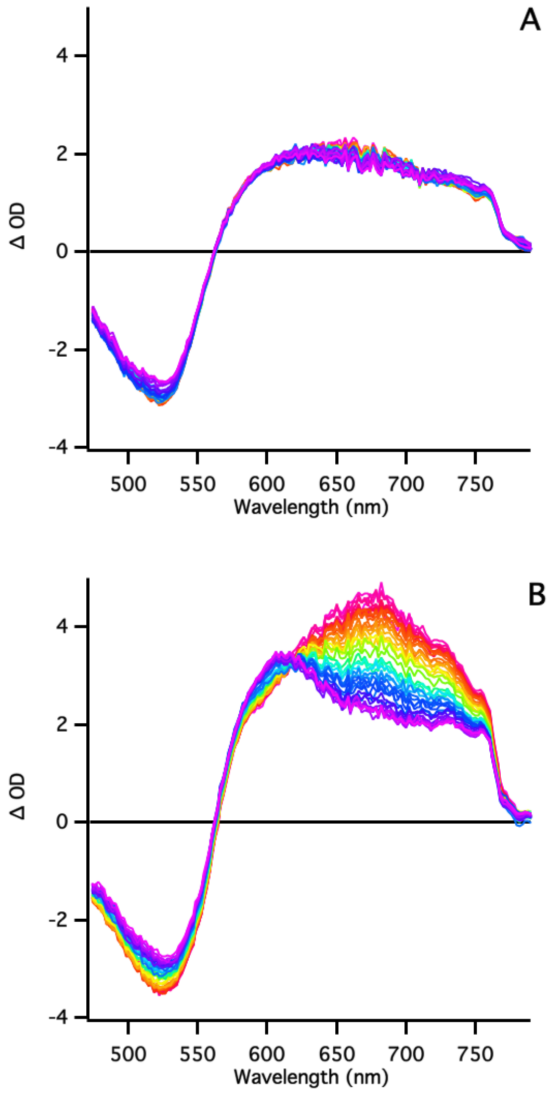


**Figure 4.5: Full frequency transient absorption spectra from 0 fs (red) to 500 ps (purple) of A.) 1-dye alone and B.) 2:1 dye:ZnO in methanol.**

Ultrafast measurements were used to study samples of **1**:nanocrystal dyads in methanol at a ratio of 2:1**,** which were photoexcited at 400 nm. At this wavelength, ZnO NCs do not absorb allowing selective excitation of the dye. Figure 4.5b shows the transient absorption of the 2 dye to 1 nanocrystal (2:1) sample. This ratio was chosen

because it showed no significant amount of free dye in solution according to NMR as well as the largest photoluminescence quench. In this sample, the same bleach at 525 nm is present, however a new feature appears at 688 nm, which decays to a second feature at 600 nm with an isosbestic point at 620 nm. The new feature at 688 nm is instrument limited and shows up within the first 80 fs. This feature can be fit to a biexponential decay with lifetimes of 3 ps and 3 ns (Table 4.1). As the feature at 688 nm decays, the second feature at 600 nm grows in, which can be fit to a biexponential with lifetimes of 4 ps rise followed by a 4 ns decay. This feature at 600 nm can be assigned as the cation radical of **1** based on the spectroelectrochemisty. The isosbestic point could not be fit to either an exponential rise or decay. Finally, the bleach at 525 nm can be fit to a biexponential rise with lifetimes of 3 ps and 5 ns.

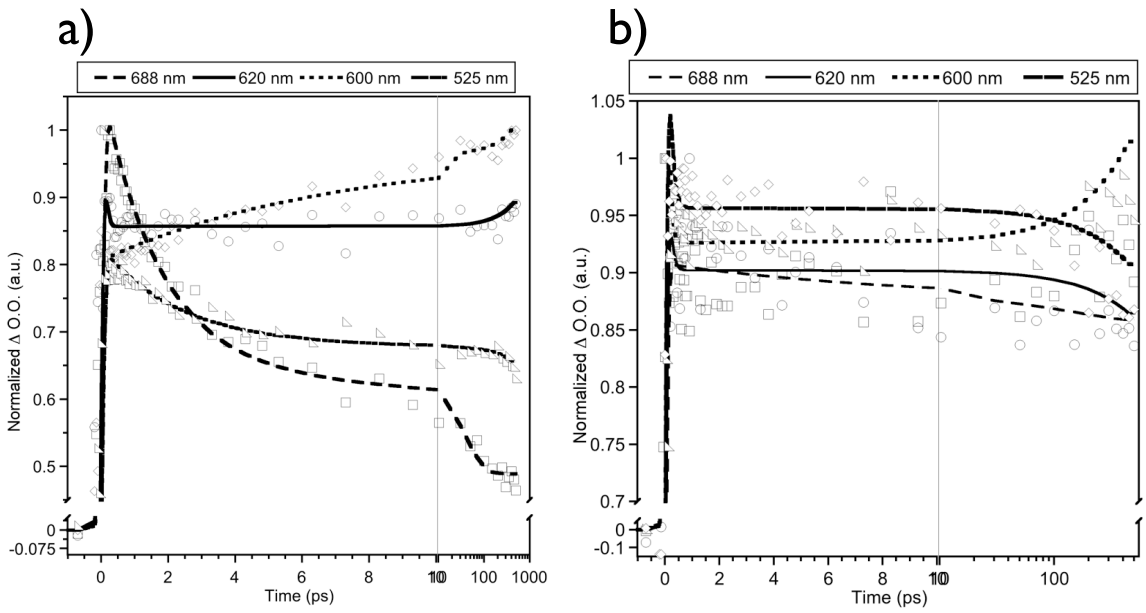


**Figure 4.6: Transient absorption spectra at 525, 600, 620, and 688 nm for a) 1:ZnO dyads at a ratio of 2:1 and b) 1 dye alone. Points are raw data and fits are represented by lines. Fit parameters are given in Table 4.1.**

Looking at the spectrum of the 2:1 dye to nanocrystal (surface unsaturated), two spectral features are evident. The first feature at 688 nm appears within the pulse width of the instrument and decays with a lifetime of 3 ps into the second feature at 600 nm. When we fit the rise of the spectral feature at 600 nm, we get a 4 ps component. The consistency of the lifetimes of the decay at 688 nm with the rise at 600 nm, in addition to the isosbestic point at 620 nm, indicates that the initial spectrum gives rise to the final spectrum. We can conclude that the excited dye forms an interface-bound charge-separated pair (IBCSP)[62] in which it injects an electron onto the surface or into a trap state of the ZnO nanocrystal, giving the spectral feature at 688 nm faster than 80 fs. A schematic of this process is shown in Figure 4.1. This process has been studied on ZnO films,[62, 88, 89] but has not been seen in disperse nanocrystals. The IBCSP spectrum resembles the spectrum of the oxidized dye, only at lower energy than the free cation is expected. Once the IBCSP is formed it can decay through one of two pathways: into a conduction band electron and the oxidized dye or it can recombine to regenerate the ground state. Figure 4.5 shows that the IBCSP decays into the cation radical of **1** at 600 nm. The cation of **1** is a higher energy species than the IBCSP, which is consistent with previous results on these types of intermediates.[62, 66, 88-90] This peak is blue-shifted 20 nm from that of the cation (seen in the spectroelectrochemistry in Figure 4.4), but we can assign it as such due to the different environment on the surface of the nanocrystal and the change in solvent. [19, 20, 22] The IBCSP feature is an ultrafast event as it appears within the pulse-width of the instrument and shows a lifetime of 4 ps. With the appearance of the cation radical of **1** on the time scale observed it is apparent that the dye is capable of

injecting from the excited singlet or the thermally excited triplet state, which means the process is an ultrafast electron injection into ZnO.[91]

**Table 4.1: Summary of fits to Ultrafast Measurements of 1:ZnO Dyads.**

| Dye Species (probe nm) | tau1 (ps) | a1 | tau2 (ps) | a2 |
|---|---|---|---|---|
| Dye (525) | 5000 (rise) | | | |
| Dye (600) | flat | | | |
| Dye (620) | flat | | | |
| Dye (688) | 5000 | | | |
| 2:1 (525) | 3.0 (rise) | 0.1 | 5000 | 0.7 |
| 2:1 (600) | 4.0 (rise) | | 4000 | |
| 2:1 (620) | flat | | | |
| 2:1 (688) | 3.0 | 0.45 | 3100 | 0.56 |

We can further confirm that the spectral feature at 600 nm is in fact the cation radical by fitting the bleach recovery at 525 nm. In the dye alone spectrum, the bleach recovery has the same long lifetime as the decay of the excited state. However, in the 2:1 sample the bleach has a 3 ps rise, which proves the second pathway available to the IBCSP in which the electron recombines with the oxidized dye regenerating the ground state. This indicates that the IBCSP is initially formed, where some of the dye decay into the fully charge separated species (cation radical) and an electron, while others recombine to form the ground state. The fact that some dyes inject and other recombine accounts for the reduction in the amplitude of the cation radical compared to the initial IBCSP peak as well as the bleach recovery in the 2:1 sample seen in Figure 4b. It also

confirms the steady-state quenching experiments, in which we see a 50% reduction in the photoluminescence of **1** when attached to ZnO NCs due to some dyes injecting and others recombining with the ground state. Therefore, we have an ultrafast electron injection from **1** into ZnO dispersion phase nanocrystals initially forming an interface-bound charge-separated pair, which then decays into the conduction band giving the second unique spectral feature, which is associated with the cation of **1**.

Unfortunately, this process is not reproducible. Approximately 50 experiments on **1**:ZnO dyads have shown the IBCSP feature 10% of the time. Five separate experiments, with different versions of dye have shown the distinct features, while countless experiments show the dyad spectra resembling that of the dye alone. It is still unclear why this is the case. Both ZnO and the dye are pH sensitive, so it is possible that this is complicating the process. However, the pH has been adjusted for the dye, the nanocrystals, and the dyads, but has not successfully reproduced the results. Work is in progress to further study this system and the IBCSP.

## 4.4 Conclusion

Femtosecond transient absorption spectroscopy has been carried out to study the interfacial electron transfer dynamics of **1**:ZnO which is compared to the dye alone. When excited at 400 nm, the transient absorption of an interface-bound charge-separated pair forms within the pulse width and decays into the fully charge separated cation radical of the dye over 4 ps. The spectral position and shape of the cation spectrum was confirmed through a separate spectroelectochemisty experiment.

# 5 Multi-Spectral Nanocrystal Light-Emitting Diodes

Semiconductor nanocrystals (NC) have attracted considerable interest recently because their physical properties are size dependent and differ from the bulk. A potential application of this work involves displays, as there is a need for cheap, efficient, multicolor light emitters. This research explores the synthesis and characterization of direct band gap III-V semiconductor nanocrystals for use in LED devices; specifically InP, InAs, and $InAs_xP_{1-x}$. Work focuses on synthesizing air-stable, monodisperse, highly photoluminescent InP nanocrystals, which emit from visible to infrared wavelengths. A wide range of particle sizes can be produced with narrow size distributions by changing the growth time or concentration of the capping agent. To date, NCs have been produced from 1-4 nm, which display UV/Vis absorption peaks between 350 and 600 nm. A successive ion layer adsorption and reaction (SILAR) technique is used to deposit a shell to stabilize the core against oxidation and increase the photoluminescence. The stability and emission are assessed using UV-Vis and fluorescence spectroscopy.

## 5.1 Introduction

As new applications related to optical devices have been developed over the past several decades, nano-materials research has emerged as a dominant field. This is part of a larger trend in science towards the creation and utilization of materials and devices through the control of matter on the nano-scale. In recent years, nanocrystals (NC) have become an attractive class of materials for many applications. Semiconductor nanocrystals possess optical and electronic properties similar to molecules; yet, these properties can be modified by controlling bulk material parameters such as size and crystallinity. The photoluminescence of many semiconductor nanocrystals can be tuned across the visible spectrum and into the infrared (IR) by changing their size.[94] These properties, in addition to their resistance to photo-bleaching, make them lucrative for applications such as bio-medical labels, solar cells, and hybrid light-emitting diodes (LEDs).[95-97]

Currently there is interest in displays, solid-state lighting, and optical sensors, where there is a need for cheap, efficient, multicolor light emitters. Presently, organic light-emitting diodes (OLEDs) are promising due to low cost, low temperature processing on a variety of large, yet flexible substrates. Although OLEDs are capable of red and green emission, they are unable to span the entire visible spectrum and into the infrared, making them unfit for high performance displays.[98] Also, OLED lifetime is a problem, especially at high brightness and shorter wavelengths due to exciton quenching.[99] Recent research involving II-VI semiconductor nanoparticle devices suggests that this decrease in efficiency from quenching is negligible in these systems.[100] For this reason, direct

bandgap semiconductor nanocrystals are being explored for LED devices and display applications.

### 5.1.1 Synthesis

There are a number of methods for synthesizing nanocrystals. The two main synthetic approaches used today are plasma and solution based. Synthesis of nanocrystals using nonthermal plasmas has become a viable option even for materials that require high temperatures.[101, 102] In a typical plasma synthesis, the size of the resulting nanocrystals is controlled by the residence time of the gas in the plasma region. The size distribution in this system is often quite broad (20%) compared to standard solution techniques. However, an advantage of plasma synthesis as compared to liquid phase routes is that the resulting material is free of ligands or surfactants, and that the ligands can be added later depending on the targeted application. This makes integration of plasma-produced NCs into devices easier, as it eliminates intermediate steps of ligand exchanges often required for II-VI and IV-VI NCs. Solution based techniques include reduction reactions, kinetically-confined micelle synthesis, and hot injection. However, reduction and micelle-based processes generally do not produce monodisperse nanocrystals. Hot injection reactions produce monodisperse, high quality nanocrystals, which can be used for most applications.

Given that many properties of nanocrystals are size dependent, polydispersity creates a wide range of properties within a sample. Their optical spectra show broadened peaks, implying emission over several wavelengths. Polydisperse samples are therefore undesirable for any type of nanocrystal device application. Monodisperse samples are produced by separating the nucleation of the nanocrystals from their subsequent growth.

The hot injection reaction reported by Murray, *et al.* accomplishes this through the rapid injection of a precursor solution into a hot solution of surfactants.[103] The reaction proceeds according to different precursor concentration phases (Figure 5.1).[104] On injection, the precursor concentrations are quickly forced above the nucleation threshold. The solution begins nucleating nanocrystals until the precursor concentration decreases below the nucleation concentration. Nanocrystal growth is the direct result of decreasing precursor concentrations once below the nucleation concentration. By making growth time substantially longer than nucleation times, nucleation will be independent of growth. Particles that nucleate at the same time will grow at the same rate for the same amount of time, leading to a monodisperse size distribution. Hot injection reactions typically produce nanocrystals with a standard deviation in size of 10% or less.

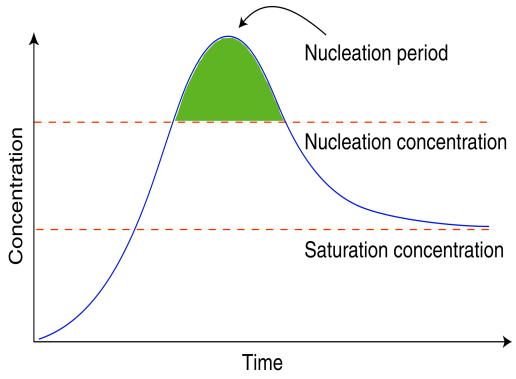


**Figure 5.1: Graph of nanocrystal nucleation and growth stages in hot injection syntheses**

High temperature routes have the benefit of producing crystalline samples that contain minimal trap states. At elevated temperatures, it is thermodynamically favorable for the atoms to diffuse within the forming crystal and react at a favorable location. Because the atoms do not have to react at the first location they come in contact with,

defect sites within the crystal are minimized as they are given a chance to react. In the low temperature syntheses this is not thermodynamically favorable, so the resulting nanocrystals often exhibit poor crystallinity.

### 5.1.2 Surface Passivation

Nanocrystal defects often form trap-states that often occur in the band gap. This would be similar to a non-bonding orbital according to molecular orbital theory. These trap states are a result of imperfections in the crystal and lead to a disruption in the flow of charge carriers through the semiconductor. This disrupted flow eventually leads to quenching of the charge carriers through nonradiative recombination.[105] Surface trap states (dangling bonds) are also possible due to an imperfect crystal structure at the surface. Both crystal defects and surface traps produce similar effects; however, the surface traps can be passivated by ligands bound to the surface. When the ligands bind to the surface, the trap state that was present reacts forming bonding and anti-bonding orbitals in the valence and conduction bands of the nanocrystal, respectively. [106]

Due to the bulky ligands typically used, not every surface atom is bound to a ligand. Also, it is generally difficult to passivate both anionic and cationic surface sites with the same ligand (or solvent). Therefore, this leaves surface sites open, meaning incomplete passivation of dangling bonds. Passivation of surface trap states can also be accomplished through creating core/shell structures. By choosing a shell such that the band gap energy is larger than the core, the shell can passivate the trap states without affecting the energetics of the core.[107] With this structure, the charge carriers will have sufficient energy to enter the conduction band of the core, but insufficient to enter the conduction band of the shell. Therefore, the overall quantum confinement in the core is

maintained. Elimination of trap states effectively increases the ratio of radiative to nonradiative recombination, thus increasing the photoluminescence quantum efficiency.[108]

Certain systems require a core/shell morphology. Currently, there are three synthetic techniques to grow a semiconductor shell on a nanocrystal. By adding shell precursors in precise amounts so that their concentration does not pass the nucleation threshold, the shell will grow on the existing core nanocrystals.[108] Also, the successive ion layer adsorption and reaction (SILAR) method deposits a monolayer at a time of the shell on to the core nanocrystals, similar to atomic layer deposition (ALD), and gives excellent thickness control.[109] This technique has the advantage of not nucleating shell particles, since only one precursor is introduced at a time and can be done in the same reaction vessel as the growth. Finally, a one-pot reaction method can be used. By choosing the reactivity of core precursors to be greater than shell precursors, the nanocrystal core will form first. As the reaction proceeds, the core will be overgrown by the shell over time.[110] However, this technique is harder to control and does not produce the well-defined core/shell structures typical of a SILAR synthesis.

Surface ligands are a particularly important variable of solution-based syntheses. They are important because they can be used to control solubility, surface chemistry, and spacing of the nanocrystals in solution and on devices. The ligands provide steric stabilization, which relies on long hydrocarbon chains to prevent particle aggregation.[111] Ligands can also provide Coulombic stabilization, which relies of charge repulsion to stabilize the nanocrystals. Ultimately, the surface ligands provide the ability to form

stable dispersions that are necessary for long-term study and nanocrystal processing. Without this stabilization, continued growth by Ostwald ripening forms larger particles and eliminates the uniform size distribution. This is undesirable and changes the properties of the sample.

Of the synthetic methods stated, solution-based, hot injection syntheses offer the most efficient way to produce semiconductor nanocrystals. The resulting NCs are crystalline, monodisperse, and easily stabilized by the addition of surface ligands. The quality of the nanocrystals plays an important role in the properties of the sample.

### 5.1.3 Nanocrystal Devices

The wide variety of nanocrystal surface chemistries enables processing in many different solvents and polymers. Therefore, hybrid organic/nanocrystal devices have the potential to combine the facile processing of OLED devices with the alluring optical properties of nanocrystals. A major advantage of III-V semiconductors is the robust covalent bond compared to the ionic bond present in II-VI semiconductors.[112] Also, III-V nanocrystals offer an ideal emission range from red to infrared. However, due to surface traps, stacking faults, and high de-trapping activation energy in the crystal compared to II-VI semiconductors, III-V semiconductors usually have a decreased quantum yield.[113] Other existing problems include poor control of size distribution and poor size tunability. Additionally, III-V syntheses are more complicated than the well-established II-VI semiconductor cadmium selenide (CdSe).[103]

The goal of this research is the development of a solution-based synthesis of monodisperse, single crystal indium phosphide (InP), indium arsenide (InAs), and indium arsenide phosphide ($InAs_xP_{1-x}$) nanocrystals that have efficient, tunable emissions.

Ideally, the nanocrystals will have emissions from 1.3-1.55 μm, which represents the prime telecommunication wavelength region. An efficient procedure to passivate the surface of the nanocrystal will also need to be developed to provide the stability of the nanocrystal and maximize the quantum yield. Using these nanocrystals, light-emitting diodes will be fabricated to span from the optical to infrared region.

Currently, II-VI nanocrystal based systems, especially cadmium selenide, dominate the literature. Colvin et al. reported the first hybrid nanocrystal/polymer LED.[114] On an indium tin oxide (ITO) anode, a bilayer device structure was fabricated. It consisted of a polymer layer of poly(para-phenylenevinylene) (PPV) as the hole-transporting layer (HTL), followed by deposition of a thin layer of CdSe nanocrystals deposited on a conducting polymer. A magnesium/silver cathode was then deposited on top of the nanocrystal layer. The device architecture allows electron injection into the nanocrystal layer and hole injection into the PPV layer. By changing the size of the CdSe used in the device, the electroluminescence (EL) could be tuned from yellow to red. They hypothesized the recombination zone lay within the nanocrystal layer, close to the PPV interface because at higher voltages, PPV emission was predominant.

In an attempt to eliminate emissions from the transport layers, a subsequent group reported a single layer device. In this device, CdSe nanocrystals were homogeneously distributed in a polymer layer that contained both the electron and hole transport species.[115] In order to prevent charge transport between nanocrystals, a volume fraction of 5-10% CdSe was used. By preventing transport between nanocrystals, efficient exciton recombination will occur. Again, a narrow electroluminescence was obtained and could

be tuned by varying the size of the nanocrystals. With this design, the electroluminescence emission wavelength remained constant under forward and reverse bias, indicating the CdSe was not directly involved in charge transport. This showed that electron and hole injection through tunneling was the excitation mechanism for the nanocrystals.

These first two devices exhibited very low (below 0.001%) external quantum efficiencies (EQE); however, they showed that it was possible to obtain a narrow electroluminescence emission from semiconductor nanocrystals. Also, this research demonstrated the ability to tune the electroluminescence through nanocrystal size, rather than by changing the composition of the material used, which is the case for organic based devices. With this knowledge, the same groups reported similar bilayer devices using CdSe/CdS core/shell nanocrystals.[116,117] The core/shell based devices showed an increase in the external quantum efficiency of a factor of 20 and the lifetime by a factor of 100. However, considerable PPV emission was still present due to the fact that recombination can still occur in the hole transport layer.

In order to isolate the luminescent function of the nanocrystals from their participation in electron transport, a trilayer device was developed by Coe-Sullivan, et al. using CdSe/ZnS core/shell nanocrystals.[100, 118] In this device architecture, the nanocrystals are deposited in between corresponding electron and hole transport layers. N, N'-diphenyl-N, N'-bis(3methylphenyl)-(1,1'-biphenyl)-4, 4'diamine (TPD) is the HTL and tris-(8-hydroxyquinoline) aluminum ($Alq_3$) the electron transport layer (ETL). This structure relies on the self-segregation of the nanocrystals from the aromatic

molecules of the hole-transport layer to produce a single monolayer of CdSe/ZnS at the interface. In order to produce a single monolayer, a monodisperse sample is needed so the nanocrystals can close pack. A separate electron transport layer (ETL) was then deposited on top of the nanocrystal layer.

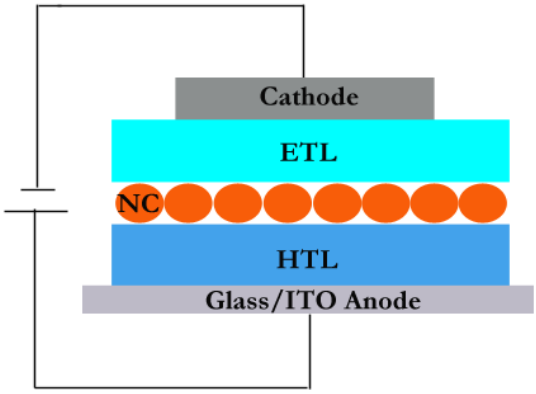


**Figure 5.2: Device architecture and electroluminescence spectra of trilayer LEDs.**[118]

With this structure, charge carriers are transported to the nanocrystal interface where recombination can occur producing a narrow electroluminescence (Figure 5.2). In order to block the holes and confine the excitons, a layer of 3-(4-biphenyl)-4-phenyl-5-tert-butylphenyl-1,2,4-triazole (TAZ) was deposited in between the nanocrystal layer and the ETL. The TAZ produced a narrower emission band with fewer contributions from the polymer layers. The trilayer device was able to nullify electroluminescence of the transport layers by eliminating the dual function of the nanocrystals and produced an external quantum efficiency of 0.5%.

Additional studies of the trilayer device have explored nanocrystal size and shell thickness as a function of device efficiency.[118] For CdSe/ZnS based devices, increasing

the core diameter increases the absorption cross-section. However, it is difficult to maintain a narrow size distribution with larger diameter cores, making device fabrication difficult. Increasing the thickness of the ZnS shell from 0.7 to 2.5 monolayers increased the external quantum efficiency to 1.1%, but the total nanocrystal diameter increased, making monodispersity harder to maintain with each subsequent layer. As each additional layer is deposited, there is a greater chance that the layers become non-uniform, leading to a range of nanocrystal sizes. Therefore, CdSe nanocrystal sizes in the middle of the tunable range with one ZnS monolayer led to the best devices, because they offer the most monodisperse samples.

With these considerations, the trilayer device architecture, seen in Figure 5.2, is the best candidate for producing the highest external quantum efficiency. These devices work best with single monolayer core/shell nanocrystals, since they are able to maintain narrow size distributions. Table 5.1 summarizes the results of LED device architectures and efficiencies. With this knowledge, device architecture can be applied to III-V semiconductor based LEDs and optimized for infrared emission.

**Table 5.1: Summary of LED architectures and EQE.**

| LED Architecture | External Efficiency | Nanocrystal, Emitting Wavelength |
|---|---|---|
| Blended single layer of NCs and polymers | 0.0005% | CdSe, 530-650 nm |
| Bi-layer devices of separated thin films of NCs and organics | 0.22%, 0.8% | CdSe/CdS, CdSe/ZnS, 530-650 nm |
| Tri-layer devices with NC monolayer between organic layers | 0.2 - 1.1% | CdSe/ZnS, 530-650 nm |

### 5.1.4 Degradation Mechanisms

In nanocrystal LEDs, there are several mechanisms by which the device can lose efficiency and degrade over time. Monodisperse nanocrystals are essential, not only for their unique properties, but to form a uniform monolayer in the device.[118] By altering the synthetic procedure, monodisperse samples can be made. Photoluminescence (PL) of the nanocrystal sample is also important to device efficiency. Greater quantum yields, in which absorbed light is re-emitted, produce brighter devices. A chemical etching process [113] or a core shell structure [108-110] can be used to increase the emission efficiency. However nanocrystals often exhibit photoluminescence intermittency, also known as blinking. The photoluminescence efficiency of a single nanocrystal continuously modulates between on and off states, and there is a non-uniform dark period.[119] The current consensus is that nanocrystals can become charged, leading to the photoluminescence quench.[120] In a neutral nanocrystal, an electron in the conduction band recombines with a hole in the valence band, emitting a photon.[121] Through appropriate surface treatment techniques, photoluminescence quantum yields can be improved in addition to reducing blinking. [122, 123] Also, careful choice of electrodes can stabilize the device architecture. [124, 125, 126] With these considerations, stable devices can be fabricated.

## 5.2 Experimental

### 5.2.1 Materials

Trioctylphosphine oxide (TOPO) and trioctylphosphine, tris(trimethylsilyl)phosphine, myristic acid, 1-octadecene, dodecylphosphonic acid, hexadecylamine were purchased from Sigma Aldrich and used as received. Indium

chloride, indium trifluoroacetate, zinc stearate, gallium acetylacetonate, and trimethylgallium were purchased from Strem Chemicals and used as received. All syntheses were carried out using standard air-free techniques. For a hot-injection synthesis, the organometallic precursors were injected into a hot surfactant solution in a non-coordinating solvent, which had been degassed prior to injection. The nanocrystals were grown at temperatures between 200-300°C and aliquots monitored through optical spectroscopy (UV/Vis). When the desired size was obtained, the reaction was stopped and cooled to room temperature. The resulting nanocrystals were purified through repeated extractions using a non-miscible polar solvent, precipitated with a miscible polar solvent, and redispersed in a non-polar solvent.

### 5.2.2 Methods

UV/Vis spectra were obtained on an Ocean Optics DH-2000-BAL spectrometer using a quartz cuvette with a path-length of 1.00 cm. Spectra were taken with an integration time of 6 seconds and a minimum of 128 spectra were averaged. Photoluminescence excitation and emission spectra were taken on a Cary Eclipse Fluorescence spectrometer using an excitation wavelength of 375 nm**.** X-ray patterns were obtained on a Bruker-AXS Microdiffractometer using $2\theta = 40$, $\Omega = 20$ for 3 minutes. Samples were drop-cast from toluene on glass slides. Peak fitting and background subtraction of the resulting x-ray patterns was done using MDI JADE 7. Transmission electron micrographs were taken on a FEI Tecnai T12 microscope. Samples were prepared on TedPella formvar carbon copper 200 mesh grids, drop-cast from toluene.[127]

### 5.2.3 Indium Phosphide – I

Indium phosphide nanocrystals were prepared following Micic et al. with slight variations.[128] Chloroindium oxalate was synthesized by mixing indium chloride with sodium oxalate in acetonitrile in a 1:1 molar ratio. The reaction was heated to 70°C for 15 hours. The resulting suspension was filtered and the solvent removed to yield the chloroindium oxalate complex. Indium phosphide nanocrystals were synthesized by adding the chloroindium oxalate to a solution of trioctylphosphine oxide (TOPO) and trioctylphosphine (TOP) in a 0.1:1 molar ratio. The reaction mixture was degassed under dry nitrogen for two hours at 100°C and then heated to 275°C. Tris(trimethylsilyl)phosphine ($TMS_3P$) was injected into the hot reaction mixture in a 1:1.6 molar ratio to the chloroindium oxalate and the nanocrystals were grown at 270°C for 3 days. The reaction was removed from heat and purified three times by precipitation with methanol and dispersed in toluene.

Chemical etching was attempted with the prepared nanocrystals by the slow addition of a 10% hydrofluoric acid (HF) solution in methanol.[113] The etching was allowed to proceed for 30 minutes before purifying the nanocrystals by precipitation with methanol and dispersed in toluene.

### 5.2.4 Indium Phosphide – II

An additional synthesis for the preparation of indium phosphide was based off Xie, et al. with minor variations.[129] A reaction mixture of 0.4 mmol indium trifluoroacetate, 1.5 mmol myristic acid, and 16 mL 1-octadecene was degassed for two hours under dry nitrogen at 100°C. An injection solution was prepared with 0.2 mmol tris(trimethylsilyl)phosphine, 2.4 mmol octylamine, and 3 mL 1-octadecene. The reaction

mixture was heated to 188°C, precursors were injected, and the nanocrystals were grown at 178°C for up to one hour. UV/Vis spectroscopy was used to monitor the first absorption peak of the growing nanocrystals. At the desired size, the reaction was removed from heat and cooled to 150°C for SILAR shell growth.

SILAR injection solutions were prepared with 0.1 M precursors in 1-octadecene, which were degassed for one hour and left under dry nitrogen. Indium phosphide with shells of zinc sulfide, gallium phosphide (GaP), or gallium sulfide (GaS) were synthesized using zinc stearate, gallium acetylacetonate, trimethylgallium, sulfur, and tris(trimethylsilyl)phosphine. For a typical SILAR reaction, the cation precursor was injected and allowed to react for 15 minutes, followed by the injection of the anion precursor. After 15 minutes, the reaction mixture was heated to 220°C for 30 minutes, followed by additional injections at the elevated temperature. After the desired number of shell layers were grown (typically 2-5 layers), the reaction was removed from heat and diluted with an equal volume of hexanes. The nanocrystals were purified through two methanol extractions, precipitated with acetone, centrifuged, and the pellet was dispersed in toluene.

### 5.2.5 Indium Phosphide – III

This synthesis was performed by Ryan Gresback in the laboratory of Professor Kortshagen. Indium phosphide nanocrystals were synthezied in a plasma reactor using a precursor gas mixture of 15% phosphine ($PH_3$) in hydrogen ($H_2$) and trimethylindium (TMIn, $In(CH_3)_3$) as reported.[102] In a similar process as above, SILAR was used to put a stabilizing ZnS shell on the plasma InP NCs. A known mass of dry InP NCs was

dispersed in a solution of octadecene and myristic acid under nitrogen and heated to 200°C for 30 min under a flow of nitrogen. Each monolayer of ZnS was grown by using preheated and deoxygenated solutions of 0.05 M zinc stearate in ODE and sulfur in ODE. The zinc and sulfur precursors were injected separately at 15-min intervals with stoichiometric ratios (based on a spherical volume thickness calculation) and heated to 220°C. After the desired number of shell layers were grown (typically 2-5 layers), the reaction was removed from heat and diluted with an equal volume of hexanes. The nanocrystals were purified through two methanol extractions, precipitated with acetone, and dispersed in toluene.

### 5.2.6 Cadmium Selenide

Cadmium selenide nanocrystals with an outer shell of zinc sulfide were synthesized using a method modified from Reiss, et al.[108] A mixture of cadmium oxide (CdO, 411 mg), dodecylphosphonic acid (DPA, 1.6 g) and hexadecylamine (18 g) in trioctylphosphine oxide (8.4 g) was heated to 270°C under nitrogen. A solution of trioctylphosphine:selenium (TOP:Se, 4 mL) in TOP (10 mL) was rapidly injected under dry nitrogen and the particles were grown for 15 minutes at 250°C. The reaction was then cooled to 220°C for SILAR injections of 0.1 M zinc stearate and sulfur solutions. Each monolayer was grown for 15 minutes per precursor, for a total of two ZnS monolayers. After complete addition the particles were precipitated and washed with methanol, centrifuged, and dispersed in hexanes.

## 5.3 Results and Discussion

### 5.3.1 Indium Phosphide Hot Injection

Work has focused on the preparation of monodisperse indium phosphide nanocrystals. The reaction reported by Micic et al. was used for the initial synthesis.[128] The reaction was run for 3 days at 300°C with chloroindium oxalate, all of which helped promote the crystallinity and monodispersity of the resulting InP. The X-ray diffraction pattern, shown in Figure 5.3 is consistent with the zinc blende unit cell of InP. The peaks were assigned to diffraction from the <111>, <220>, and <311> planes of crystalline zinc blende InP. The Debye-Scherrer equation was used in conjunction with the full-width at half max of the XRD peaks to calculate the size of the nanocrystals. The diameter of the NCs was calculated to be approximately 2-3 nm, which is in agreement with estimates from TEM images. Looking at the TEM (Figure 5.3b) it appears that the nanocrystals are not monodisperse, as a range of particle sizes are present.

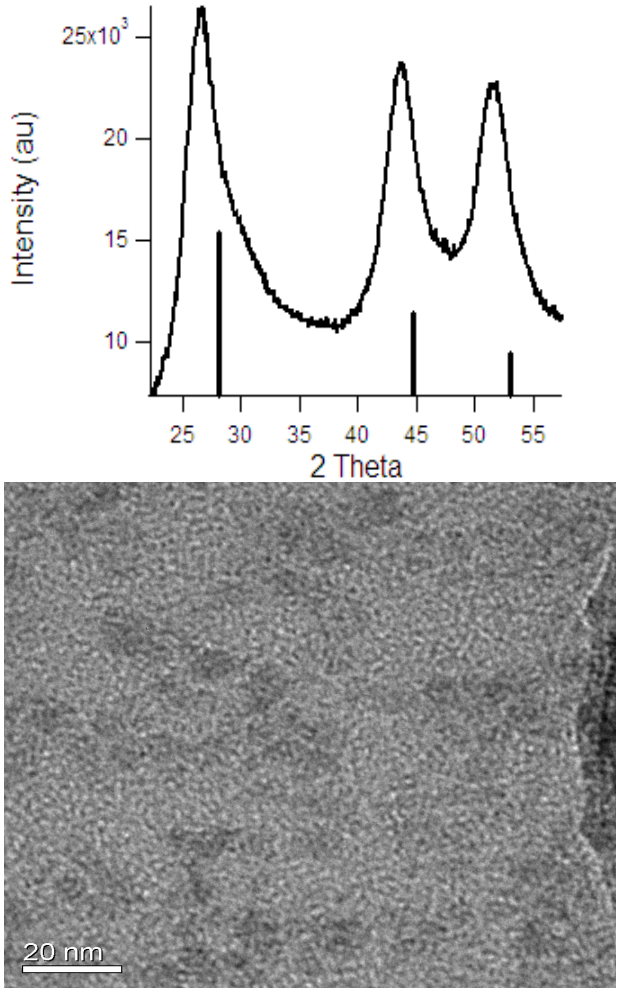


**Figure 5.3: XRD of InP NCs and bulk powder diffraction lines (top-background subtracted) and TEM[127] (bottom) of InP NCs.**

Figure 5.4 shows the UV/VIS absorption spectrum of colloidal InP NCs with a single absorption peak at 590 nm, corresponding to a valence band to conduction band electronic transition. This peak therefore represents the band gap of the InP. Here quantum confinement effects are observed as the band gap of bulk InP shifts from 1.35 eV (918 nm) to around 2 eV (around 600 nm).

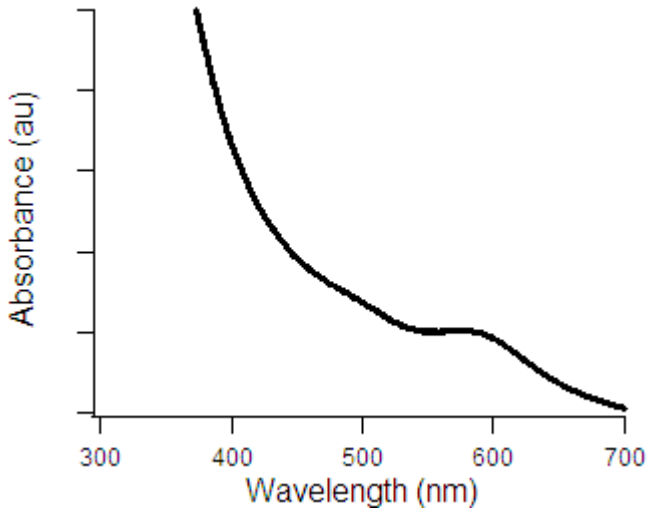


**Figure 5.4. UV/Vis absorption spectrum of InP NC.**

The absorption spectrum can also be used to show the relative size dispersity of the sample. Although you cannot directly calculate a size distribution based on UV/Vis spectroscopy, the absorption peak is a good indication of the size dispersity. The presence of a broad absorption peak indicates that the InP is relatively polydisperse, as a range of nanocrystal sizes absorb a range of wavelengths. This is in agreement with particle sizes visible in the TEM image. In an attempt to decrease the size distribution, size-selective precipitations were performed on polydisperse InP samples through controlled addition of methanol. By adding small amounts of a non-solvent, the largest particles are destabilized and precipitate from solution first, leaving the smaller particles still dispersed. Even after multiple precipitations, monodisperse samples were difficult to produce, yielding absorption spectra with the same absorption properties.

The as-prepared InP nanocrystals exhibit especially poor photoluminescence properties, mostly due to surface trap states. These are passivated by chemically etching the nanocrystals with a hydrofluoric acid solution. The etching serves to fill phosphorus vacancies with fluoride ions. Several different etching conditions; including HF concentration, time etched, temperature and total solution volume, were used to identify the maximum observable PL intensity. It was found that high concentration and increased temperature dissolved the particles making characterization difficult. Figure 5.5 shows the relative increase in intensity of the different conditions compared to the as-prepared InP nanocrystals. Ultimately, the best etching conditions were 10% HF solution in methanol added to the colloidal InP NCs for 30 minutes. This increased the observed PL intensity by over an order of magnitude. However, the HF etching procedure is a sensitive technique. Often the nanocrystals aggregate after purification, making it difficult to disperse them in a solvent and to maintain the previous size distribution.

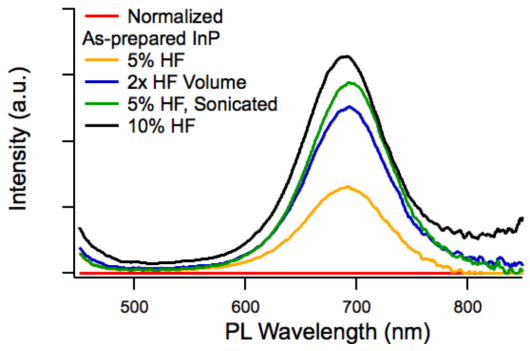


**Figure 5.5. PL spectra of InP with different HF etching conditions normalized to the PL of as prepared un-etched InP NCs.**

This particular synthetic route has several disadvantages. It is first necessary to synthesize the chloroindium oxalate complex, followed by a three day reaction at 300°C.

Therefore, a significant amount of time is involved in each synthesis. Also, the HF etching procedure is inconsistent in increasing the photoluminescence and generating stable nanocrystals. In addition, multiple attempts have been unable to yield a monodisperse sample according to UV/Vis spectroscopy. Therefore, a simpler synthetic route is necessary to produce monodisperse samples that exhibit stabilized photoluminescence.

In order to address these problems, several new synthetic routes were investigated. The Xie, et al. InP synthesis alleviates several of the drawbacks associated with the previous synthesis.[129] The reaction uses standard indium precursors and can be completed in less than one hour. This setup produces monodisperse InP nanocrystals without the need for size-selective precipitations. Also, a one-pot core/shell SILAR reaction can be used to passivate the surface. This reaction was used to study the effects of the number of shell monolayers and shell composition on air-stability and photoluminescence of the InP core.

Unlike the previous route, UV/Vis spectroscopy of particles prepared via the Xie route shows the presence of a strong absorption peak. Figure 5.6 shows the evolution of the first absorption peak over the course of the reaction. A sharp peak appears at 1 minute and is maintained till 20 minutes. After 20 minutes of reaction time, the first absorption peak begins to broaden, indicating a widening of the size distribution. Based on these data, 15 minutes of reaction time appears to be optimal to produce monodisperse InP nanocrystals. The reaction can be rapidly quenched to room temperature using an ice bath to prevent further nanocrystal growth.

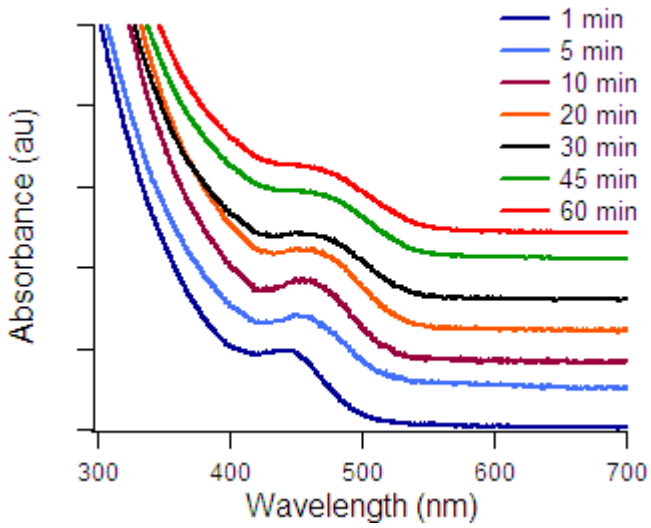


**Figure 5.6. Evolution of InP first absorption peak during growth.**

As the nanocrystals grow over the course of an hour, the first absorption peak is shifted from 450 nm to 480 nm. This 30 nm shift does not represent a large range of particle sizes (less than 0.2 nm); therefore a variable other than reaction time will need to be adjusted to produce larger NCs in future syntheses.

When the desired size of nanocrystals is obtained, a SILAR reaction is used to grow a shell on the InP core. The ZnS shell serves two purposes. It is necessary to protect the InP core against oxidation, in addition to increasing the photoluminescence. When the as-prepared InP nanocrystals in toluene are exposed to air overnight, they oxidize and the first absorption peak almost completely disappears (Figure 5.7- blue trace). However, when the ZnS shell is grown, the InP core is stabilized against oxidation and maintains its original absorption peak (black trace).

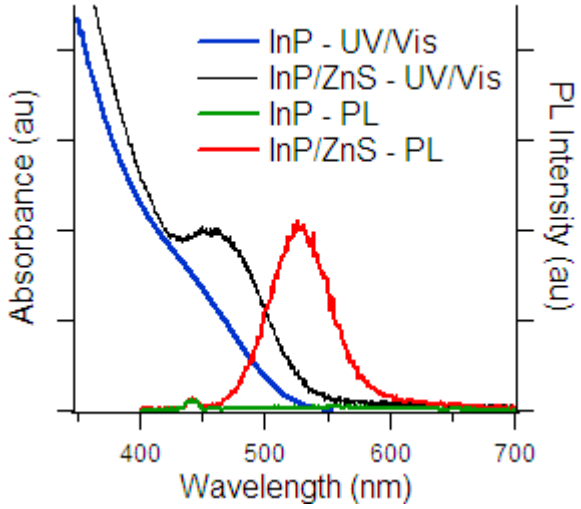


**Figure 5.7. UV/Vis and PL of bare InP and InP/ZnS NCs in toluene exposed to air for 18 hours at room temperature.**

The zinc sulfide shell also serves to passivate any surface trap states, therefore, increasing the photoluminescence. The photoluminescence of the oxidized core is completely quenched (green trace), therefore, by preventing oxidation of the core, PL is stabilized (Figure 5.7- red trace). The photoluminescence also increases as a function of shell thickness. As five ZnS monlayers are added to the core (Figure 5.8), the PL increases with each layer. This increase is due to the complete passivation of surface trap states, in addition to an isolation of the core to prevent oxidation. Although the PL is increasing with each additional layer, the peak appears to be blue-shifting. It is possible that as more ZnS layers are added, they compress the core InP causing a blue-shift in the emission data.

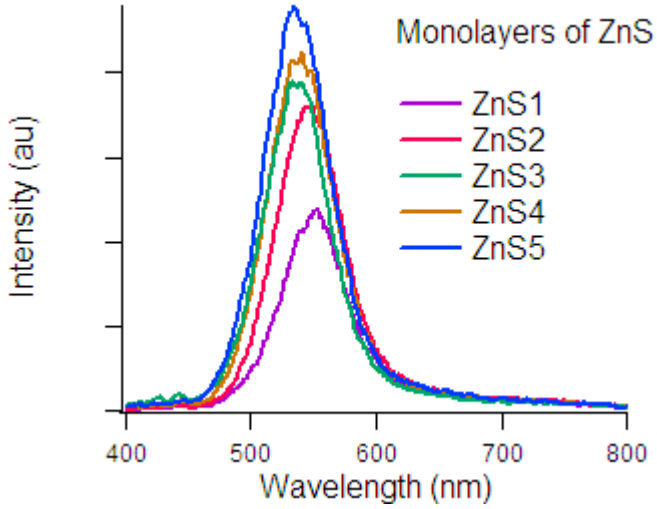


**Figure 5.8. PL spectra of InP/ZnS NCs with varying amounts of ZnS.**

It is important that the addition of the shell does not affect the core, specifically the band gap or the size-distribution. UV/Vis spectroscopy shows that the first absorption peak is maintained after zinc sulfide (ZnS) SILAR injections (Figure 5.9). The absorption peak of the InP core at 460 nm remains constant in shape and energy after three layers of ZnS are grown.

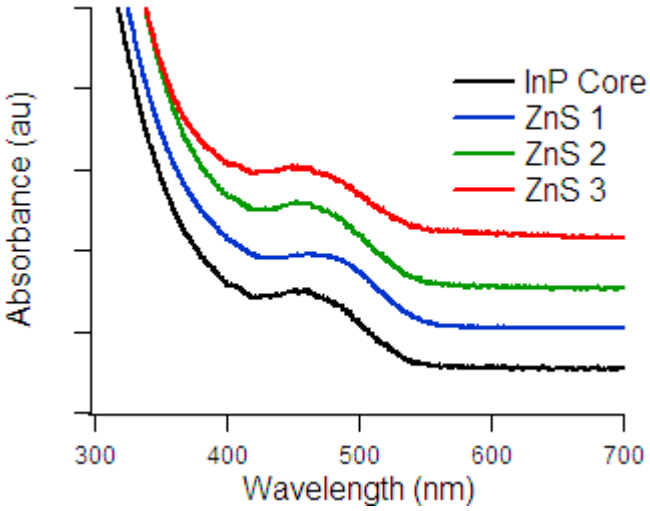


**Figure 5.9. UV/Vis spectra of InP and InP/ZnS NCs with varying amounts of ZnS.**

As in the previous reaction, XRD showed crystalline InP nanocrystals were produced with 3 monolayers of ZnS (Figure 5.10).

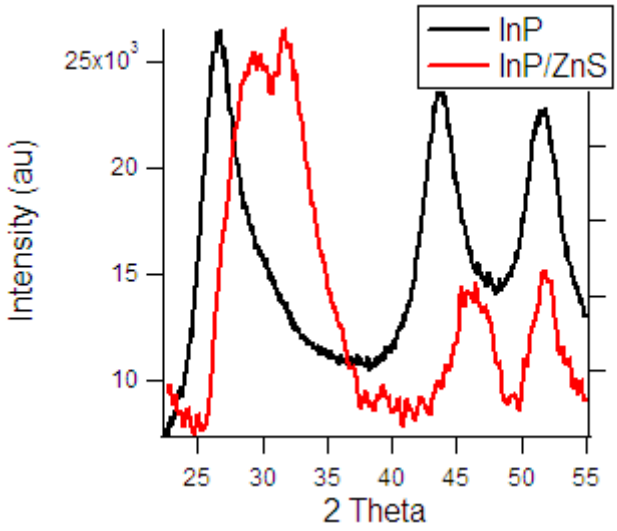


**Figure 5.10. XRD of InP and InP/ZnS NCs showing peak shift upon shell addition. Background has been subtracted.**

These nanocrystals are 3 nm according to XRD. By using XRD, a core/shell structure can be verified by showing the predominant peaks attributed to the core InP NCs. However, these peaks are shifted toward the characteristic ZnS zinc blende peak positions due to the presence of the shell species. When compared to the XRD pattern in Figure 5.3 (2θ values of 28, 44, and 52°), it is obvious that the predominant peaks shifted to 30, 46, and 54°. This shows that ZnS is covering the InP core.

These results show that the InP/ZnS synthesis is reproducible and yields stable nanocrystals. However, other shells have not been reported. Therefore, a similar SILAR procedure was used to grow a gallium phosphide shell on the indium phosphide core. Gallium phosphide was chosen because it is a III-V semiconductor and has a smaller, type I band gap offset than zinc sulfide. The initial hope was that the lower energy band gap would allow a greater number of charge carriers to reach the core, thus producing a more efficient LED. As with the zinc sulfide shell, the growth of gallium phosphide did not affect the position of the InP absorption peaks or the size distribution. In addition, the GaP stabilized the InP core against oxidation when exposed to air. The UV/Vis shows a slight blue shift in the first absorption peak after five days in air; however, this peak remains constant after several weeks (Figure 5.11). This blue-shift could be due to a slight oxidation of the core. Based on the stability of the produced nanocrystals, it appears that a core/shell structure was produced. TEM could be used to see the morphology of the GaP shell produced and give a possible explanation to the slight blue shift in the absorption peak. TEM will show if the resulting nanocrystals are spherical, or if the GaP shell preferentially grew along one crystal face producing a rod-like shape.

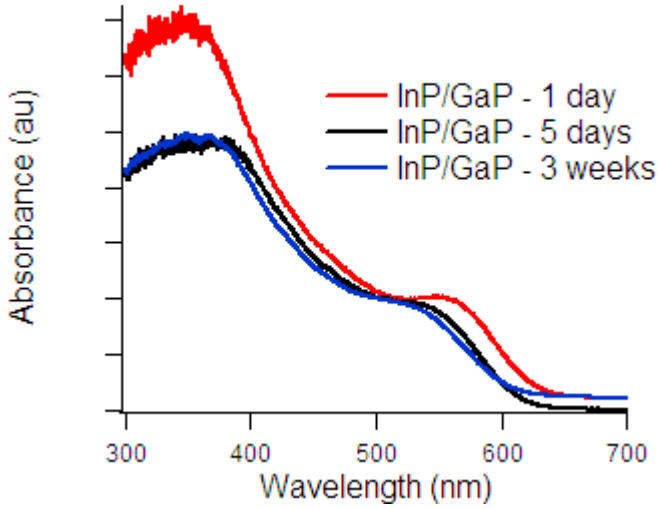


**Figure 5.11. UV/Vis absorption spectra of InP/GaP NCs in toluene over the course of 3 weeks.**

However, photoluminescence spectroscopy of InP/GaP failed to show any observable photoluminescence. It turns out that the smaller band gap of the GaP leads to a higher probability for charge carriers to remain at the surface of the NC. Since the GaP conduction band is lower in energy compared to ZnS, the electrons have sufficient energy to enter the GaP conduction band. Therefore, if the charge carriers remain at the surface of the nanocrystal, they will not recombine radiatively in the InP core.

Finally, a gallium sulfide SILAR reaction was attempted. Multiple attempts using various gallium and sulfur precursors did not produce stable nanocrystal dispersions. The lack of a stable solution made UV/Vis and PL spectroscopy difficult.

In an attempt to understand the previous SILAR reaction, gallium sulfide nanocrystals were synthesized. Reaction conditions similar to the Xie InP synthesis were

used, making use of trimethylgallium and bis(trimethylsilyl)sulfide as precursors. The first absorption peak appeared at 330 nm and remained constant for the initial 45 minutes of reaction (Figure 5.12). The absorption peak at 330 nm shows quantum confined gallium sulfide nanocrystals as the band gap shifted from 3.05 eV in the bulk to 3.75 eV (330 nm) in the nanocrystal. At one hour, the absorption peak began to broaden, indicating an increase in the size distribution. As with the InP/GaS core/shell structure, these nanocrystals were not dispersible in solvent after extraction and precipitation. Several different colloidal stabilizers (including myristic acid, octylamine, TOP and TOPO) and solvents (toluene, chloroform, and hexanes) were used; however, the NCs continued to flocculate from solution. This occurs because the electrostatic repulsive forces provided by the ligands on the GaS nanocrystal are overcome by the strong van der Waals attractive forces of the GaS, causing the NCs to precipitate.

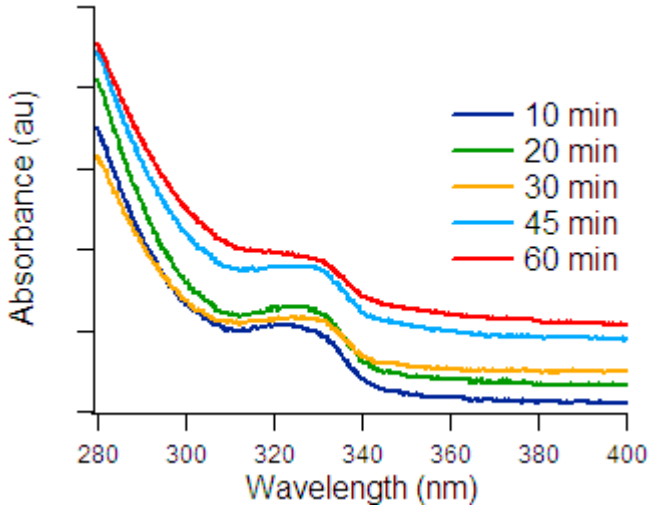


**Figure 5.12. Evolution of GaS first absorption peak during growth.**

### 5.3.2 Indium Phosphide – Plasma Synthesis

Indium phosphide nanocrystals ranging from 2-5 nm were prepared in plasma reactor, resulting in bare InP NCs.[102] Ligand capped and especially as-synthesized plasma InP NCs show little or no PL. If the nanocrystals are allowed to oxidize, quantum yields less than 1% are observed. Therefore, it is necessary to eliminate non-radiative recombination sites on the nanocrystal surface. As discussed above, the two best options are fluoride etches and capping the InP NCs with a wide bandgap semiconductor such as ZnS. Based on the success of the SILAR solution capping, this method was adopted for the plasma-synthesized particles. In this system, a single monolayer of ZnS led to a significant increase in the quantum yield. The addition of more ZnS layers does not further increase the quantum yield of the NCs, likely because all of the non-radiative traps were passivated by the initial monolayer. Overall, photoluminescence quantum yields between 10 – 15 % were observed for the InP/ZnS nanocrystals ranging from 2-5 nm, which is less than half the quantum yield observed in the solution InP NCs (40%).[129] This discrepancy between the plasma and solution InP NCs is most likely due to the poor size distribution of the plasma particles compared to their solution counterparts. However this is still significant improvement and proves to be a viable option to passivate nanocrystals prepared by non-solution techniques.

### 5.3.3 Cadmium Selenide

Cadmium selenide nanocrystals were synthesized with a zinc sulfide shell to study the difference between direct charge injection and Forster energy transfer into nanocrystals in hybrid LEDs.[130] Forster energy transfer involves formation of excitons on organic semiconductors, which can be transferred onto the inorganic nanocrystals, where

they recombine resulting in emission of a photon. In a direct charge injection mechanism, the electrons and holes are directly injected into the NCs where they recombine resulting in a photon. By using various device configurations, we show that both these mechanisms can operate independently to maximize the light emission in LEDs.

The UV/Vis spectrum, in Figure 5.13, shows a first absorption peak at 626 nm, corresponding to 5.6 nm nanocrystals. The second and third absorption peaks of CdSe are also visible at 550 and 510 nm respectively. The PL spectrum shows emission at 640 nm.

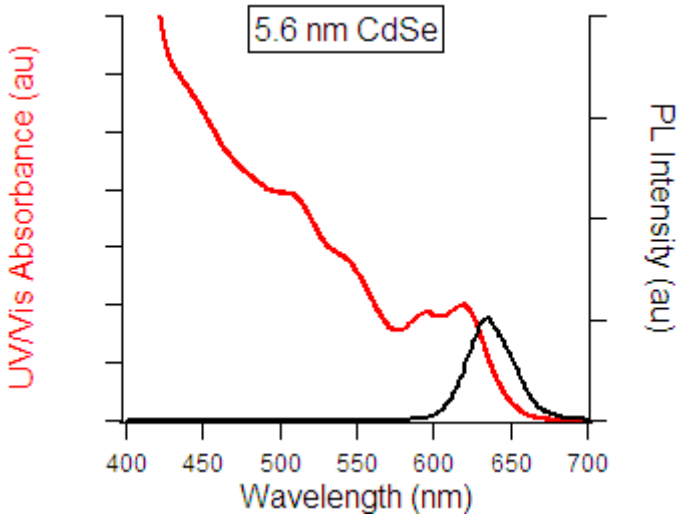


**Figure 5.13. UV/Vis and PL spectra of CdSe/ZnS NCs.**

Using these NCs, three different devices were constructed, one without a hole transport layer, and two with this layer. In the two devices with the added HTL, one had an additional emission layer with the CdSe NCs. The first device was designed to promote Forster energy transfer, the device with two emissive layers and the HTL designed to promote both mechanisms, and the device with just the HTL designed to

promote direct charge injection. By using these different device configurations it was shown that direct charge injection and Forster energy transfer act independently to produce the light from the NCs in an LED depending on device construction. It is also possible to have both direct charge transfer and Forster energy transfer mechanisms play a significant role in the light output.

## 5.4 Conclusion

Semiconductor nanocrystals represent an important emerging field because they show quantum mechanical properties in an easily manipulated real-world package. These unique properties make them lucrative for display applications, including light emitting diodes. To date, several groups have reported the use of CdSe nanocrystals in visible LEDs displaying external efficiencies above 1%. However, there have been far fewer reports on infrared LEDs that can match the efficiencies of the CdSe based systems.

This research seeks to produce efficient IR-LED devices for use in telecommunications. III-V semiconductor nanocrystals were used in preparation of these devices due to their tunable emissions from visible to infrared. Current research has explored the synthesis and characterization of monodisperse, highly photoluminescent indium phosphide nanocrystals, which emit from visible to infrared wavelengths. While several synthetic routes have been explored, the Xie synthesis has produced the best hot-injection results. This method produces a range of particle sizes with narrow size distributions by changing the growth time or concentration of the capping agent. Particles have been produced from 1-4 nm, which display UV/Vis absorption peaks between 340 and 600 nm. However, InP nanocrystals exhibiting emissions in the red and infrared region have not been synthesized to date. In addition, successive ion layer

adsorption and reaction is performed to deposit a shell to stabilize the core. The SILAR method precisely controls the thickness of the shell deposited based on the number of monolayers added and can be done in one pot.

# 6 References


[1] Faraday, M., *Proceedings of the Royal Society* **1856**, *8*, 356.
[2] Ekimov, A. I. and Onushohenko, A., *Pis'ma Zh. Eksp. Teor. Fiz.* **1981**, *34*, 363.
[3] Gratzel, M., *Inorg. Chem.* **2005**, *44*, 6841.
[4] Klimov, V. I., *Semiconductor and Metal Nanocrystals : Synthesis and Electronic and Optical Properties*, Marcel Dekker, New York, **2004**, p.
[5] O'Regan, B. and Gratzel, M., *Nature* **1991**, *353*, 737.
[6] Chen, C.-Y., Wang, M., Li, J.-Y., Pootrakulchote, N., Alibabaei, L., Ngoc-le, C.-h., Decoppet, J.-D., Tsai, J.-H., Gratzel, C., Wu, C.-G., Zakeeruddin, S. M. and Gratzel, M., *ACS Nano* **2009**, *3*, 3103.
[7] Kalyanasundaram, K. and Gratzel, M., *Coord. Chem. Rev.* **1998**, *177*, 347.
[8] Klein, C., Nazeeruddin, M. K., Liska, P., Di Censo, D., Hirata, N., Palomares, E., Durrant, J. R. and Gratzel, M., *Inorg. Chem.* **2004**, *44*, 178.
[9] Kohle, O., Ruile, S. and Gratzel, M., *Inorg. Chem.* **1996**, *35*, 4779.
[10] Nazeeruddin, M. K., Zakeeruddin, S. M., Humphry-Baker, R., Jirousek, M., Liska, P., Vlachopoulos, N., Shklover, V., Fischer, C.-H. and Gratzel, M., *Inorg. Chem.* **1999**, *38*, 6298.
[11] Zakeeruddin, S. M., Nazeeruddin, M. K., Humphry-Baker, R., Gratzel, M. and Shklover, V., *Inorg. Chem.* **1998**, *37*, 5251.
[12] Nazeeruddin, M. K., Kay, A., Rodicio, I., Humphry-Baker, R., Mueller, E., Liska, P., Vlachopoulos, N. and Graetzel, M., *J. Am. Chem. Soc.* **1993**, *115*, 6382.
[13] Nazeeruddin, M. K., Zakeeruddin, S. M., Lagref, J. J., Liska, P., Comte, P., Barolo, C., Viscardi, G., Schenk, K. and Gratzel, M., *Coord. Chem. Rev.* **2004**, *248*, 1317.
[14] Anderson, S., Constable, E. C., Seddon, K. R., Turp, J. E., Baggott, J. E. and Pilling, M. J., *J. Chem. Soc., Dalton Trans.* **1985**, 2247.
[15] Chang, W.-C., Chen, H.-S., Li, T.-Y., Hsu, N.-M., Tingare, Y. S., Li, C.-Y., Liu, Y.-C., Su, C. and Li, W.-R., *Angew. Chem.* **2010**, *122*, 8337.
[16] Chen, C.-Y., Wu, S.-J., Wu, C.-G., Chen, J.-G. and Ho, K.-C., *Angew. Chem. Int. Ed.* **2006**, *45*, 5822.
[17] Hodson, E. and Simpson, S. J., *Polyhedron* **2004**, *23*, 2695.
[18] Jose, D. A., Kar, P., Koley, D., Ganguly, B., Thiel, W., Ghosh, H. N. and Das, A., *Inorg. Chem.* **2007**, *46*, 5576.
[19] Kar, P., Verma, S., Das, A. and Ghosh, H. N., *J. Phys. Chem. C* **2009**, *113*, 7970.
[20] Kar, P., Verma, S., Sen, A., Das, A., Ganguly, B. and Ghosh, H. N., *Inorg. Chem.* **2010**, *49*, 4167.
[21] Martineau, D., Beley, M., Gros, P. C., Cazzanti, S., Caramori, S. and Bignozzi, C. A., *Inorg. Chem.* **2007**, *46*, 2272.
[22] Ramakrishna, G., Jose, D. A., Kumar, D. K., Das, A., Palit, D. K. and Ghosh, H. N., *J. Phys. Chem. B* **2005**, *109*, 15445.

[23] Rau, S., Buttner, T., Temme, C., Ruben, M., Gorls, H., Walther, D., Duati, M., Fanni, S. and Vos, J. G., *Inorg. Chem.* **2000**, *39*, 1621.
[24] Sullivan, B. P., Baumann, J. A., Meyer, T. J., Salmon, D. J., Lehmann, H. and Ludi, A., *J. Am. Chem. Soc.* **1977**, *99*, 7368.
[25] Tabatabaeian, K., Downing, P., Adams, H., Mann, B. E. and White, C., *J. Organomet. Chem.* **2003**, *688*, 75.
[26] Wei, Q. and Galoppini, E., *Tetrahedron* **2004**, *60*, 8497.
[27] Ardo, S. and Meyer, G. J., *Chem. Soc. Rev.* **2009**, *38*, 115.
[28] Ekimov, A. I., Efros, A. L. and Onushohenko, A., *Solid State Commun.* **1985**, *56*, 921.
[29] Buffat, P. and Borel, J. P., *Phys. Rev. A* **1976**, *13*, 2287.
[30] Steckel, J. S., Coe-Sullivan, S., Bulovic, V. and Bawendi, M. G., *Adv. Mater. (Weinheim, Ger.)* **2003**, *15*, 1862.
[31] Campbell, S. A., Gladfelter, W., Holmes, R. and Kortshagen, U. in *Multi Spectral Nanoparticle Based Light Emitting Devices*, *Vol.* The Center for Nanostructured Applications, University of Minnesota, **2006**.
[32] Adams, D. M., Brus, L., Chidsey, C. E. D., Creager, S., Creutz, C., Kagan, C. R., Kamat, P. V., Lieberman, M., Lindsay, S., Marcus, R. A., Metzger, R. M., Michel-Beyerle, M. E., Miller, J. R., Newton, M. D., Rolison, D. R., Sankey, O., Schanze, K. S., Yardley, J. and Zhu, X. Y., *J. Phys. Chem. B* **2003**, *107*, 6668.
[33] Wolfbauer, G., Bond, A. M., Deacon, G. B., MacFarlane, D. R. and Spiccia, L., *J. Am. Chem. Soc.* **1999**, *122*, 130.
[34] Nazeeruddin, M. K., De Angelis, F., Fantacci, S., Selloni, A., Viscardi, G., Liska, P., Ito, S., Takeru, B. and Gratzel, M., *J. Am. Chem. Soc.* **2005**, *127*, 16835.
[35] Tuikka, M., Hirva, P., Rissanen, K., Korppi-Tommola, J. and Haukka, M., *Chem. Commun. (Cambridge, U. K.)* **2011**, *47*, 4499.
[36] Burmeister, J. L., *Coord. Chem. Rev.* **1968**, *3*, 225.
[37] Burmeister, J., *Coord. Chem. Rev.* **1990**, *105*, 77.
[38] Basolo, F., Burmeister, J. L. and Poe, A. J., *J. Am. Chem. Soc.* **1963**, *85*, 1700.
[39] Burmeister, J. L. and Basolo, F., *Inorg. Chem.* **1964**, *3*, 1587.
[40] MacDougall, J. J., Nelson, J. H., Fultz, W. C., Burmeister, J. L., Holt, E. M. and Alcock, N. W., *Inorg. Chim. Acta* **1982**, *63*, 75.
[41] Paviglianiti, A. J., Minn, D. J., Fultz, W. C. and Burmeister, J. L., *Inorg. Chim. Acta* **1989**, *159*, 65.
[42] Burmeister, J. L., Hassel, R. L. and Phelan, R. J., *Inorg. Chem.* **1971**, *10*, 2032.
[43] Hassel, R. L. and Burmeister, J. L., *J. Chem. Soc. D: Chem. Commun.* **1971**, *0*, 568.
[44] Fultz, W. C. and Burmeister, J. L., *Inorg. Chim. Acta* **1980**, *45*, L271.
[45] Hassel, R. L. and Burmeister, J. L., *Inorg. Chim. Acta* **1974**, *8*, 155.
[46] Nicpon, P. and Meek, D. W., *Inorg. Chem.* **1967**, *6*, 145.
[47] Bertini, I. and Sabatini, A., *Inorg. Chem.* **1966**, *5*, 1025.
[48] Vandenburgh, L., Buck, M. R. and Freedman, D. A., *Inorg. Chem.* **2008**, *47*, 9134.
[49] Brewster, T. P., Ding, W., Schley, N. D., Hazari, N., Batista, V. S. and Crabtree, R. H., *Inorg. Chem.* **2011**, *50*, 11938.
[50] Rawling, T., Buchholz, F. and McDonagh, A. M., *Aust. J. Chem.* **2008**, *61*, 405.

[51] Maerker, G. and Case, F. H., *J. Am. Chem. Soc.* **1958**, *80*, 2745.
[52] Freedman, D. A., Gill, T. P., Blough, A. M., Koefod, R. S. and Mann, K. R., *Inorg. Chem.* **1997**, *36*, 95.
[53] Viala, C. and Coudret, C., *Inorg. Chim. Acta* **2006**, *359*, 984.
[54] Sullivan, B. P., Salmon, D. J. and Meyer, T. J., *Inorg. Chem.* **1978**, *17*, 3334.
[55] Lay, P. A., Sargeson, A. M., Taube, H., Chou, M. H. and Creutz, C., *Inorg. Synth.* **1986**, 291.
[56] Hasan, K. and Zysman-Colman, E., *Inorg. Chem.* **2012**, *51*, 12560.
[57] Homanen, P., Haukka, M., Pakkanen, T. A., Pursiainen, J. and Laitinen, R. H., *Organometallics* **1996**, *15*, 4081.
[58] Maroney, M. J., Fey, E. O., Baldwin, D. A., Stenkamp, R. E., Jensen, L. H. and Rose, N. J., *Inorg. Chem.* **1986**, *25*, 1409.
[59] Lin, S. W. and Schreiner, A. F., *Inorg. Chim. Acta* **1971**, *5*, 290.
[60] Anderson, N. A. and Lian, T., *Annu. Rev. Phys. Chem.* **2005**, *56*, 491.
[61] Asbury, J. B., Ellingson, R. J., Ghosh, H. N., Ferrere, S., Nozik, A. J. and Lian, T. Q., *J. Phys. Chem. B* **1999**, *103*, 3110.
[62] Stockwell, D., Yang, Y., Huang, J., Anfuso, C., Huang, Z. and Lian, T., *J. Phys. Chem. C* **2010**, *114*, 6560.
[63] Anderson, N. A., Ai, X. and Lian, T., *J. Phys. Chem. B* **2003**, *107*, 14414.
[64] Bauer, C., Boschloo, G., Mukhtar, E. and Hagfeldt, A., *J. Phys. Chem. B* **2001**, *105*, 5585.
[65] Fessenden, R. W. and Kamat, P. V., *J. Phys. Chem.* **1995**, *99*, 12902.
[66] Katoh, R., Furube, A., Hara, K., Murata, S., Sugihara, H., Arakawa, H. and Tachiya, M., *J. Phys. Chem. B* **2002**, *106*, 12957.
[67] Katoh, R., Furube, A., Barzykin, A. V., Arakawa, H. and Tachiya, M., *Coord. Chem. Rev.* **2004**, *248*, 1195.
[68] Benko, G., Kallioinen, J., Korppi-Tommola, J. E. I., Yartsev, A. P. and Sundstrom, V., *J. Am. Chem. Soc.* **2001**, *124*, 489.
[69] Kallioinen, J., Benko, G., Myllyperkio, P., Khriachtchev, L., Skarman, B., Wallenberg, R., Tuomikoski, M., Korppi-Tommola, J., Sundstrom, V. and Yartsev, A. P., *J. Phys. Chem. B* **2004**, *108*, 6365.
[70] Rossini, J. E., Huss, A. S., Bohnsack, J. N., Blank, D. A., Mann, K. R. and Gladfelter, W. L., *J. Phys. Chem. C* **2010**, *115*, 11.
[71] Huss, A. S., Rossini, J. E., Ceckanowicz, D. J., Bohnsack, J. N., Mann, K. R., Gladfelter, W. L. and Blank, D. A., *J. Phys. Chem. C* **2010**, *115*, 2.
[72] Gerd-Jan ten Brink, Isabel W. C. E. Arends, Marcel Hoogenraad, Göran Verspui and Roger A. Sheldon, *Adv. Synth. Catal.* **2003**, *345*, 497.
[73] Zhang, D., Telo, J. P., Liao, C., Hightower, S. E. and Clennan, E. L., *J. Phys. Chem. A* **2007**, *111*, 13567.
[74] Schwartz, D. A., Norberg, N. S., Nguyen, Q. P., Parker, J. M. and Gamelin, D. R., *J. Am. Chem. Soc.* **2003**, *125*, 13205.
[75] Viswanatha, R., Sapra, S., Satpati, B., Satyam, P. V., Dev, B. N. and Sarma, D. D., *J. Mater. Chem.* **2004**, *14*, 661.
[76] Kay, A. and Gratzel, M., *Sol. Energy Mater. Sol. Cells* **1996**, *44*, 99.

[77] Leschkies, K. S., Divakar, R., Basu, J., Enache-Pommer, E., Boercker, J. E., Carter, C. B., Kortshagen, U. R., Norris, D. J. and Aydil, E. S., *Nano Lett.* **2007**, *7*, 1793.
[78] Slattery, S. J., Gokaldas, N., Mick, T. and Goldsby, K. A., *Inorg. Chem.* **1994**, *33*, 3621.
[79] Martineau, D., Beley, M. and Gros, P. C., *J. Org. Chem.* **2005**, *71*, 566.
[80] Cook, M. J., Lewis, A. P., Mcauliffe, G. S. G., Skarda, V., Thomson, A. J., Glasper, J. L. and Robbins, D. J., *J. Chem. Soc.,Perkin Trans. 2* **1984**, 1293.
[81] Giordano, P. J., Bock, C. R., Wrighton, M. S., Interrante, L. V. and Williams, R. F. X., *J. Am. Chem. Soc.* **1977**, *99*, 3187.
[82] Skarda, V., Cook, M. J., Lewis, A. P., Mcauliffe, G. S. G., Thomson, A. J. and Robbins, D. J., *J. Chem. Soc., Perkin Trans. 2* **1984**, 1309.
[83] Ohsawa, Y., DeArmond, M. K., Hanck, K. W., Morris, D. E., Whitten, D. G. and Neveux, P. E., *J. Am. Chem. Soc.* **1983**, *105*, 6522.
[84] Hore, P. J., *Nuclear Mag. Res.*, Oxford University Press, **1995**, p.
[85] Zelakiewicz, B. S., de Dios, A. C. and Tong, *J. Am. Chem. Soc.* **2002**, *125*, 18.
[86] Badia, A., Gao, W., Singh, S., Demers, L., Cuccia, L. and Reven, L., *Langmuir* **1996**, *12*, 1262.
[87] Kohlmann, O., Steinmetz, W. E., Mao, X.-A., Wuelfing, W. P., Templeton, A. C., Murray, R. W. and Johnson, C. S., *J. Phys. Chem. B* **2001**, *105*, 8801.
[88] Furube, A., Katoh, R., Hara, K., Murata, S., Arakawa, H. and Tachiya, M., *J. Phys. Chem. B* **2003**, *107*, 4162.
[89] Furube, A., Katoh, R., Yoshihara, T., Hara, K., Murata, S., Arakawa, H. and Tachiya, M., *J. Phys. Chem. B* **2004**, *108*, 12583.
[90] Katoh, R., Furube, A., Fuke, N., Fukui, A. and Koide, N., *J. Phys. Chem. C* **2012**, *116*, 22301.
[91] Henry, W., Coates, C. G., Brady, C., Ronayne, K. L., Matousek, P., Towrie, M., Botchway, S. W., Parker, A. W., Vos, J. G., Browne, W. R. and McGarvey, J. J., *J. Phys. Chem. A* **2008**, *112*, 4537.
[92] Bhasikuttan, A. C., Suzuki, M., Nakashima, S. and Okada, T., *J. Am. Chem. Soc.* **2002**, *124*, 8398.
[93] Vlcek, A., *Coord. Chem. Rev.* **2000**, *200-202*, 933.
[94] Alivisatos, A. P., *Science* **1996**, *271*, 933.
[95] Liu, W., Howarth, M., Greytak, A. B., Zheng, Y., Nocera, D. G., Ting, A. Y. and Bawendi, M. G., *J. Am. Chem. Soc.* **2008**, *130*, 1274.
[96] Rogach, A. L., Gaponik, N., Lupton, J. M., Bertoni, C., Gallardo, D. E., Dunn, S., Pira, N. L., Paderi, M., Repetto, P., Romanov, S. G., O'Dwyer, C., Torres, C. M. S. and Eychmuller, A., *Angew. Chem. Int. Ed.* **2008**, *47*, 6538.
[97] Koleilat, G. I., Levina, L., Shukla, H., Myrskog, S. H., Hinds, S., Pattantyus-Abraham, A. G. and Sargent, E. H., *ACS Nano* **2008**, *2*, 833.
[98] Holmes, R. J., D'Andrade, B. W., Forrest, S. R., Ren, X., Li, J. and Thompson, M. E., *Appl. Phys. Lett.* **2003**, *83*, 3818.
[99] Baldo, M. A., Adachi, C. and Forrest, S. R., *Phys. Rev. B* **2000**, *62*, 10967.
[100] Coe, S., Woo, W. K., Bawendi, M. and Bulovic, V., *Nature* **2002**, *420*, 800.
[101] Gresback, R., Holman, Z. and Kortshagen, U., *Appl. Phys. Lett.* **2007**, *91*, 093119.

[102] Gresback, R., Hue, R., Gladfelter, W. L. and Kortshagen, U., *Nanoscale Research Letters* **2011**, *6:68*.
[103] Murray, C. B., Norris, D. J. and Bawendi, M. G., *J. Am. Chem. Soc.* **1993**, *115*, 8706.
[104] LaMer, V. K. and Dinegar, R. H., *J. Am. Chem. Soc.* **1950**, *72*, 4847.
[105] Yu, P. Y. C., M, *Fundamentals of Semiconductors*, Springer-Verlag, Berlin, **2001**, p.
[106] Huang, X., Lindgren, E. and Chelikowsky, J. R., *Phys. Rev. B* **2005**, *71*.
[107] Narayanaswamy, A., Feiner, L. F. and van der Zaag, P. J., *J. Phys. Chem. C* **2008**, *112*, 6775.
[108] Reiss, P., Bleuse, J. and Pron, A., *Nano Lett.* **2002**, *2*, 781.
[109] Li, J. J., Wang, Y. A., Guo, W. Z., Keay, J. C., Mishima, T. D., Johnson, M. B. and Peng, X. G., *J. Am. Chem. Soc.* **2003**, *125*, 12567.
[110] Li, L. and Reiss, P., *J. Am. Chem. Soc.* **2008**, *130*, 11588.
[111] Guzelian, A. A., Katari, J. E. B., Kadavanich, A. V., Banin, U., Hamad, K., Juban, E., Alivisatos, A. P., Wolters, R. H., Arnold, C. C. and Heath, J. R., *J. Phys. Chem.* **1996**, *100*, 7212.
[112] Kim, S. H., Wolters, R. H. and Heath, J. R., *J. Chem. Phys.* **1996**, *105*, 7957.
[113] Micic, O. I., Sprague, J., Lu, Z. H. and Nozik, A. J., *Appl. Phys. Lett.* **1996**, *68*, 3150.
[114] Colvin, V. L., Schlamp, M. C. and Alivisatos, A. P., *Nature* **1994**, *370*, 354.
[115] Dabbousi, B. O., Bawendi, M. G., Onitsuka, O. and Rubner, M. F., *Appl. Phys. Lett.* **1995**, *66*, 1316.
[116] Schlamp, M. C., Peng, X. G. and Alivisatos, A. P., *J. Appl. Phys.* **1997**, *82*, 5837.
[117] Mattoussi, H., Radzilowski, L. H., Dabbousi, B. O., Thomas, E. L., Bawendi, M. G. and Rubner, M. F., *J. Appl. Phys.* **1998**, *83*, 7965.
[118] Coe-Sullivan, S., Woo, W. K., Steckel, J. S., Bawendi, M. and Bulovic, V., *Organic Electronics* **2003**, *4*, 123.
[119] Efros, A. L., *Nat. Mater.* **2008**, *7*, 612.
[120] Nirmal, M., Dabbousi, B. O., Bawendi, M. G., Macklin, J. J., Trautman, J. K., Harris, T. D. and Brus, L. E., *Nature* **1996**, *383*, 802.
[121] Dekel, E., Gershoni, D., Ehrenfreund, E., Spektor, D., Garcia, J. M. and Petroff, P. M., *Phys. Rev. Lett.* **1998**, *80*, 4991.
[122] Mahler, B., Spinicelli, P., Buil, S., Quelin, X., Hermier, J. P. and Dubertret, B., *Nat. Mater.* **2008**, *7*, 659.
[123] Chen, Y., Vela, J., Htoon, H., Casson, J. L., Werder, D. J., Bussian, D. A., Klimov, V. I. and Hollingsworth, J. A., *J. Am. Chem. Soc.* **2008**, *130*, 5026.
[124] Gao, M. Y., Richter, B., Kirstein, S. and Mohwald, H., *J. Phys. Chem. B* **1998**, *102*, 4096.
[125] Hirose, Y., Kahn, A., Aristov, V. and Soukiassian, P., *Appl. Phys. Lett.* **1996**, *68*, 217.
[126] Hirose, Y., Kahn, A., Aristov, V., Soukiassian, P., Bulovic, V. and Forrest, S. R., *Phys. Rev. B* **1996**, *54*, 13748.
[127] Gresback, R.

[128] Micic, O. I., Sprague, J. R., Curtis, C. J., Jones, K. M., Machol, J. L., Nozik, A. J., Giessen, H., Fluegel, B., Mohs, G. and Peyghambarian, N., *J. Phys. Chem.* **1995**, *99*, 7754.
[129] Xie, R., Battaglia, D. and Peng, X., *J. Am. Chem. Soc.* **2007**, *129*, 15432.
[130] Kumar, B., Hue, R., Gladfelter, W. L. and Campbell, S. A., *J. Appl. Phys.* **2012**, *112*, 034501.